CHUNGSZENTRUM JÜLICH GmbH

KFA

Institut für Festkörperforschung

Fluid membranes – Theory of vesicle conformations

Udo Seifert

Berichte des Forschungszentrums Jülich ; 2997
ISSN 0944-2952
Institut für Festkörperforschung Jül-2997

Zu beziehen durch: Forschungszentrum Jülich GmbH · Zentralbibliothek
D-52425 Jülich · Bundesrepublik Deutschland
Telefon: 02461/61-6102 · Telefax: 02461/61-6103 · Telex: 833556-70 kfa d

Fluid membranes – Theory of vesicle conformations

Udo Seifert

Habilitation theses Ludwig-Maximilians-Universität München
submitted October 1994.

Contents

List of recurrent symbols

Symbol	Meaning	defined in Eq.
A	area of the vesicle	2.49
ΔA	area difference between the two monolayers	2.46
ΔA_0	optimal area difference between the two monolayers	2.47
b	friction coefficient for monolayer slipping	7.29
c_0	reduced spontaneous curvature	2.56
C_0	spontaneous curvature	2.54
C_{ij}	elements of the correlation matrix	4.24
d	distance between bilayer mid-plane and monolayer neutral surface	after Eq.2.19
$d_i^{(1,2,3)}$	linear term in an expansion of the geometrical quantities	4.7-4.9
$D_{ij}^{1,2,3}$	matrix elements of the second variation of the geometrical quantities	4.7-4.9
$\mathbf{E}$	energy matrix	2.29
E_0	energy of a bending mode	2.14
E_0^a	energy of a bending mode of a bound bilayer	6.4
f	energy density of a bilayer membrane	2.23
f_0	energy density of a membrane in the classical model	2.10
$f_1^{\pm}$	elastic energy density of the monolayers	2.19
F	energy of a bilayer membrane	2.28
F_0	energy of a membrane in the classical model	2.13
F_0^a	energy of a bound bilayer in harmonic approximation	6.4
g_i	linear term in an expansion of the bending energy	4.6
G	dimensionless bending energy	2.51
G_{ij}	matrix of the second variation of the bending energy	4.6
H	mean curvature	2.1
k^m	elastic compression modulus of the monolayer	2.19
K	Gaussian curvature	2.2
$\mathbf{K}$	external force acting on the liquid	7.1
l_0	distance from the wall for which the adhesion potential is minimal	6.21
m	reduced total mean curvature	2.56
m_0	reduced optimal area difference	2.56
M	total mean curvature	2.45
$\mathbf{n}$	normal vector	2.6
N	total number of modes	4.5

$N^{\pm}$	number of lipid molecules in the two layers	2.40
P	Lagrange multiplier for volume	2.57
Q	Lagrange multiplier for mean curvature	2.57
R_g	gas constant	2.37
R_0	equivalent sphere radius	2.49
R_1^*	inverse contact curvature	6.10
S_{ij}	elements of the stability matrix	4.19
$u_{l,m}$	expansion coefficients of fluctuating quasispherical shape	4.38
v	reduced volume	2.67
$\mathbf{v}$	velocity field of the surrounding liquid	7.1
V^0	value of the adhesion potential in its minimum	6.21
V_f^0	value of the adhesion potential for which a free vesicle becomes deformed	6.22
V_u^0	value of the adhesion potential for which thermally activated unbinding sets in	6.26
w	scaled contact potential for adhesion	6.11
W	(i) energy of a vesicle in the area-difference elasticity model	2.50
	(ii) contact potential for adhesion (in Chapter 6)	6.9
W_a	value of contact potential at adhesion transition	6.12
α	material parameter of the area-difference elasticity	2.52
γ_0	damping rate of a bending mode in the classical model	7.25
γ_0^a	damping rate of a bending mode of a bound membrane	7.44
$\gamma_{1,2}$	damping rates of coupled bilayer modes	7.35
Γ^a	kinetic coefficient of a bound membrane	7.42
Γ_0	kinetic coefficient in the classical model	7.23
Δ	dimensionless excess area	4.37
κ	bilayer bending rigidity	2.10
$\tilde{\kappa}$	renormalized bilayer bending rigidity	2.30
κ^m	bending rigidity of a monolayer	2.34
κ_G	Gaussian bending rigidity of the bilayer	2.10
$\xi, \xi_\Sigma, \xi_\kappa$	crossover length-scales for a bound bilayer	6.5 and 6.6
ρ	reduced density difference	2.24
$\bar{\rho}$	reduced average density deviation	2.25
$\rho^{\pm}$	reduced density difference deviations	2.22
$\bar{\sigma}$	dimensionless effective tension	4.59
Σ	Lagrange multiplier for area	2.57
τ	ratio between reduced temperature and excess area	4.45
ϕ_0	equilibrium number density of lipids in the monolayer	2.19
$\phi^{\pm}$	number densities of lipids in the monolayer	2.19
$\phi^{\pm}_{\|proj}$	number densities of lipids in the monolayer projected onto bilayer midplane	2.19
Φ	variational free energy functional	2.57
Ω	curvature of adhesion potential	6.2

Chapter 1

Introduction

1.1 Vesicles

Membranes as studied in this treatise consist of a bilayer of lipid molecules that are composed of a hydrophilic head and two hydrophobic hydrocarbon chains. When introduced into an aqueous environment, these amphiphilic molecules aggregate spontaneously into two monomolecular layers held together by weak non-covalent forces due to the hydrophobic effect. These membranes form large encapsulating "bags" called *vesicles* because open sheet-like conformations would involve a large energy along the hydrophobic edges. Even though the membrane is only a few nanometers thick, the size of these vesicles can reach macroscopic dimensions of up to 100 micrometers. Video microscopy reveals both an extreme softness of the membrane since thermally excited shape fluctuations are strong enough to become visible and an amazing variety of different shapes, among which shape transformations can be induced by changing parameters like the temperature or osmotic conditions.[1]

Interest in these systems arises from at least three perspectives[2], emphasizing (i) the unique material properties of a fluid membrane resulting from its molecular architecture (the *physical chemistry* aspect), (ii) the enormous variety of conformations exhibited by membranes considered as two-dimensional surfaces (the *statistical physics* point of view), and (iii) the ubiquitousness of membranes in *biological* systems. Before we return to these aspects later in this introduction, a few examples will serve to introduce the physical object of this study.

The most prominent example of a shape transformation is the budding transition shown in Fig. 1.1, where the shape change of an initially spherical vesicle is recorded with video

[1] Experiments on vesicle shapes and their transformations are reviewed in (Wortis *et al.*, 1993).

[2] Reviews and surveys on the physics of membranes include (Meunier *et al.*, 1987; Nelson *et al.*, 1989; Sackmann, 1990; Lipowsky, 1991; Lipowsky *et al.*, 1991; Bloom *et al.*, 1991; Beysens *et al.*, 1991; Gompper & Schick, 1994; Lipowsky & Sackmann, 1994)

microscopy. As the temperature increases, the sphere becomes a prolate ellipsoid. While this transformation may seem inevitable given that the thermal expansion of the area is much larger than that of the enclosed volume, the surprise is the occurrence of a pear shape with broken up/down symmetry as the temperature is increased further. Experimentally, it is still somewhat controversial whether the pears with the wide neck are equilibrium states or kinetic transients. As will be seen, these alternatives depend on subtle material properties of the bilayer. At even higher temperature, the neck closes, resulting in two spherical compartments that are sitting on top of each other but still connected by a narrow constriction. In all but the first and last shape, the video exhibits pronounced fluctuations which the still pictures, of course, cannot convey.

The budding transition does not necessarily happen; sometimes the reflection symmetry is restored upon further heating, as shown in the reentrant sequence displayed in Fig. 1.2. Alternatively, the spherical shape can become oblate after a temperature increase. This shape then develops into a discocyte with subsequent transformation into a stomatocyte as shown in Fig. 1.3. This sequence is particularly interesting since the discocytes look very much like the rest shape of red blood cells. Indeed, the quest for understanding the biconcave shape of the red blood cell motivated much of the earlier work on vesicles.

A significant shape change such as budding illustrates that fluidity is an important material property of this system. These shape transformations would hardly be possible if the membrane resisted shear. Still, the bilayer structure is quite robust; neither mesoscopic pores or holes are formed, nor does the topology of the vesicle change since the buds are usually not fissioned from the mother vesicles.

Even though the topology remains the same on the timescale of minutes to hours on which these shape changes are recorded, vesicles of non-spherical topology do exist.[3] Some of the experimentally observed shapes are shown in Fig. 1.4 for genus 1 (one hole), in Fig. 1.5 for genus 2 (two holes), and in Fig. 1.6 for higher genus, respectively. Characteristic for the latter shape are strong fluctuations of the position of the necks.

For a theoretical description on mesoscopic length-scales much larger than the bilayer thickness, membranes can be considered as two-dimensional surfaces embedded in three dimensional space. Their conformations, however, are fundamentally distinct from interfaces since they are not determined by a surface tension but rather by bending elasticity as introduced independently more than twenty years ago by Canham, Helfrich and Evans[4]. This

[3]Experimental records of vesicle shapes of non-spherical topology are given in (Mutz & Bensimon, 1991; Fourcade *et al.*, 1992; Michalet *et al.*, 1994; Michalet, 1994). The theoretical work will be referenced in the main part.

[4](Canham, 1970; Helfrich, 1973; Evans, 1974)

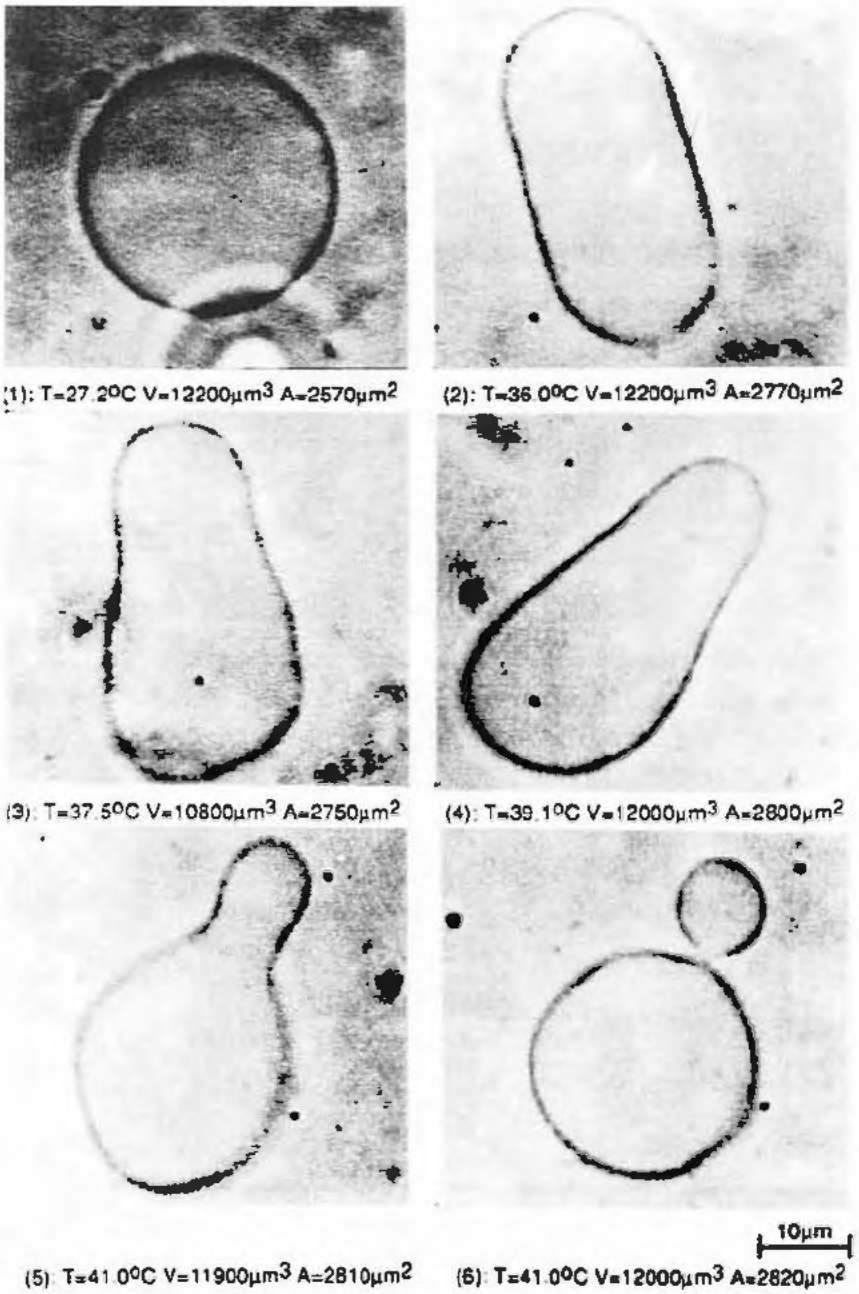

Figure 1.1: Budding transition. The temperature increases from 27.2°C, 36.0°C, 37.5°C, 39.1°C, 41.0°C to 41.0 ° from left to right and top to bottom. (Käs & Sackmann, 1991).

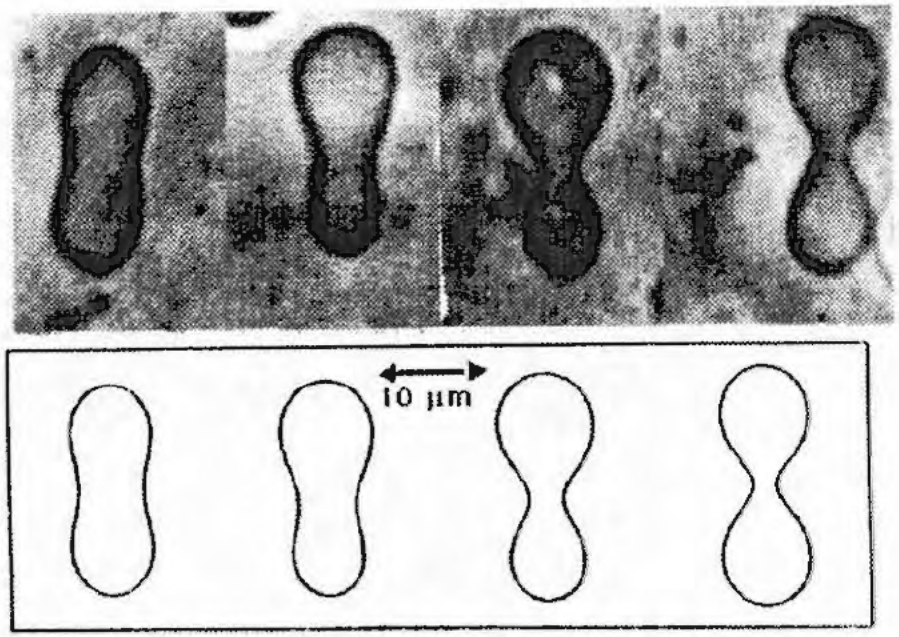

Figure 1.2: Reentrant transition. The temperature increases from 20.7°C, 32.6°C, 40.0°C, to 44.3 ° from left to right. The theoretical curves have been obtained within the BC model as discussed in Sect. 3.7.3. (Berndl *et al.*, 1990).

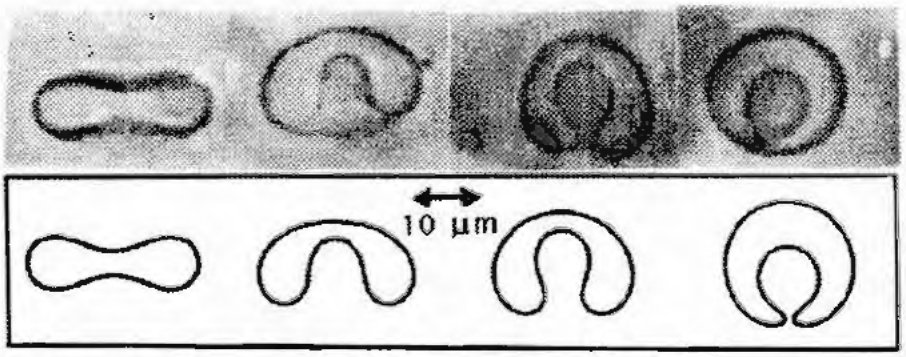

Figure 1.3: Dicocyte/stomatocyte transition. The temperature increases from 43.8°C, 43.9°C, 44.0°C, to 44.1°C from left to right. The theoretical curves show the contour of corresponding stationary shapes (Berndl *et al.*, 1990).

fundamental difference is the reason for the great variety of non-spherical shapes of vesicles, in contrast to the characteristic spherical equilibrium shapes of simple liquids which are governed by isotropic surface tension.

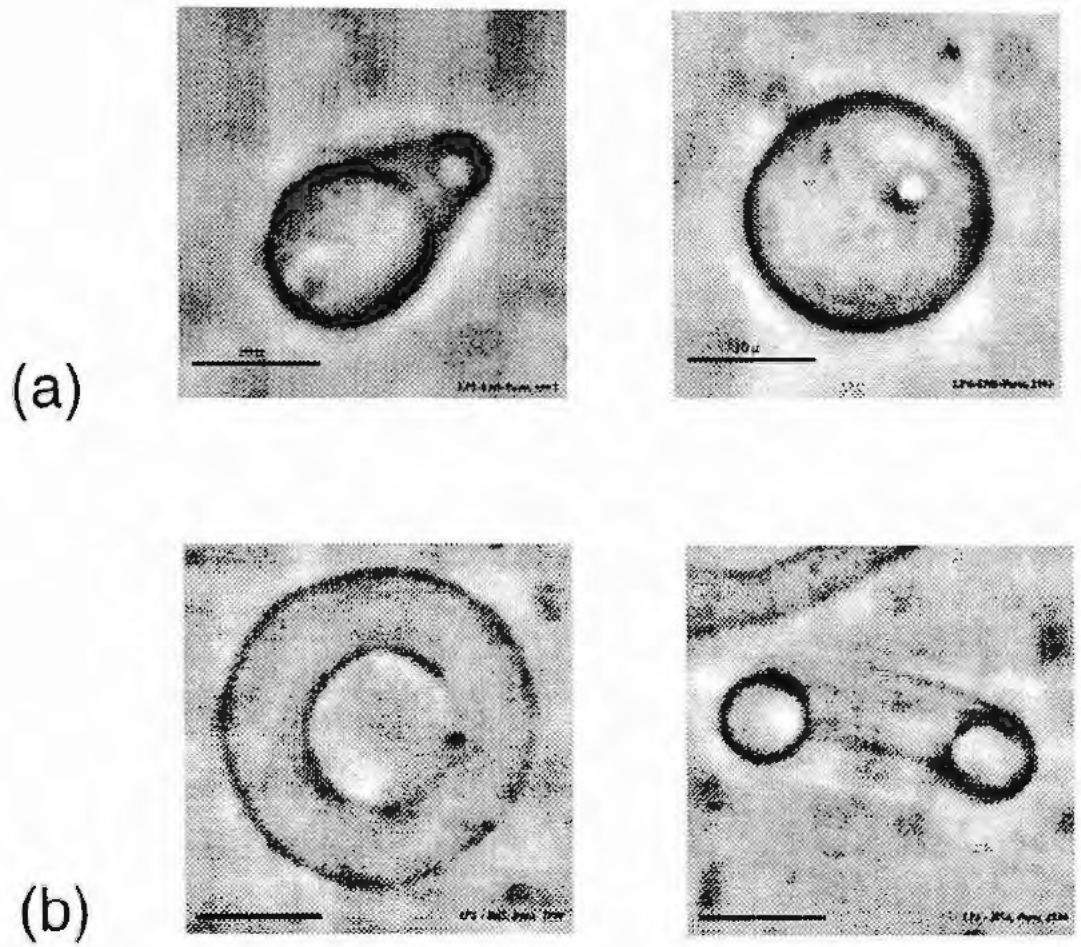

Figure 1.4: Toroidal vesicles. (a) a non-axisymmetric torus (b) an axisymmetric circular torus. The bar denotes $10\mu m$. (Michalet, 1994)

Figure 1.5: Three views on a vesicle with genus 2, the "button" surface. The bar denotes 10μm. (Michalet, 1994).

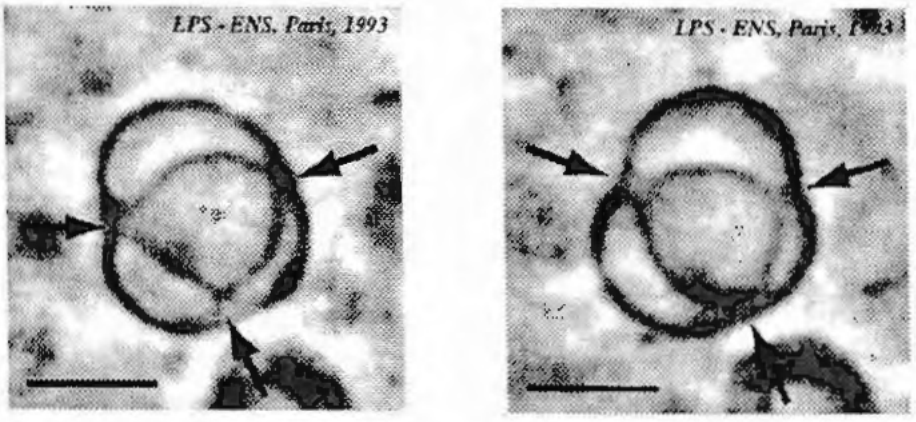

Figure 1.6: Vesicles of higher genus. The arrows point to necks whose positions strongly fluctuate. The bar denotes 10μm. (Michalet *et al.*, 1994)

Bending elasticity or, in its mathematical formulation, curvature energy not only generates a large variety of shapes. It also leads to different fluctuation or excitation spectra of these shapes and different dynamics than is shown by simple liquid interfaces. As will be seen, these phenomena require different mathematical tools for their description such as conformal transformations in three dimensions. The fact that these mathematical concepts become visible in the microscope definitely contributes to the appeal of these systems to statistical physicists. From a different perspective, these membranes also bear a close connection to certain string models studied in high-energy physics, since the world-sheet of a closed string is akin to a vesicle even though the embedding dimension in these string models may be much higher than three (Polyakov, 1987; Wheater, 1994).

A prime motivation to investigate membranes arises from biology in our three dimensional world. The lipid bilayer is the most elementary and indispensable structural component of biological membranes, which form the boundary of all cells and cell organelles (Alberts *et al.*, 1989). In biological membranes, the bilayer consists of many different lipids and other amphiphiles. As the cartoon shown in Fig. 1.7 illustrates, biomembranes are "decorated" with embedded membrane proteins, which ensure the essential functional properties of a biomembrane such as ion pumping, conversion from light energy to chemical energy and specific recognition. Often a polymeric network is anchored to the membrane endowing it with further structural stability. This stability is particularly spectacular in red blood cells which can squeeze through tiny capillaries and still recover their rest shape countless times in a life cycle.

Understanding the physical properties of the bilayer through the study of vesicles should provide valuable insight into the physical mechanisms that also govern the more complex biomembranes for which, from this perspective, the artificial vesicle is a model system. Striking phenomenological similarities between the budding transition as shown in Fig. 1.1 and exo-cytosis where small vesicles bud off the cell membrane encourage a thorough analysis of these artificial membranes.

Referring to the biological motivation, a distinction has been emphasized between classical "biophysics" and a field which acquired the somewhat fancy notion of "biologically inspired physics" (Peliti, 1991). While the former field is concerned with the detailed modelling of real biological processes – often at the cost of many parameters in a theoretical description – the latter approach takes the biological material as inspiration for asking questions biologists often may not even find relevant (yet). Even though the present work originates in the latter approach an optimist would hope for a reconciliation of these perspectives in the future. The impressive success biomedical applications of vesicles (often called "liposomes" in this field) have already reached in areas like drug delivery (Cevc, 1994; Lasic,

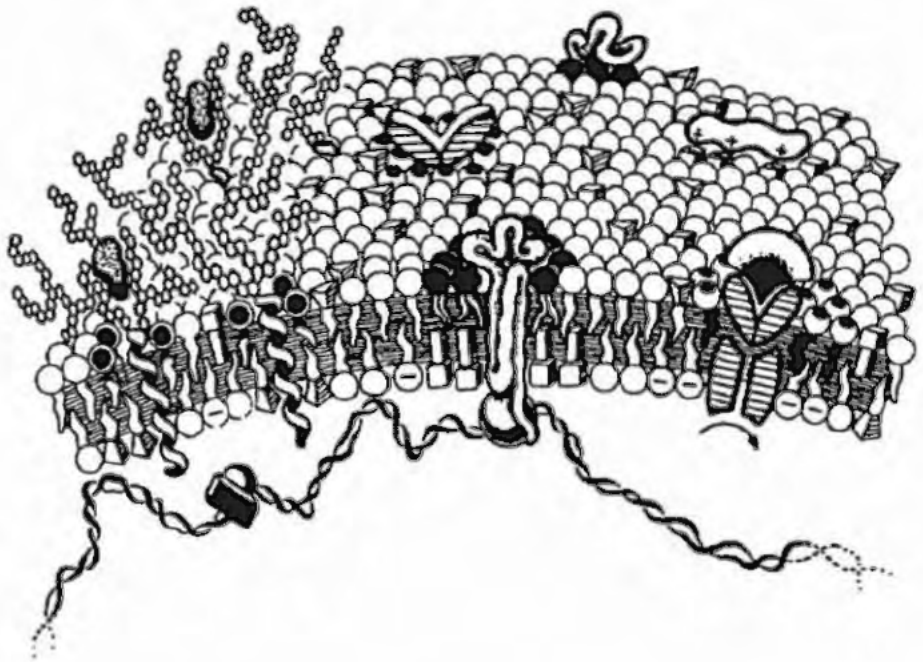

Figure 1.7: Cartoon of a biomembrane. (Sackmann, 1990).

1994) proves that at least some crucial mechanisms of biological systems have already been identified correctly by studying these model systems.

1.2 Overview

A systematic theory of vesicle conformations is the topic of this treatise.[5] "Conformations" is used here in a broad sense including not only the mean shapes as illustrated above but also the thermal excitations of these shapes, the shapes of vesicles adhering to a substrate and dynamical aspects of these conformations.

To transform the basic concept of curvature energy as introduced twenty years ago into a systematic quantitative theoretical description remained a challenge for quite some time. In particular, the implementation of the fact that the membrane is a bilayer (rather than a structureless monolayer) has been controversial, giving rise to various variants of curvature models which will be presented from a unifying point of view in Chapter 2. The starting point in this chapter is the trivial level of an almost planar membrane to which are introduced complications that arise from the closure of the membrane. The relationship between the

[5] In this overview, no references are given. They will appear in the main part.

various variants of the curvature model, which appear in the literature, are examined and incorporated under one general model.

In Chapter 3, the phase diagram, i.e. the shape of lowest energy for a certain set of parameters, is presented for the different variants of the curvature model. Such a study can become the basis for a comparison between theory and experiments as is discussed for the budding transition in some detail.

Due to the softness of the membrane, thermally excited shape fluctuations ("flickering") are visible under a microscope for most mean shapes. In Chapter 4, a theoretical approach for calculating thermal fluctuations around nontrivial mean shapes is introduced. The emphasis here is not on specific values but rather on introducing a scheme in which the role of the geometrical constraints present in various variants of the curvature model can be clarified. In particular, the fluctuations for "quasi-spherical" vesicles, which are spherical in the mean, are addressed. This case is important from an experimental perspective since the flicker spectrum yields the bending rigidity, which is the basic material parameter of fluid membrane. The range of validity of previous theoretical approaches is clarified.

Chapter 5 is devoted to the theory of vesicles of non-spherical topology. A variety of these shapes for genus 1 has been predicted independently from their experimental observation. In particular, the theory predicted the prominence of non-axisymmetric shapes. For genus 2 and higher, our theoretical analysis revealed that the shape of lowest energy should be one-fold continuously degenerate due to the conformal invariance of the curvature energy. Strong evidence for this phenomenon was found experimentally soon after.

Chapter 6 deals with a vesicle adhering to a substrate. This conformation has fundamental relevance since very often vesicles and membranes are not isolated but rather interacting with each other through a variety of forces. We focus on the shape change induced by adhesion and discuss in particular a novel transition caused by the competition between curvature and adhesion.

Chapter 7 is devoted to the dynamics of fluid membranes. Since the embedding of the membrane into the fluid is crucial to all dissipative processes, the full hydrodynamics of the coupled system comprising both the membrane and the embedding liquid has to be treated. For general conformations, this can become quite involved. We focus on the paradigmatic situation of an almost planar membrane and examine in particular the role of the coupling between the two monolayers on the damping of membrane fluctuations. The discussion of the dynamics of a bound membrane is motivated by recent experimental progress in this field.

A step towards biological membranes is presented in Chapter 8, where shape transforma-

tions of two-component vesicles are considered. A brief perspective concludes the treatise in Chapter 9.

While Chapter 2 and 3 constitute the basis of this work, the subsequent chapters can then be read almost independently. Before we start with the theory in Chapter 2, we provide below some background related to the chemistry and thermodynamics of lipids.

1.3 Chemistry and thermodynamics

Any theoretical treatment has to be aware of a few basic properties of the membrane resulting from their molecular architecture. The bilayers discussed in this work are formed by so-called lipids, which constitute a particular class of amphiphilic molecules. Lipids consist of a polar or negatively charged head group, which is highly soluble in water, and a hydrophobic part, which consists of two hydrocarbon chains (Cevc & Marsh, 1987). This structure is illustrated in Fig. 1.8 for a particular lipid, the phospholipid palmitoyl-oleoyl-phosphatidyl-choline (POPC). The various bilayer-forming lipids differ in the length of the hydrocarbon chains, the number of unsaturated bonds within a chain, the chemistry of the head group and of the backbone connecting chains and head (Marsh, 1990). For the mesoscopic conformation studied in this work, the molecular details are believed to be largely irrelevant, in the sense that they can be subsumed into effective elastic constants of the continuum theory described below.

Phase diagrams for the binary system that consists of lipid and water have been studied experimentally with a variety of techniques such as X-ray diffraction, electron microscopy, differential scanning calometry and NMR-spectroscopy (Marsh, 1990). Quite generally, these phase diagrams are governed by the amphiphilic nature of the lipid molecule, which tries to avoid contact of the chain region with water. Bilayer formation as one way to achieve this depends crucially on the molecular geometry of the amphiphile (Israelachvili, 1991). If the chain is too short, or the head is too bulky, the amphiphiles prefer to self aggregate into micelles, which are spherical (or cylindrical) conformations of a "monolayer" with no water in the interior.

In Fig. 1.9, the phase diagram for dimyristoyl phosphatidylcholine (DMPC)/water is shown. In large parts of the phase diagram, swollen bilayers are the stable phase. This lamellar phase is fluid at high temperature (the so-called L_α phase) whereas at low temperature, the bilayers become a two-dimensional gel ($L_{\beta'}$). For DMPC, there is also an intervening "ripple phase" with surface texture ($P_{\beta'}$). At very low water content, liquid crystalline phases form which may be cubic or hexagonal. The L_α phase can take up only a certain amount of water. Adding more water leads to phase coexistence between the L_α

phase and excess water.

Vesicles as they will be studied here belong to this excess water phase since typically only a very small amount of lipid is swollen with water. The thermodynamic properties of this excess water phase are not yet well characterized since topological equilibration requires too long a time for it to be experimentally accessible. One would expect that this phase is characterized by an equilibrium distribution of vesicles of different sizes and topologies (Helfrich, 1986; Morse & Milner, 1994a; Morse & Milner, 1994b).

An even richer phase behavior has been found for tensides, which are single chain amphiphiles, in water at high dilution. Such a system exhibits several vesicular phases and also a random bicontinuous phase, the so-called sponge phase, which have been identified experimentally (Hoffmann *et al.*, 1992) in agreement with theoretical predictions (Roux *et al.*, 1992; Porte, 1992). The larger stiffness of phospholipid bilayers, however, may prevent the formation of some of these phases, such as the sponge phase, by preempting the theoretically

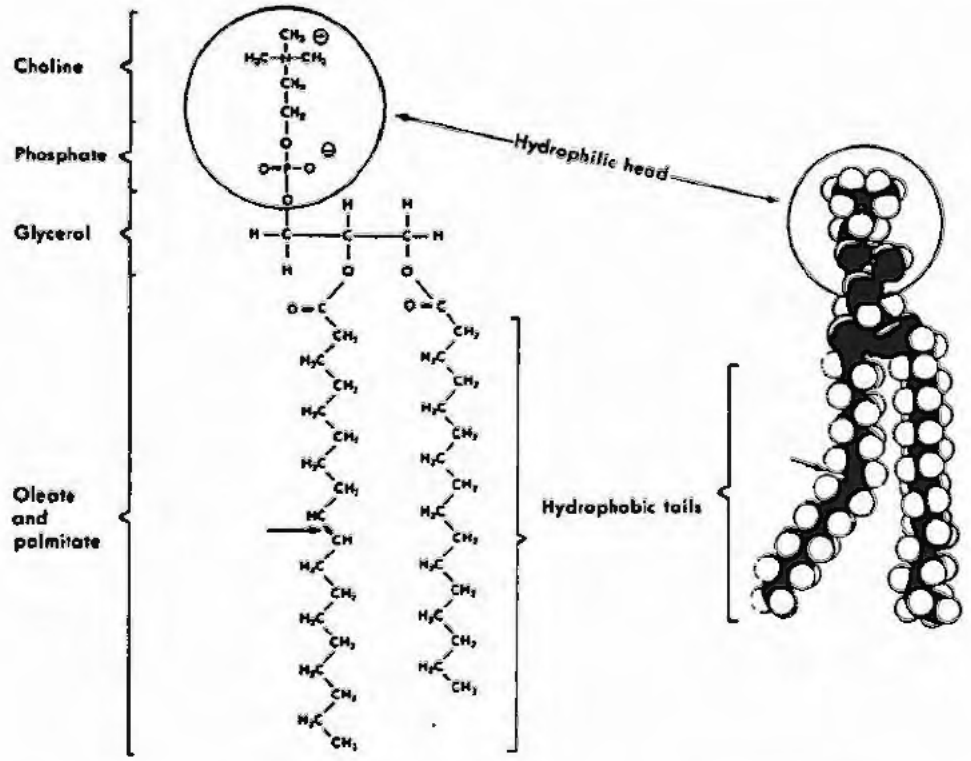

Figure 1.8: Molecular architecture of POPC, a particular phospholipid. (Robertis & E.M.F. De Robertis, 1980).

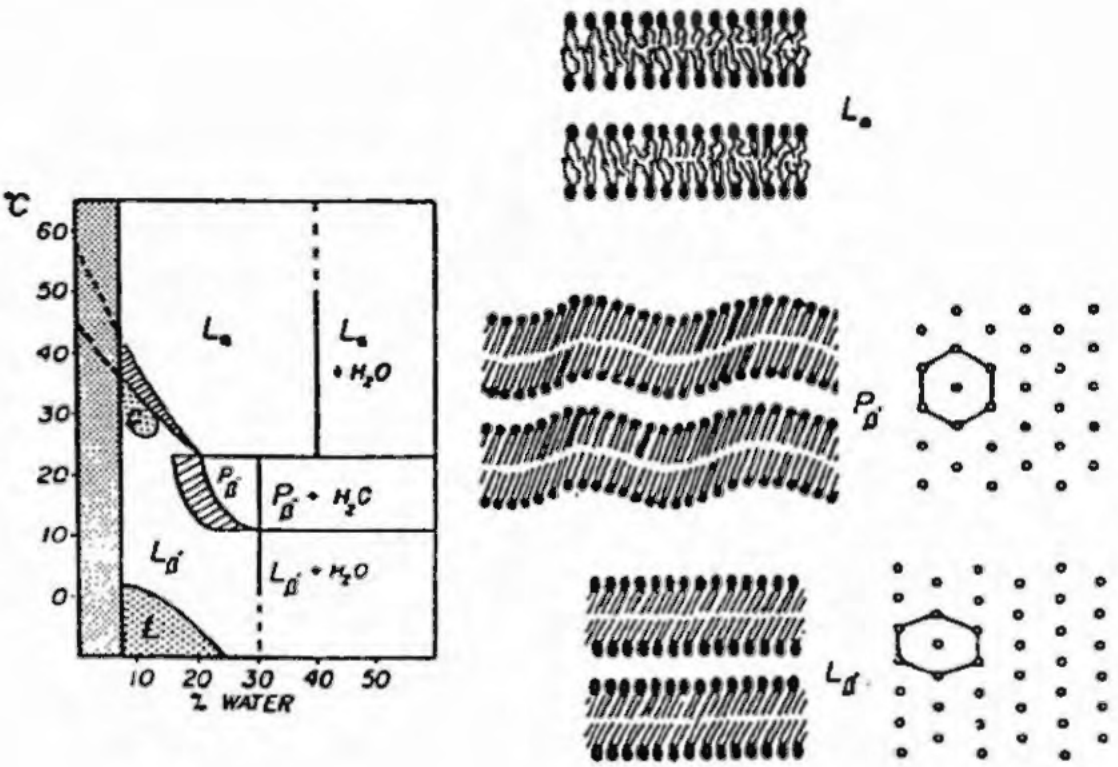

Figure 1.9: Phase diagram of DMPC/water. L_α, $L_{\beta'}$, and $P_{\beta'}$ denote the fluid lamellar, the gel and the ripple phase, respectively. (Janiak *et al.*, 1979).

expected second order transition to this phase with a strong first order transition (Helfrich, 1994).

As interesting as the issue of the global phase diagram may be, the problem of thermal equilibrium on very long time scales is fortunately mostly irrelevant as long as one focuses on *a* particular vesicle as seen in the microscope. Our "observables" will be quantities referring to this particular vesicle and not quantities characterizing a whole ensemble of vesicles. In this sense, the often made statement that "vesicles are only metastable" is somewhat misleading since it precludes the fact that on experimentally relevant time-scales (up to at least an hour) a vesicle can be considered as a system in a well-defined constrained equilibrium. The constraints characteristic for this equilibrium arise from physical properties of the bilayer as follows.

First, due to the strong hydrophobic effect, the concentration of "free" lipid molecules in aqueous solution is tiny, with a typical value of the order of 1 - 100 molecules per μm^3 (Marsh, 1990). Consequently, the number of lipid molecules within the bilayer is constant for a vesicle. This fact implies that the area of a vesicle is also constant at constant temperature since it can adjust to its optimal value. Moreover, even the number of molecule within each layer is practically constant since interchange of lipid molecules from one monolayer to the other is slow due to the large activation barrier for dragging a polar head group through the hydrocarbon chain region. Measurements of this flip-flop rate are somewhat controversial due to the various measurement techniques, but there is consensus that for phospholipids this time scale is of the order of hours (Homan & Pownall, 1988). However, there are amphihilic molecules that can be present as solutes in the bilayer, such as the biologically ubiquitous cholesterol, that are known to flip much faster between the layers (Backer & Dawidowicz, 1981).

Even though membranes are permeable to water, the enclosed volume of a vesicle is typically a constrained variable, too. The reason lies in the presence of molecules to which the membrane is impermeable such as sugar molecules or large ions, that are either deliberately added to the aqueous solution, or inevitably present in low concentration due to impurities. In either case, any net transfer of water would generate an osmotic pressure that cannot be counter-balanced by the relatively weak forces arising from additional bending of the membrane, as will be quantified in Sect. 2.4 below. Thus, the enclosed volume of a vesicle is controlled by the condition that basically no osmotic pressure builds up (Helfrich, 1973).

Chapter 2

Curvature models

In this chapter, we motivate, in three steps, the energy for any specific vesicle shape. First, the concept of local curvature energy in the classical model (Sect. 2.1) is discussed and its basic consequences are recalled (Sect. 2.2). Then, the refinement arising from the bilayer nature of the membrane is introduced (Sect. 2.3) and finally non-trivial effects arising form the closure of an open bilayer sheet to a vesicle is taken into account (Sect. 2.4). Since our treatment does not quite follow the chronology, a brief history of the various variants of the curvature models that appear in the literature is presented in Sect. 2.5 to give credit to previous work. Finally, the set of stationary shapes which follows from this curvature model is described in Sect. 2.6.

2.1 Local curvature energy in the classical model

Three or four orders of magnitude separate the thickness of the bilayer, which is about four nanometers, from the overall size of vesicles which are observable in the microscope. This separation of length-scales suggests a description of the membrane as a two-dimensional surface $\mathbf{R}(s_1, s_2)$ embedded in three-dimensional space. Here, s_1 and s_2 denote (arbitrary) internal coordinates. Such a surface can locally be characterized by its two radii of curvature R_1 and R_2, as shown in Fig. 2.1 . From the radii of curvature, both the mean curvature

$$H \equiv (1/R_1 + 1/R_2)/2, \tag{2.1}$$

and the Gaussian curvature

$$K \equiv 1/(R_1 R_2) \tag{2.2}$$

can be derived.

For a mathematical definition of these quantities, (see, e.g., (do Carmo, 1976)), one first

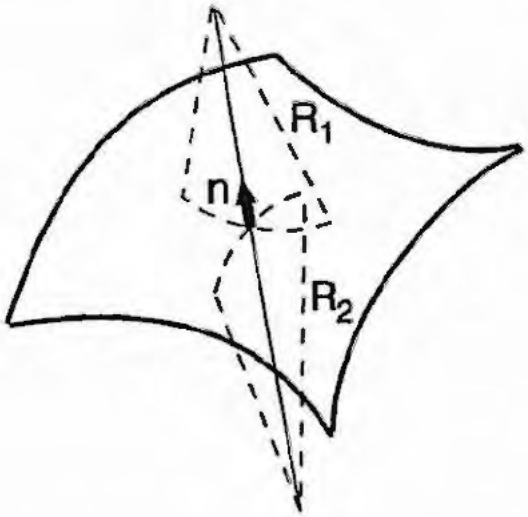

Figure 2.1: Curvature on a two-dimensional surface. The length scales R_1 and R_2 denote the radii of curvature. The vector n denotes the normal.

introduces the tangential vectors

$$\mathbf{R}_i \equiv \partial_i \mathbf{R}(s_1, s_2) \quad \text{for} \quad i = s_1, s_2, \tag{2.3}$$

from which one obtains the metric tensor

$$g_{ij} \equiv \mathbf{R}_i \cdot \mathbf{R}_j. \tag{2.4}$$

Its determinant, $g \equiv \det(g_{ij})$, yields the area element

$$dA = \sqrt{g}\, ds_1 ds_2. \tag{2.5}$$

The normal vector, $\mathbf{n}(s_1, s_2)$, is given by

$$\mathbf{n} = \frac{\mathbf{R}_1 \times \mathbf{R}_2}{|\mathbf{R}_1 \times \mathbf{R}_2|}. \tag{2.6}$$

Finally, the mean and the Gaussian curvature follow from the curvature tensor

$$h_{ij} \equiv (\partial_i \partial_j \mathbf{R}) \cdot \mathbf{n} \tag{2.7}$$

according to

$$H \equiv -\frac{1}{2} tr\ h^i_j \tag{2.8}$$

and

$$K \equiv det(h^i_j), \tag{2.9}$$

where $h^i_j \equiv g^{ik}h_{kj}$ and g^{ij} are the matrix elements of the (matrix) inverse of (g_{ij}). The minus-sign in Eq. (2.8) ensures a positive mean curvature for the sphere with the usual spherical coordinates ($s_1 = \theta, s_2 = \phi$), contrary to the convention used in differential geometry. Comparison of Eqs. (2.1) and (2.2) with Eqs. (2.8) and (2.9) shows that the radii of curvature are the negative inverse eigenvalues of the curvature tensor.

In the classical curvature model for symmetric membranes, the local bending energy f_0 of a non-flat membrane is written as an expansion in the curvature. To lowest order, one obtains (Canham, 1970; Helfrich, 1973)

$$f_0 \equiv (\kappa/2)(2H)^2 + \kappa_G K. \tag{2.10}$$

The two elastic constants κ and κ_G both have the dimension of an energy. They are called bending rigidity and Gaussian bending rigidity, respectively.

A constant term in the energy density (2.10) which would correspond to a "surface tension" or chemical potential for area has to be omitted. The fixed number of molecules in the membrane ensures a fixed internal area because stretching or compressing the membrane involves much larger energies than the cost of bending conformations. The absence of a surface tension distinguishes bilayer membranes fundamentally from liquid interfaces or even Langmuir monolayers, where interfacial area can be created or destroyed at a cost that is given by the surface tension. For an interface, the "interfacial" particles are the same as the bulk particles whereas a membrane consists of a fixed number of "particles" each of which can assume its preferred area in the conformations studied here.

2.2 Almost planar membrane and persistence length

Before we consider vesicles, it is instructive to recall some basic properties of the curvature energy for almost planar membranes. We use a Monge-representation for the displacements $h(\mathbf{x})$ of the membrane which is oriented in the $(z = 0)$−plane, with $\mathbf{x} = (x, y)$. The mean curvature is then given as (do Carmo, 1976)

$$2H = -\frac{\nabla^2 h + (\partial_x h)^2\partial_y^2 h + (\partial_y h)^2\partial_x^2 h - 2\partial_x h\partial_y h\partial_x\partial_y h}{(1+(\nabla h)^2)^{3/2}} = -\nabla^2 h(1 + O((\nabla h)^2)). \tag{2.11}$$

As will be discussed below, the Gaussian curvature is a total divergence and need not be considered here. Introducing a Fourier representation

$$h(\mathbf{x}) \equiv \int \frac{d^2q}{(2\pi)^2} h_{\mathbf{q}} e^{i\mathbf{q}\mathbf{x}}, \tag{2.12}$$

the bending energy is given by

$$F_0 \equiv \int dxdy\sqrt{g}f_0(x,y) \approx \frac{\kappa}{2}\int \frac{d^2q}{(2\pi)^2}q^4 h_{\mathbf{q}}h^*_{\mathbf{q}} \equiv \frac{1}{2}\int \frac{d^2q}{(2\pi)^2}E_0(q)h_{\mathbf{q}}h^*_{\mathbf{q}} \tag{2.13}$$

to lowest order, where * denotes the complex conjugate. Here, we have defined the "energy"

$$E_0(q) \equiv \kappa q^4 \tag{2.14}$$

of a bending mode.

The static correlation functions can easily be obtained from (2.13) as

$$< h_{\mathbf{q}}h^*_{\mathbf{q}'} >= \frac{T}{E_0(q)}(2\pi)^2\delta(\mathbf{q}-\mathbf{q}') = \frac{T}{\kappa q^4}(2\pi)^2\delta(\mathbf{q}-\mathbf{q}'), \tag{2.15}$$

where $< ... >$ is the thermal expectation value taken with the Boltzmann weight, $\exp(-F_0/T)$. Boltzmann's constant is set to unity throughout the article.

It is consistent to neglect the higher order terms in the expansion (2.13) as long as the expectation value $< (\nabla h)^2 >$ is small compared to 1. Using the correlation function (2.15), one finds

$$< (\nabla h)^2 >= \int \frac{d^2q}{(2\pi)^2}\int \frac{d^2q'}{(2\pi)^2}\mathbf{q}\mathbf{q}' < h_{\mathbf{q}}h^*_{\mathbf{q}'} >= \frac{T}{2\pi\kappa}\int_{1/L}^{1/a} dq/q = \frac{T}{2\pi\kappa}ln(L/a). \tag{2.16}$$

Here, L is the linear extension of the membrane and a is a molecular cut-off of the order of nanometers. Thus, the notion of an almost planar membrane is meaningful only if $L \ll L_p$ where the *persistence length* (de Gennes & Taupin, 1982)

$$L_p \equiv ae^{2\pi\kappa/T} \tag{2.17}$$

is also the correlation length for the normals.

If higher order terms occurring in the expansion (2.13) are treated perturbatively the result can be formulated as a length-dependent bending rigidity

$$\kappa(L) = \kappa - (c/4\pi)T\ln(L/a), \tag{2.18}$$

where L is the length-scale on which the membrane is bent. There has been some controversy about the correct value of the factor c.[1] Beyond the scale L_p, membrane conformations are characterized by irregular shapes for which self-avoidance becomes crucial.

[1] Depending on the measure used to integrate out the fluctuations, $c = 1$ has been found for the "curvature measure" (Helfrich, 1985; Helfrich, 1986; Helfrich, 1987) and $c = 3$ for the "displacement measure" (Peliti & Leibler, 1985; Förster, 1986; Kleinert, 1986). The latter value has recently been confirmed by Monte-Carlo simulations (Gompper & Kroll, 1994). Within a real-space renormalization group scheme, (Mecke, 1994) obtains $\alpha \simeq 1.4$ and an exponential dependence of the bending rigidity on length-scales beyond the persistence length.

For phospholipid membranes as studied here, the bending rigidity can be obtained from the flicker experiments analyzed with the spherical equivalent of the spectrum (2.15) as discussed in Sect. 4.2. The typical range of values $\kappa \simeq 10 - 25T$ leads to an astronomical persistence length $L_p \simeq a e^{60-150}$. This results shows that the concept of a mean orientation of the membrane makes sense for these bilayers.

A much smaller persistence length applies if so-called bola-lipids are added to the membrane (Duwe *et al.*, 1990). The corresponding vesicles have shown strong fluctuations. However, a naive application of the results developed here to this system is dangerous for two reasons. First, bola lipids are soluble in substantial fraction so that the concept of a vanishing surface tension may break down. Secondly, the local composition in mixed membranes can couple to the shape, which leads to spatial inhomogeneities as will be discussed in Chapter 8.

2.3 Coupling between curvature and density

Further analysis of the energy density (2.10) as described in Sect. 3.3 below shows that it cannot explain typical phenomena observed in shape transformations of vesicles such as the budding transition. The reason for this failure is its lack of any signature of the bilayer architecture. In fact, the energy (2.10) would be appropriate for a symmetric lipid monolayer for which so far no physical realization is known.

The bilayer aspect can easily be incorporated by "decorating" each side of the mathematical surface $\mathbf{R}(s_1, s_2)$ with a fluid of lipids as shown in Fig. 2.2 . Such a two-dimensional fluid can be characterized by its number densities $\phi^{\pm}(s_1, s_2)$. Deviations from the equilibrium density ϕ_0 cost an energy

$$f_1^{\pm} \equiv (k^m/2)(\phi^{\pm}/\phi_0 - 1)^2, \tag{2.19}$$

to lowest order in $\phi^{\pm}/\phi_0 - 1$. Here, k^m can be interpreted as the elastic compression modulus for the two-dimensional fluid within each monolayer. This elasticity acts in the so-called neutral surface of each monolayer. The neutral surface is defined by the property that bending and stretching are decoupled in energy when both deformations are defined with respect to it. The neutral surface of each monolayer is at a distance d from the bilayer mid-plane.

It will be very convenient to have all physical quantities defined on the bilayer midplane. Therefore, we project the densities $\phi^{\pm}$ onto this surface. If the membrane is curved, the projected densities $\phi^{\pm}_{proj}$ deviate from the densities $\phi^{\pm}$. To lowest order in dH, the relation

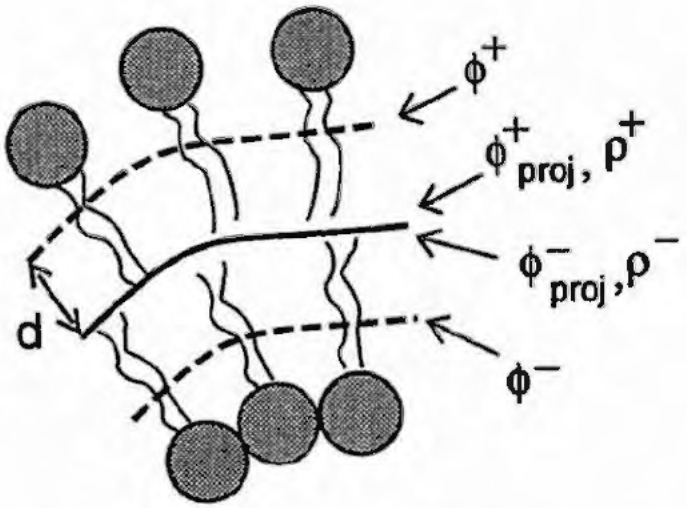

Figure 2.2: Cartoon of a *bilayer* membrane. The densities $\phi^{\pm}$ are defined on the neutral surfaces of the two monolayers shown as dashed lines. The projected densities $\phi^{\pm}_{proj}$ and the scaled quantities $\rho^{\pm}$ are defined on the bilayer midplane (dark line).

between both densities is given by

$$\phi^{\pm} = \phi^{\pm}_{proj}(1 \mp 2dH + O(d^2K)). \tag{2.20}$$

For small curvature, the elastic energy, $f_1^{\pm}$, can thus be written as

$$f_1^{\pm} = (k^m/2)(\rho^{\pm} \mp 2dH)^2, \tag{2.21}$$

where we introduce the reduced density deviations

$$\rho^{\pm} \equiv (\phi^{\pm}_{proj}/\phi_0 - 1). \tag{2.22}$$

The total energy of a symmetric bilayer membrane is thus given by (Seifert & Langer, 1993)

$$f \equiv f_0 + f_1^+ + f_1^- = \frac{\kappa}{2}(2H)^2 + \kappa_G K + \frac{k^m}{2}\left[(\rho^+ - 2dH)^2 + (\rho^- + 2dH)^2\right]. \tag{2.23}$$

We have retained the bending part of the classical model. Physically, it signifies the energy stored in the bending of each individual monolayer even if the lateral densities are adjusted to the shape in such a way that the contributions $f_1^{\pm}$ vanish.

The coupling between the local shape and the densities becomes more evident if we introduce the reduced density difference

$$\rho \equiv (\rho^+ - \rho^-)/2, \tag{2.24}$$

and the deviation

$$\bar{\rho} \equiv (\rho^+ + \rho^-)/2 \tag{2.25}$$

of the mean density form its equilibrium value. Using these quantities, the energy (2.23) can be written as

$$f = \frac{\kappa}{2}(2H)^2 + \kappa_G K + k^m \left[\bar{\rho}^2 + (\rho - 2dH)^2\right]. \tag{2.26}$$

Disregarding the phenomenological "derivation" of the energy (2.23) or (2.26) given here, one could also have postulated this form as following from two principles. First, the relevant "degrees of freedom" are identified, which are the "shape" and the two densities of the two monolayer liquids. Then, the energy is expanded in the lowest order terms in these variables taking into account the obvious symmetry requirements of a symmetric bilayer. The slight advantage of our presentation is the identification of the "coupling constant" between ρ and H as given by the material parameters $k^m d$. Along the same lines, it should be clear that there will be all sorts of higher order terms which are compatible with the symmetry of the membrane. For instance, we have not treated any explicit interaction between the two layers but rather postulated a fixed distance d. On a more microscopic level, one could expect that the local distance or thickness of the membrane depends on its local lateral density. Thus, one could introduce a field for the deviations from the mean thickness d which, however, would not couple to the shape H nor to ρ in quadratic order by symmetry.

For a discussion of small displacements about the almost planar shape for the bilayer energy, the reduced densities are expanded as

$$\rho^{\pm}(\mathbf{x}) \equiv \int \frac{d^2q}{(2\pi)^2}(\bar{\rho}_\mathbf{q} \pm \rho_\mathbf{q})e^{i\mathbf{q}\mathbf{x}}. \tag{2.27}$$

The total energy of a bilayer membrane, thus, becomes

$$F \equiv \int \frac{d^2q}{(2\pi)^2} f_\mathbf{q} \equiv \frac{1}{2}\int \frac{d^2q}{(2\pi)^2}(h_\mathbf{q}, \rho_\mathbf{q}, \bar{\rho}_\mathbf{q})\mathbf{E}(q)\begin{pmatrix} h_\mathbf{q} \\ \rho_\mathbf{q} \\ \bar{\rho}_\mathbf{q} \end{pmatrix}^*, \tag{2.28}$$

with the "energy" matrix

$$\mathbf{E}(q) \equiv \begin{pmatrix} \tilde{\kappa}q^4 & -2k^m dq^2 & 0 \\ -2k^m dq^2 & 2k^m & 0 \\ 0 & 0 & 2k \end{pmatrix}, \tag{2.29}$$

where the renormalized bending rigidity $\tilde{\kappa}$ is defined by

$$\tilde{\kappa} \equiv \kappa + 2d^2 k^m. \tag{2.30}$$

Minimizing the single mode energy $f_{\mathbf{q}}$ in Eq. (2.28) with respect to $\rho_{\mathbf{q}}$ leads to

$$\rho_{\mathbf{q}}^{min}(h_{\mathbf{q}}) = dq^2 h_{\mathbf{q}}. \tag{2.31}$$

Using this relation in (2.28), we recover the energy of the classical model

$$f_{\mathbf{q}}(h_{\mathbf{q}}, \rho_{\mathbf{q}}^{min}, \bar{\rho}_{\mathbf{q}} = 0) = \frac{\kappa}{2} q^4 h_{\mathbf{q}} h_{\mathbf{q}}^*. \tag{2.32}$$

This shows that the classical model implicitly assumes that the densities in each monolayer adjust optimally to the local shape, i.e., in the classical model bending takes place at a relaxed lateral density within each monolayer.

For bending at "frozen" density $\rho^{\pm} = 0$, we get

$$f_{\mathbf{q}}(h_{\mathbf{q}}, \rho_{\mathbf{q}} = 0, \bar{\rho}_{\mathbf{q}} = 0) = \frac{\tilde{\kappa}}{2} q^4 h_{\mathbf{q}} h_{\mathbf{q}}^*. \tag{2.33}$$

Whether the difference between bending at relaxed and bending at frozen densities is significant depends on the relative magnitude of κ and $\tilde{\kappa}$. For a simple estimate, we assume that each monolayer is a homogeneous thin plate of thickness $2d$. For such a plate, the bending rigidity κ^m (with a superscript for "monolayer") and the area compression modulus k^m are related by (Landau & Lifshitz, 1989)

$$\kappa^m = k^m d^2/3. \tag{2.34}$$

With the bending rigidity of the bilayer $\kappa = 2\kappa^m$ and Eq. (2.30), we find $\tilde{\kappa} = 4\kappa$. This significant difference shows that lateral relaxation is an important factor in bending deformations (Evans, 1974; Helfrich, 1974). Two effects can impede this lateral relaxation. First, lateral relaxation is effective only if the time–scale associated with this relaxation is faster than a typical time–scale for the bending lateral relaxation. This issue will be addressed in Chapter 7 below. Secondly, lateral relaxation implicitly assumes a reservoir of lipid molecules at the boundaries. For closed membranes such a reservoir is not available, leading to consequences discussed in the next section.

We close this section by quoting the static correlation functions which follow from (2.28)

$$\begin{aligned} < \begin{pmatrix} h_{\mathbf{q}} \\ \rho_{\mathbf{q}} \\ \bar{\rho}_{\mathbf{q}} \end{pmatrix} (h_{\mathbf{q}'}, \rho_{\mathbf{q}'}, \bar{\rho}_{\mathbf{q}'})^* > &= T\mathbf{E}^{-1}(q)(2\pi)^2 \delta(\mathbf{q} - \mathbf{q}') \\ &= T \begin{pmatrix} 1/\kappa q^4 & dq^2/\kappa & 0 \\ dq^2/\kappa & \tilde{\kappa}/2k^m\kappa & 0 \\ 0 & 0 & 1/2k^m \end{pmatrix} (2\pi)^2 \delta(\mathbf{q} - \mathbf{q}'). \end{aligned} \tag{2.35}$$

2.4 Global energy of a vesicle shape

The energy of a closed membrane conformation follows from integrating the energy density (2.26) over the closed vesicle surface. This leads to the total energy of a vesicle,

$$F = \frac{\kappa}{2}\oint dA(2H)^2 + \kappa_G \oint dA\ K + k^m \oint dA(\rho - 2dH)^2 + k^m \oint dA\bar{\rho}^2 + F_V \qquad (2.36)$$

as a sum of five contributions which we now discuss in detail.

2.4.1 Gauss-Bonnet-theorem

The second integral in the energy (2.36) does not depend on the specific shape of the vesicle. Due to the Gauss-Bonnet theorem (see e.g. (do Carmo, 1976)), this term is the topological invariant $\kappa_G 4\pi(1-g)$, where g is the genus, i.e., the number of handles, of the vesicle. For any fixed topology, this energy can be neglected. We will proceed to do so by formally setting $\kappa_G = 0$.

2.4.2 Osmotic pressure

The last term, F_V, in the energy (2.36) arises from the presence of molecules in the solution, such as large ions or sugar molecules, to which the membrane is impermeable on the time scales considered here. With c as the total concentration in mols per volume of these osmotically active molecules, there arises an osmotic pressure

$$\Pi \equiv R_g T(n/V - c), \qquad (2.37)$$

where $R_g \simeq 8.31 J/(molK)$ is the gas constant, V the volume of the vesicle and n the total number of moles of these molecules caught within the vesicle. For simplicity, an ideal solution was assumed. Such an osmotic pressure leads to the energy

$$F_V(V) \equiv \int_{V_0}^{V} dV' \Pi(V') = R_g T[n\ln(V/V_0) - c(V - V_0)] \approx \frac{R_g T c V_0}{2}\left(\frac{V}{V_0} - 1\right)^2. \qquad (2.38)$$

The latter approximations holds for small $V/V_0 - 1$, where

$$V_0 \equiv n/c \qquad (2.39)$$

is the volume for which the osmotic pressure vanishes.

2.4.3 Minimizing with respect to lipid densities

First, the energy F is minimized with respect to the density variables ρ and $\bar{\rho}$ taking into account that the number N^+ and N^- of lipid molecules within each layer is conserved. Using

$$N^{\pm} = \oint dA \phi^{\pm}_{proj} \tag{2.40}$$

and the definitions (2.22),(2.24) and (2.25), this conservation implies the integral constraints

$$\int dA\bar{\rho} = \int dA[(\phi^+_{proj} + \phi^-_{proj})/\phi_0 - 1] = (N^+ + N^-)/(2\phi_0) - A, \tag{2.41}$$

where A is the total area of the vesicle and

$$\int dA\rho = \frac{1}{2}\int dA(\phi^+_{proj} - \phi^-_{proj})/\phi_0 = (N^+ - N^-)/(2\phi_0). \tag{2.42}$$

If these constraints are added with Lagrange multipliers to the energy F, minimization at fixed shape (and, thus, at fixed area A) immediately leads to a constant mean density given by

$$\bar{\rho} = (N^+ + N^-)/(2\phi_0 A) - 1. \tag{2.43}$$

For the local density difference, minimization shows that the density difference follows the local mean curvature according to

$$\rho(s_1, s_2) - 2dH(s_1, s_2) = -2dM/A + (N^+ - N^-)/(2\phi_0 A), \tag{2.44}$$

where

$$M \equiv \oint dAH \tag{2.45}$$

is the total (integrated) mean curvature. The geometrical quantity M also determines the actual area difference

$$\Delta A = 4dM + O(d^2) \tag{2.46}$$

between the neutral surfaces of the two monolayers which will, in general, differ from the optimal area difference

$$\Delta A_0 \equiv (N^+ - N^-)/\phi_0, \tag{2.47}$$

which is determined by the number of molecules in each layer.

If the expressions (2.44) and (2.43) for the density variables are inserted into the energy (2.36), one obtains an energy

$$\begin{aligned} F \equiv\ & (\kappa/2)\oint dA(2H)^2 + \frac{k^m}{4A}(\Delta A - \Delta A_0)^2] \\ & + k^m A[(N^+ + N^-)/(2\phi_0 A) - 1]^2 + \frac{R_g T c V_0}{2}\left(\frac{V}{V_0} - 1\right)^2. \end{aligned} \tag{2.48}$$

2.4.4 Effective constraint on area and volume

A convenient simplification arises from the fact that there are two well-separated energy scales present in the four terms of the energy (2.48). The first and the second terms both are, as shown below, of the order κ. The third term depends strongly on the total area of the vesicle. For a large vesicle with $A = 1000\mu\text{m}^2$, and the typical material constants $k = 10^2\text{erg/cm}^2$, and $\kappa = 10^{12}\text{erg}$ (Evans & Needham, 1987), the energy scale of this term, $k^m A \simeq 10^9\kappa$ vastly exceeds the energy of the curvature elasticity. Thus, one can determine the area A by the requirement that the third term vanishes. This leads to the area constraint

$$A = (N^+ + N^-)/(2\phi_0) \equiv 4\pi R_0^2, \tag{2.49}$$

given by the mean number of lipid molecules in the two layers. For later reference, we define here an equivalent sphere radius R_0.

Likewise, the energy scale involving osmotic differences, $RTcV_0/2 \simeq 10^3\kappa$, for the typical values $R_0 = 10\mu\text{m}$ and $c = 10^{-4}\text{mol/m}^3$ as a typical sugar concentration, shows that only minute concentration differences between interior and exterior solution of the order of 10^{-7}mol/m^3 can be balanced by the curvature energy. To an excellent approximation, the volume is thus constraint to the value $V_0 = n/c$ for which the osmotic pressure vanishes (Helfrich, 1973). Any change in the ambient osmotic conditions will lead to an adaption of the vesicle volume such that the resulting osmotic pressure difference effectively vanishes again.

From a theoretical point of view, one could easily proceed without making these two simplifications even though they are convenient and well-justified for giant vesicles. In fact, the theory as developed in the next chapter also captures the more general case where volume and area are subject to the energy terms present in (2.48).

2.4.5 Area-difference-elasticity model

If the terms in the second line of the energy (2.48) are thus replaced by hard constraints on the area and volume, one obtains the so–called area–difference–elasticity (ADE)-model in which the energy of a vesicles is given by (Seifert *et al.*, 1991a; Wiese *et al.*, 1992; Bozic *et al.*, 1992; Miao *et al.*, 1994)

$$W \equiv \kappa \left[G + \frac{\alpha\pi}{8Ad^2}(\Delta A - \Delta A_0)^2 \right], \tag{2.50}$$

with the dimensionless "local" bending energy

$$G \equiv (1/2) \oint dA(2H)^2 \tag{2.51}$$

and the dimensionless material parameter

$$\alpha \equiv 2k^m d^2/(\pi\kappa). \tag{2.52}$$

The second term in (2.50) is the so-called area-difference elasticity or non-local curvature energy. In the form $\alpha\kappa$, the elastic constant in front of this term is sometimes called the non-local bending rigidity. If one assumes that the monolayers are homogeneous sheets of thickness $2d$, one obtains with (2.34) the estimate $\alpha = 3/\pi \simeq 1$. However, it may be advisable to leave the value of α open and treat it as an independent material parameter because the ADE model may be applicable even if a simple relation like (2.34) breaks down due to the internal structure of the monolayer. Corrections to the energy (2.50) can be expected to be of the order of d/R_0, which is the basic expansion parameter of these curvature models for symmetric membranes.

2.5 A brief history of variants of the curvature model

The derivation of the ADE model given above reflects an evolution of curvature models dating to their first appearance in the early seventies. All these models can be cast in a form amounting to special cases of a generalized ADE model.

In this section, we introduce these variants roughly according to their historical occurrence not only in order to assign credit for the essential steps. Considerable parts of the literature still deal with these variants especially since they contain typically one less parameter than the ADE model. We will also have to specialize to these limiting cases sometimes in later chapters.

2.5.1 Minimal model: local curvature energy only

The first description of fluid membranes by a curvature model is given by (Canham, 1970), in which the local energy density of the form $\sim (1/R_1^2 + 1/R_2^2) = (2H)^2 - 2K$ is introduced. Since the Gaussian term is irrelevant for all but topological transformations, this model amounts to retaining just the local curvature energy from (2.50). For later reference, we define the energy of this "minimal model" as

$$F_M \equiv \kappa G. \tag{2.53}$$

From the present perspective, this energy is a faithful description of a vesicle which consists of a symmetric bilayer with rapid flip-flop of the lipid molecules. While it is known that cholesterol flips quite rapidly between the two layers (Backer & Dawidowicz, 1981) pure

cholesterol does not form bilayers. For vesicles consisting of mixtures, however, the presence of two components leads to an additional degree of freedom which has to be taken into account as discussed in Chapter 8. Likewise, lipid molecules with two polar head groups connected by hydrocarbon chains such as the bola lipids (Marsh, 1990) would constitute a model system for this minimal model. Again, these molecules can be added to a lipid bilayer but they are not able to form bilayers as a single component system. Thus, there is not yet a genuine physical realization of this "minimal model".

2.5.2 Spontaneous curvature model

Helfrich in a seminal paper introduced the energy

$$F_{SC} \equiv \frac{\kappa}{2} \oint dA (2H - C_0)^2, \tag{2.54}$$

where the so-called spontaneous curvature C_0 is supposed to reflect a possible asymmetry in the membrane (Helfrich, 1973). The energy (2.54) together with constraints on the total area and the enclosed volume defines the spontaneous-curvature (SC) model.[2] The physical origin of the spontaneous curvature could be either a different chemical environment on both sides of the membrane, or a different chemical composition of the two monolayers. In the latter case, however, the fluidity of the lipids will lead to a lateral adjustment of the local composition to the local curvature, i.e., to the local shape, as we will discuss in Chapter 8. The spontaneous curvature then becomes a dynamical variable and is no longer constant over the vesicle surface. Indeed, the spontaneous curvature has remained elusive since there seem to be no measurements of this quantity for phospholipid vesicles.

2.5.3 Bilayer couple model

In a complementary approach, building on the earlier work (Sheetz & Singer, 1974; Evans, 1974; Evans, 1980b), Svetina and Zeks[3] introduced the so-called bilayer couple (BC-) model, in which a hard constraint on the area difference ΔA, i.e., $\alpha = \infty$, is imposed. Thus, this model is defined by the energy (2.53) together with the three constraints on area, volume and total mean curvature. In view of the derivation given above for the ADE model, the bilayer couple model can be rationalized by assuming the monolayers as incompressible but still bendable. Any spontaneous curvature is irrelevant in the BC model since it would add only a constant term to the energy at constant ΔA (Seifert *et al.*, 1991b).

[2] An alternative formulation of the spontaneous curvature model has been suggested recently in (Fischer, 1993).

[3] (Svetina *et al.*, 1982; Svetina & Zeks, 1983; Svetina & Zeks, 1989)

Model	Energy	Constraints
Minimal	$F_M \equiv \kappa G$	A, V
BC	$F_M \equiv \kappa G$	A, V, M
ADE	$W \equiv \kappa[G + (\alpha/2)(m - m_0)^2]$	A, V
SC	$F_{SC} \equiv \kappa(G - c_0 m + 2\pi c_0^2)$	A, V
ADE-SC	$W_{SC} \equiv \kappa[G - c_0 m + 2\pi c_0^2 + (\alpha/2)(m - m_0)^2]$	A, V

Table 2.1: Variants of the curvature models

2.5.4 Area-difference-elasticity model

The physical effect of the area-difference-elasticity has been appreciated early on in (Helfrich, 1974) and, in particular, in (Evans, 1974; Evans, 1980b). The model as defined in Eq. (2.50) has been introduced independently by three groups (Seifert *et al.*, 1991a; Wiese *et al.*, 1992; Bozic *et al.*, 1992). The derivation as presented above is original although related to the one given in (Miao *et al.*, 1994).

2.5.5 Area-difference elasticity model with spontaneous curvature

The ADE model can also be derived if the two monolayers are asymmetric in the first place (Miao *et al.*, 1994). This leads to a systematic spontaneous curvature which amounts to replacing $(2H)^2$ by $(2H - C_0)^2$ in (2.50). However, at constant area A and optimal area-difference $\widehat{\Delta A_0}$, the latter model is equivalent to the ADE model without spontaneous curvature but with a renormalized area–difference ΔA_0 given by (Miao *et al.*, 1994)

$$\Delta A_0 = \widehat{\Delta A_0} + 8\pi C_0 d R_0^2/\alpha. \tag{2.55}$$

Thus, within the ADE model the spontaneous curvature leads only to a trivial modification. Only for the limit $\alpha \to 0$ must one include a spontaneous curvature in order to end up with the SC model. If the limit $\alpha \to 0$ is taken in the energy (2.50), one recovers the minimal model (2.53).

2.5.6 Summary of curvature models

For later reference, the energy and the applicable constraints on the various models are summarized in Table 2.1 It is useful to introduce scaled quantities as follows. The reduced

mean curvature m, the reduced optimal area-difference m_0, and the reduced spontaneous curvature c_0 are defined by

$$m \equiv M/R_0, \qquad m_0 \equiv \Delta A_0/(4dR_0), \quad \text{and} \quad c_0 \equiv C_0 R_0. \tag{2.56}$$

2.6 Stationary shapes

Vesicles will acquire the shape at which their curvature energy subject to the appropriate constraints is minimal. This basic premise of the approach using curvature models assumes both that non-equilibrium effects such as convection and temperature gradients are small, and that the effect of thermal fluctuations on the shape can be neglected. While the former assertion has to be taken cared of by the experimentalist, the latter holds in first approximation since the bending rigidity is still large compared to a thermal energy. How to incorporate the effect of thermal fluctuations around the shape of lowest energy will be discussed in Chapter 4.

The search for the shape of lowest energy proceeds in three steps. First, the set of *stationary shapes* is determined for which the first variation of the appropriate energy, subject to the applicable constraints, vanishes. This set includes local minima as well as saddle points. Secondly, saddle points are excluded leading to the set of *locally stable shapes*. Finally, if there are several local minima for the same control parameters, the energies of these shapes are compared with each other to find the shape of lowest energy.

2.6.1 General energy functional and equivalence of the ensembles

We first show that the set of stationary shapes is the same for all variants of the curvature energy (except the minimal model which contains only a subset). Consider the general variational free-energy

$$\Phi[S] = \kappa G[S] + \Sigma A[S] + PV[S] + QM[S], \tag{2.57}$$

where the dimensionless local curvature energy G has been defined in Eq. (2.51) and $[S]$ denotes symbolically the dependence on the shape S. The parameters Σ, P and Q will be specified later. The stationarity condition for the functional $\Phi[S]$ formally reads

$$\delta^1\Phi[S] = \kappa\delta^1 G[S] + \Sigma\delta^1 A[S] + P\delta^1 V[S] + Q\delta^1 M[S] = 0, \tag{2.58}$$

where δ^1 denotes the first variation. The set of stationary shapes $\mathcal{S}_\Phi$ contains all shapes which obey this equation as Σ, P and Q are varied. In the BC-model, Σ, P and Q are

Model	$g(A,V,M) - PV$	Σ	Q
Minimal	$\Sigma_M A$	Σ_M	0
BC	$\Sigma A + QM$	Σ	Q
ADE	$\Sigma_{ADE} A + (\alpha/2)\kappa(M - M_0)^2/R_0^2$	Σ_{ADE}	$\alpha\kappa(M - M_0)$
SC	$\Sigma_{SC} A - \kappa C_0 M + \kappa C_0^2 A/2$	$\Sigma_{SC} + \kappa C_0^2/2$	$-2\kappa C_0$
ADE-SC	$\Sigma_{ADE-SC} A - \kappa C_0 M$ $+\kappa C_0^2 A/2 + \alpha/2\kappa(M - M_0)^2/R_0^2$	$\Sigma_{ADE-SC} + \kappa C_0^2/2$	$-2\kappa C_0 + \alpha\kappa(M - M_0)$

Table 2.2: Parameters in the various models

Lagrange multipliers chosen such that the area A, the volume V and the integrated mean curvature M acquire the appropriate values. These Lagrange parameters fulfill the relations

$$\Sigma/\kappa = -\frac{\partial G}{\partial A}_{|V,M}, \quad P/\kappa = -\frac{\partial G}{\partial V}_{|A,M}, \quad \text{and} \quad Q/\kappa = -\frac{\partial G}{\partial M}_{|A,V}. \tag{2.59}$$

We now show that the set $\mathcal{S}_\Phi$ contains as a subset the set of stationary shapes $\mathcal{S}_B$ which belong to the energy B of the general form

$$B \equiv \kappa G + g(A,V,M), \tag{2.60}$$

where $g(A,V,M)$ is an arbitrary function. Such an energy, e.g., has been encountered during the derivation of the ADE model where the last three terms of the energy F in Eq. (2.48) are of this type. If there are constraints, $g(A,V,M)$ has to include terms of the type $\Sigma_B A$, $P_B V$ and $Q_B M$, where, e.g., Σ_B is the Lagrange multiplier for the area. The stationarity condition for the energy B is

$$\delta^1 B \equiv \kappa\delta^1 G + \frac{\partial g}{\partial A}\delta^1 A[S] + \frac{\partial g}{\partial V}\delta^1 V[S] + \frac{\partial g}{\partial M}\delta^1 M[S] = 0. \tag{2.61}$$

A comparison of (2.61) with (2.58) shows that any stationary shape of the energy B is also stationary for Φ provided the parameters Σ, P and Q are chosen according to

$$\Sigma = \frac{\partial g}{\partial A}, P = \frac{\partial g}{\partial V}, \quad \text{and} \quad Q = \frac{\partial g}{\partial M}. \tag{2.62}$$

Note that the reverse is not quite true. Depending on the specific form of g, there may be values of Σ, P and Q which are not accessible through (2.62). Specializing the energy B to the various variants of the curvature models discussed above, we collect the interpretation of the parameters Σ, P and Q for the respective models in Table 2.2. In all cases, P is the Lagrange multiplier that ensures the constraint on area. For historical reasons, we will often replace Q by $-2\kappa C_0$ in the rest of this article.

2.6.2 Shape equation and scale invariance of the local curvature energy

The formal shape equation (2.58) corresponds to a partial differential equation for the shape. This equation can be derived by paramterizing small deviations around a stationary shape $\mathbf{R}_0(s_1, s_2)$ by

$$\mathbf{R}(s_1, s_2) = \mathbf{R}_0(s_1, s_2) + \epsilon(s_1, s_2)\mathbf{n}(s_1, s_2), \tag{2.63}$$

where $\mathbf{n}(s_1, s_2)$ is the local normal vector. The stationarity condition $\delta\Phi/\delta\epsilon(s_1, s_2) = 0$ (2.58) then becomes[4]

$$P + 2\Sigma H - 2\kappa[2H(H^2 - K) + C_0 K - \Delta H] = 0. \tag{2.64}$$

Here

$$\Delta \equiv (1/\sqrt{g})\partial_i(g^{ij}\sqrt{g}\partial_j) \tag{2.65}$$

is the Laplace–Beltrami operator on the surface. For $\kappa = 0$, this equation corresponds to Laplace's equation which describes the balance of pressure and surface tension for soap films. For finite bending rigidity, bending moments contribute to this force balance.

An important general statement about the solutions of the fourth order partial differential equation (2.64) follows from the scale invariance of the local curvature energy G. This energy does not depend on the size of the vesicle but only on its shape. If $\mathbf{R}_0(s)$ is a solution to (2.64), the rescaled shape $\mathbf{R}_0(s) \to \mathbf{R}_0(s)/\lambda$, with $\lambda > 0$, is also a solution provided $\Sigma \to \lambda^2\Sigma$, $P \to \lambda^3 P$ and $C_0 \to \lambda C_0$ are rescaled properly. Writing $\lambda = 1 + \epsilon$, one obtains from the stationarity condition (2.58), the homogeneity relation

$$2\Sigma A + 3PV + QM = 0. \tag{2.66}$$

Because of the scale invariance, it is sufficient to consider the solutions of the shape equation at fixed C_0, where the two possible signs for C_0 as well as $C_0 = 0$ have to be considered separately. The solutions to (2.64) then depend only on the two parameters ΣC_0^2, and PC_0^3. Since for any given value of these two parameters one will, in general, find a discrete set of solutions to (2.64), the set of all solution to (2.64) is a two-dimensional manifold with countable degeneracy if trivial rescalings are ignored. Rather than characterizing these shapes by the values of ΣC_0^2 and PC_0^3, we will use two geometrical quantities, the reduced volume

$$v \equiv \frac{V}{(4\pi/3)R_0^3} \leq 1, \tag{2.67}$$

(where equality holds for the sphere only) and the integrated mean curvature $m > 0$ defined in Eq. (2.56).

[4]This form is trivially different from the one derived in (Ou-Yang & Helfrich, 1989) since (i) we have a different sign convention for H and (ii) in (Ou-Yang & Helfrich, 1989) the SC model was used in which the term $\sim C_0^2$ leads to a shift in the tension Σ.

2.6.3 Expansion around the sphere

The only known analytical solution of spherical topology of (2.64) is the sphere. Indeed, inserting a sphere with radius R_0 into (2.64) shows that it is a solution whenever

$$PR_0 + 2\Sigma - \kappa C_0/R_0 = 0. \tag{2.68}$$

Some insight into the structure of solutions to (2.64) can be gained by an expansion around the sphere. A slightly deformed sphere can be parametrized by spherical harmonics $Y_{lm}(\theta,\phi)$) according to

$$R(\theta,\phi) = R_0(1 + \sum_{l\geq 0,m} u_{l,m} Y_{lm}(\theta,\phi)), \tag{2.69}$$

where $|m| \leq l$ and $u_{l,-m} = (-1)^m u^*_{l,m}$.

Whenever the second variation of Φ,

$$\delta^2\Phi = (\kappa/2R_0^2) \sum_{l\geq 0,m} |u_{l,m}|^2[l(l+1) - 2][l(l+1) - C_0R_0 - PR_0^3/2\kappa], \tag{2.70}$$

vanishes around the sphere, stationary shapes bifurcate from it. Here, the stationarity (2.68) has been used to eliminate Σ. The second variation $\delta^2\Phi$ does not depend on m for symmetry and is identical to zero for the $(l = 1)-$modes which correspond to rigid translations of the sphere. With increasing P, the sphere thus becomes unstable with respect to deformations with index l at a critical pressure (Ou-Yang & Helfrich, 1987; Peterson, 1988),

$$P_c(l)R_0^3/\kappa \equiv 2l(l+1) - 2C_0R_0. \tag{2.71}$$

2.6.4 Axisymmetric shapes

In order to investigate the evolution of the shapes which bifurcate from the sphere at the critical value $P_c(l)$, the fourth order partial differential equation (2.64) has to be solved numerically. In full generality, this task has not yet been attacked. A significant simplification arises if the search for stationary shapes is restricted to axisymmetric ones. This restriction is not as severe as it may look in the first place since it turns out that in large regions of the interesting parameter space the shape of lowest energy is indeed axisymmetric for vesicles of spherical topology.

For axisymmetric shapes, the shape equation becomes an ordinary differential equation of fourth order. It can be derived either by specializing the general shape equation (2.64) to axisymmetric contours, or by inserting a parametrization of an axisymmetric vesicle into the

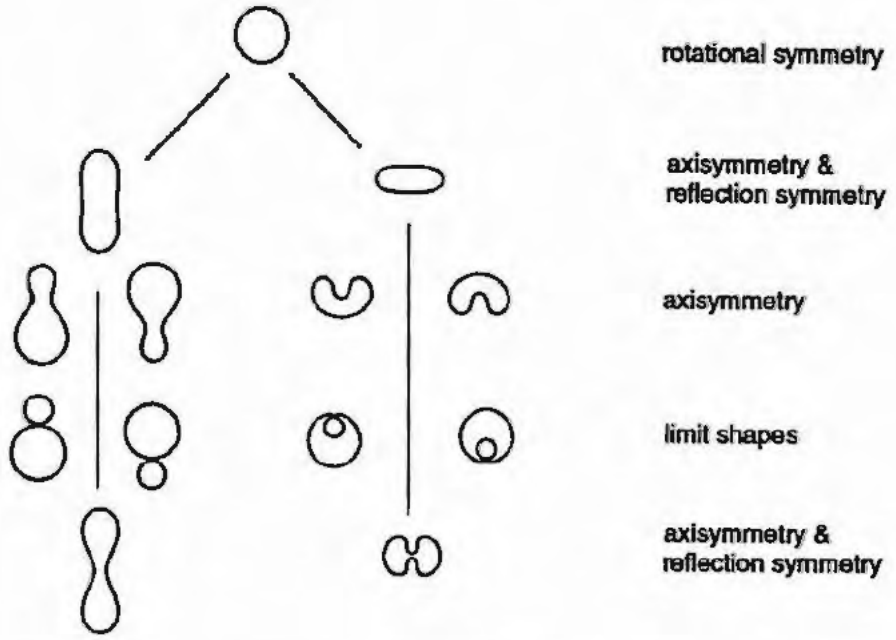

Figure 2.3: Bifurcation scheme with stationary shapes and their symmetry.

energy functional and then deriving the corresponding Euler Lagrange equations.[5] These shape equations can then be solved by a shooting method as explained in detail in (Seifert *et al.*, 1991b). In principle, a systematic procedure can be conceived that exhausts all solutions of the axisymmetric shape equations. Since its practical implementation, however, can become quite time-consuming, one rather needs a guided search for solutions. Such a guidance is provided by the bifurcations from the sphere, for which the parameters like P and Σ follow from the relations (2.68) and (2.71). These values can be used as good guesses for the shooting method.

For the $(l = 2)$−bifurcation, one thus finds prolate and oblate ellipsoids. Both types of shapes constitute a two-dimensional sheet emerging from the sphere which can be parametrized by the reduced volume v and the reduced mean curvature m. As one follows these shapes away from the sphere, the prolates become continuously more dumbbell-like while the oblates become biconcave. Along a one-dimensional curve in this sheet, sheets of shapes with broken up/down symmetry bifurcate from these up/down symmetric shapes. These are the pear

[5]Shape equations in various parametrizations have been derived and solved in (Helfrich, 1973; Deuling & Helfrich, 1976; Jenkins, 1977; Luke & Kaplan, 1979; Luke, 1982; Peterson, 1985b; Svetina & Zeks, 1989; Miao *et al.*, 1991; Seifert *et al.*, 1991b). Recently, there have been claims that the shape equations as derived in the cited works are incorrect (Hu & Ou-Yang, 1993; Naito & Okuda, 1993; Zheng & Liu, 1993). A rebuttal of these false claims is given in (Jülicher & Seifert, 1994) where it is pointed out that particular attention has to be given to the variation at the boundaries.

shapes and the stomatocytes, respectively, as shown in the scheme, Fig. 2.3 (Seifert *et al.*, 1991b).

While the oblates and prolates as well as the pears and the stomatocyte sheets have been studied quite exhaustively, little is known about other sheets which correspond to bifurcations from the sphere at larger values of l. However, there are also strong hints that these shapes are irrelevant, as discussed below in Sect. 3.2.2.

2.6.5 Limit shapes and neck condition

Sheets of shapes typically end in limit shapes where the contour becomes singular. The most prominent limit shape is those for the pears where the diameter of the neck has shrunk to zero. In this case, the shape consists of two spheres of radius R_A and R_B. It turns out that these radii have to fulfill the so-called "kissing" or "ideal neck" condition (Seifert, 1990; Berndl, 1990; Miao *et al.*, 1991; Seifert *et al.*, 1991b)

$$1/R_A + 1/R_B = C_0. \tag{2.72}$$

This condition was first found empirically. It can also be proven by a subtle matching procedure (Fourcade *et al.*, 1994). Despite its superficial simplicity, this condition has, however, withstood so far to any "simple" proof. A hint to where such a proof could start follows from the observation that the kissing condition implies that the curvature energy density $(2H - C_0)^2$ is the same in both adjacent segments. The ideal neck condition applies also to limit shapes for which one segment, say A, is a prolate. In this case, R_A denotes the curvature of this shape at the pole.

Other limit shapes include an infinitely thin cylinder (for the prolates), two spheres of equal size (also for the prolates), a spherical cavity embedded in a larger sphere (for the stomatocytes), as well as shapes which self-intersect along the axis (for the discocytes and the stomatocytes) (Seifert *et al.*, 1991b). In the latter case, the sheets can be extended mathematically beyond the lines of self-intersection. Physically, however, such a limit line shows that for those parameters, self-interaction of the membrane has to be taken into account.

Chapter 3

Shape transformations and phase diagrams

In this Chapter, we organize systematically the stationary shapes in so-called phase diagrams. These phase diagrams then provide the basis for a comparison between theoretical results and experimentally observed shape transformations.

The set of stationary shapes comprises both locally stable shapes and saddle points. In principle, one should analyse the local stability of each shape and then discard the locally unstable saddle points and proceed with the local minima. Such a comprehensive stability analysis has not yet been completed. However, stability with respect to axisymmetric deformations is easy to check by close inspection of the bifurcation diagram. We explain this method in Sect. 3.1, where we introduce the crucial concept of a continuous and a discontinuous transition.

These transitions separate different regions in a phase diagram, which shows the shape of lowest energy (and sometimes also locally stable shapes of higher energy) for a given set of controlled variables such as the reduced volume and the area difference. Since both the energy and the relevant parameters depend on the specific variant of the curvature model, the phase diagrams and the character of a shape transformation differ between the various variants as well.

Before we present the phase diagrams for the most important variants of the curvature model in Sects. 3.3 through 3.6, we address the issue of stability with respect to non-axisymmetric perturbations and the relevance of non-axisymmetric shapes in Sect. 3.2. We include information about stability in the phase diagrams wherever possible.

For a comparison of the theoretical results with experimental findings in Sect. 3.7, we introduce the notion of a temperature trajectories into the phase diagram. The budding transition will serve as an example to show how detailed a comparison is possible at the present stage.

3.1 Continuous and discontinuous transitions

Any bifurcation can occur as a continuous or a discontinuous transition (Seifert *et al.*, 1991b). In this section, we discuss the two variants paradigmatically for the prolate/pear bifurcation. The systematics and specific parameters for which each case applies will be given in Sect. 3.5 below.

In Fig. 3.1, the energy W within the ADE model of the (symmetric) prolates and the (asymmetric) pears is sketched for two different values of α as a function of the reduced area difference m_0 while the reduced volume v is kept constant (Miao *et al.*, 1994). Thus, the same one-parameter family of prolates and pears is involved in both cases because at constant v there is only a one-parameter family of prolates and pears, respectively. However, the topology of the energy close to the transition is qualitatively different. In the diagram on the left (typical for large α), which corresponds to a *continuous transition*, the symmetric shapes become unstable with increasing m_0 beyond the point marked with C^{pear}. In the diagram on the right hand side (typical for small α), the symmetric shape still become unstable with increasing m_0 beyond the point marked with M^{pro}. In the latter case, the asymmetric shapes close to the bifurcation, however, are also unstable since their energy constitutes the upper part of the "Gibbs' wing". This situation corresponds to a *discontinuous transition* since with increasing m_0 the symmetric shapes become metastable beyond D^{pear} and unstable beyond M^{pro}. With decreasing m_0, the asymmetric shapes become metastable below D^{pear} and become unstable below M^{pear}. In the regime between M^{pear} and M^{pro}, the asymmetric shapes of the upper part of the Gibbs' wing, in fact, correspond to the saddle points (and their energy to the activation energy) of this discontinuous transition. The asymmetric shapes close to the bifurcation thus change their stability as a function of α. For large α, they are stabilized by the area-difference-elasticity energy, while for small α they become unstable.

In such a qualitative discussion of the generic feature of the energy diagrams, notions borrowed from thermodynamics were used. Despite the appeal of such an analogy, it is important to keep in mind that there are fundamental differences between a thermodynamic phase transition and a shape transformation of a vesicle which, in fact, more resembles a *bifurcation*. A single vesicle does not form a thermodynamic system in which phases of the same energy could coexist. The vesicle is either symmetric or asymmetric but it is not half symmetric and half asymmetric. As quantitative energy diagrams show, the activation energy between two locally stable shapes is of the order of κ times a numerical prefactor. The shape transformation in the case of a discontinuous transition will set in as soon as the activation energy between the "metastable" and the globally stable shape

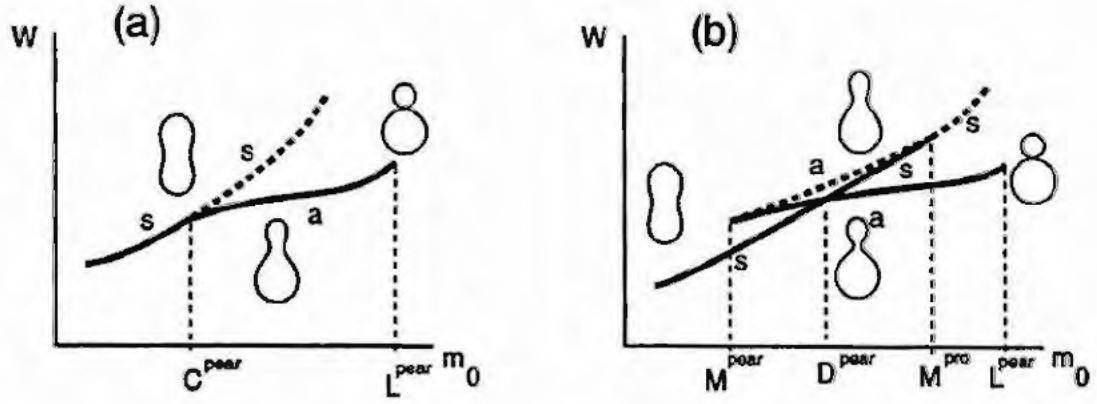

Figure 3.1: Continuous (a) and discontinuous (b) transition. Both figures show the energy W of the symmetric (s) and asymmetric (a) shapes as a function of the optimal reduced area difference m_0 at fixed reduced volume v for large α (a) and small α (b) . Typical shapes are sketched along the branches. The dashed curves show the energy of unstable shapes. In case (a), all asymmetric shapes are locally stable, the symmetric shapes are unstable to the right of C^{pear}. In case (b), the asymmetric shapes are unstable on top of the Gibbs' wing. M^{pear} and the bifurcation point M^{pro} denote the spinodals of the discontinuous transition. The asymmetric branch ends in the limit shape L^{pear}. After (Miao *et al.*, 1994).

becomes comparable to the thermal energy T. Depending on the specific transition, this point will be close to the limits of metastability as given by M^{pro} and M^{pear} for a "strong" discontinuous transition and may be closer to D^{pear} for a weak transition. In the latter case, one may even expect fluctuations of the shape across the weak barrier.

3.2 Stable shapes

Stability with respect to *axisymmetric* perturbations follows from a close inspection of the energy diagram in the vicinity of a bifurcation as discussed above. There are a few results and some other techniques relating to stability with respect to *non-axisymmetric* perturbations.

3.2.1 A theorem

In Sect. 4.1.2 below, we will prove a theorem which addresses the question of whether or not the stability of any specific shape depends on the variant of the curvature model, or, in particular, on the value of the material parameter α if we stay within the ADE model. It turns out that the stability of a shape with respect to a deformation which breaks a symmetry is a property of the shape and, thus, holds for any variant (or any value of α);

the stability of a shape with respect to a deformation which does not break a symmetry can depend on the variant under consideration.

This theorem implies that whenever an axisymmetric shape is unstable with respect to a non-axisymmetric deformation it will be unstable in any variant of the curvature model. Therefore, every result on stability with respect to non-axisymmetric deformations obtained in any variant of the curvature model carries over to all variants immediately. On the contrary, the α-dependent stability of the weak pears illustrates the second part of the theorem: These shapes are stable for large α but become saddle points for small α. This instability, however, does not break a symmetry.

3.2.2 Systematic stability analysis

In the next chapter, a scheme will be developed with which the stability of axisymmetric shapes can be analysed systematically. While a comprehensive analysis is not yet completed (Nikolic *et al.*, 1994), the yet available results will be integrated into the phase diagrams shown below.

3.2.3 Spherical limit

In the spherical limit, $v \to 1$, Peterson has proven that all shapes which result from the sphere by a bifurcation labeled with $l \geq 3$ (compare Sect 2.6.3) are unstable with respect to a $(l = 2)$–deformation (Peterson, 1989). According to this general result, only the $(l = 2)$–shapes are suitable candidates for local minima near the sphere. Even though Peterson used the spontaneous curvature model, his proof also holds for the other variants.

Focusing on the shapes resulting from the $(l = 2)$-bifurcation, the following result has been derived for the one parameter family of stationary shapes parametrized by m by expanding the curvature energy as well as the constraints for fixed $v < 1$ with $1-v \ll 1$ (Milner & Safran, 1987; Heinrich *et al.*, 1992): Shapes with the largest m are axisymmetric prolates. With decreasing m, these shapes become unstable with respect to a non-axisymmetric deformation which leads to ellipsoids. For even smaller m, these shapes become the axisymmetric oblates.

3.2.4 Variational approaches

In an approach based on a variational ansatz, (Heinrich *et al.*, 1993) parametrized shapes by spherical harmonics. While certain amplitudes are fixed by the constraints, a minimization with respect to the free amplitudes in a subspace $l \leq l_{max}$, which includes non-axisymmetric

shapes, leads to an approximation of locally stable shapes. The results obtained by this technique will be integrated into the next sections.

3.2.5 Direct minimization

In a recent development, a discretized version of the bending energy has been minimized by a steepest descent method on a triangulated surface (Schnitzler, 1993). The numerical effort for such an algorithm to work is considerable, but a few new results have been obtained so far, in particular for the vesicles of non-spherical topology discussed in Chapter 5. An advantage of this method is that one can start with an axisymmetric stationary shape obtained by solving the shape equations and then apply a small non-axisymmetric perturbation. If the shape under the minimizing algorithm restores the axisymmetry, this provides evidence that the shape is indeed a local minimum.

3.3 A simple model: Local curvature energy only

The simplest model for vesicles consisting of symmetric bilayers is given by the local curvature energy G (2.51) and the constraints on area and volume. Because of the scale invariance of the curvature energy, this model depends only on one parameter, the reduced volume v defined in Eq. (2.67).

The axisymmetric stationary shapes in this model, which can be found by solving the shape equations (Seifert *et al.*, 1991b), comprise both the oblate ellipsoids (which become biconcave discocytes as the reduced volume is decreased) and the prolate ellipsoids (which acquire a long cylindrical shape as the reduced volume decreases.) A third class of stationary shapes are the stomatocytes which bifurcate from the oblates through a transition which breaks the reflection symmetry. Both the energy of these branches and typical shapes are shown in Fig. 3.2.

Perturbation theory in the spherical limit (Milner & Safran, 1987; Heinrich *et al.*, 1992) shows (i) that the oblates which show up as stationary shapes in the energy diagram, in fact, are unstable and (ii) that there are no stationary (let alone stable) non-axisymmetric ellipsoids in this limit. A systematic stability analysis shows that the oblates become locally stable for $v < v_C^{ob} \simeq 0.75$ (Nikolic *et al.*, 1994). The same approach also indicates that the prolates remain locally stable for all v.

Collecting these results, the (one dimensional) phase diagram contains the following sequence of absolute minimal shapes with decreasing v as shown in Fig. 3.2: Prolates for $v > v_D \simeq 0.65$, oblates for $v_D^{sto} < v < v_D$, with $v_D^{sto} \simeq 0.59$ and finally stomato-

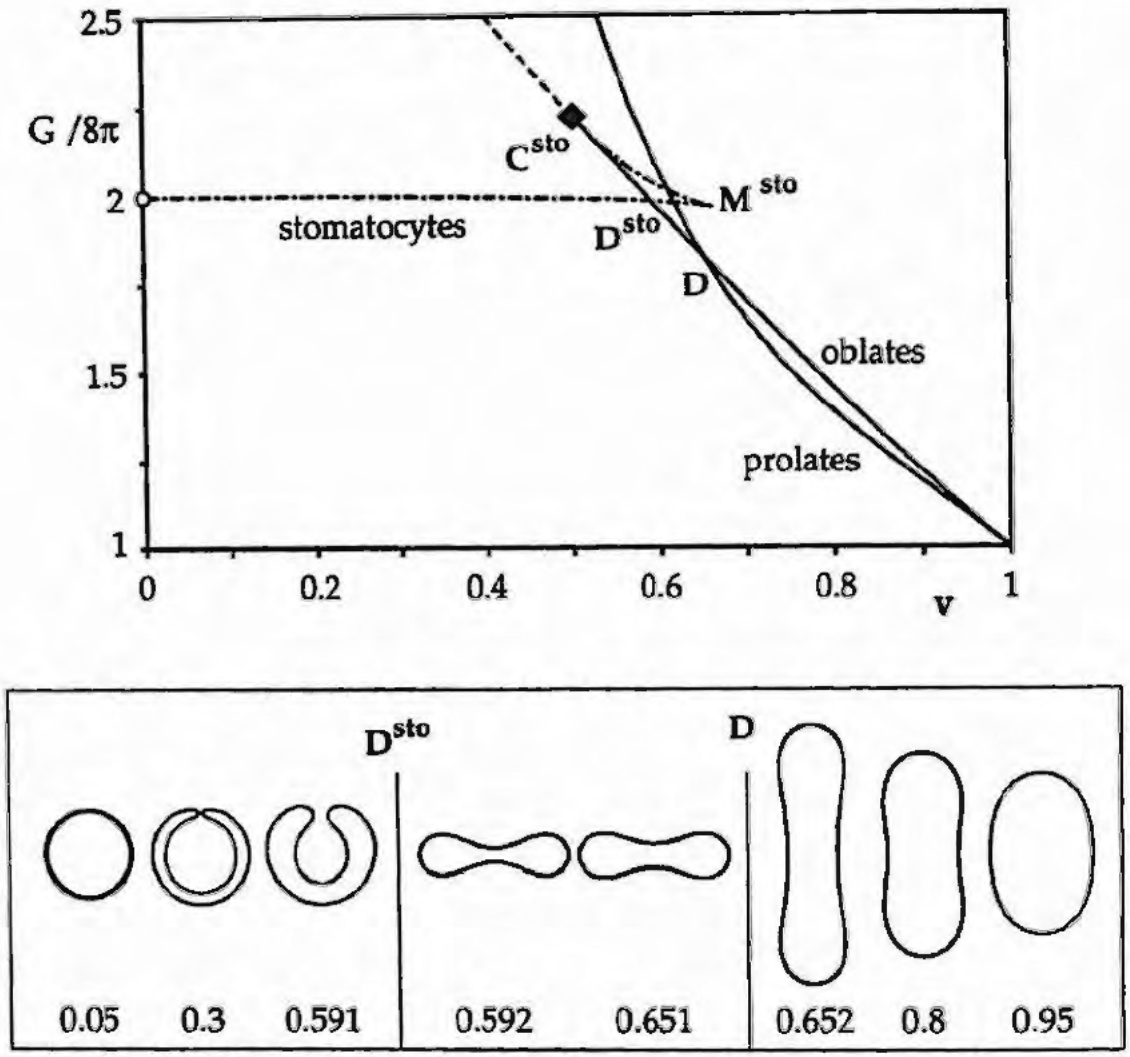

Figure 3.2: Energy G and contours of stationary shapes as a function of reduced volume v. All shapes have the same area. D and D^{sto} denote the discontinuous prolate/oblate and oblate/stomatocyte transition. The oblates and the stomatocytes loose metastability at C^{sto} and M^{sto}, respectively. Beyond the diamond, the oblates self-intersect. (Seifert *et al.*, 1991b)

cytes for $v < v_D^{sto}$. The discontinuous prolate/oblate transition has a spinodal for the oblates at v_C^{ob}, whereas the prolates are (at least) metastable for all v. The discontinuous oblate/stomatocyte transition has spinodals at $v_M^{sto} \simeq 0.66$ for the stomatocyte and $v_C^{sto} \simeq 0.51$ for the oblate, respectively (Seifert *et al.*, 1991b).

Three facts about this simple model should be emphasized: (i) The biconcave discocytes have the lowest energy in a narrow range of reduced volume v. Thus, neither a negative

spontaneous curvature nor any specific bilayer feature is necessary to obtain red-blood-cell-like shapes, contrary to repeated claims in the older literature. (ii) Budding does not occur in this model since pears do not show up as stationary shapes in this variant. (iii) So far, there is no indication for the presence of locally (let alone globally) stable non-axisymmetric shapes in this model for any v.

3.4 Bilayer–couple model

In this variant, a second constraint is imposed on the reduced mean curvature m which gives rise to a two-dimensional phase diagram. A fourth class of axisymmetric shapes, the pears, as well as non-axisymmetric ellipsoids now become relevant (Svetina & Zeks, 1989; Seifert *et al.*, 1991b).

The axisymmetric shapes show up in two separate regions of the phase diagram shown in Fig. 3.3. The prolates and the pears occur for larger values of m, the oblate shapes and the stomatocytes for smaller values of m. In both cases, the reflection symmetry is broken continuously at C^{sto} and C^{pear} , respectively. The pears and the stomatocytes are both bounded by a limit line. For the pears, this limit line L^{pear} is the vesiculation line where the neck diameter connecting the two spherical compartments has shrunk to zero. The location of this line follows straight from geometry as (Svetina & Zeks, 1989; Seifert *et al.*, 1991b)

$$v_L^{pear}(m) = 1 - 3[m/(4\pi) - 1]^2/2 - [m/(4\pi) - 1]^3/2 \tag{3.1}$$

with $1 \leq m/(4\pi) \leq \sqrt{2}$. This limit line starts at the point E where two spheres with equal radius sit on top of each other and ends in the point S of a sphere. The same two points are also connected by the line C^{pear} of continuous transitions between the prolates and the pears.

The stomatocytes are likewise bound by a limit line of shapes L^{sto} which consist of a sphere that encloses a smaller sphere. Both spheres are connected by an ideal neck. The locus L^{sto} is also given by (3.1) with $0 < m/(4\pi) < 1$.

The gap between the prolates and the oblates has been conjectured as filled with non-axisymmetric ellipsoids, which are separated by two continuous transitions C^{ob} and C^{pro} from the axisymmetric shapes (Seifert *et al.*, 1991b). This prediction has since then been verified by the variational approach (Heinrich *et al.*, 1993).

Significant parts of the phase diagram have not been yet explored. There are three reasons for our lack of knowledge about shapes of lowest energy in these regions. First, there is a region above the oblates and to the left of $v \simeq 0.7$ where both shapes with only two reflection planes and shapes with a threefold axis become relevant, as preliminary numerical work by

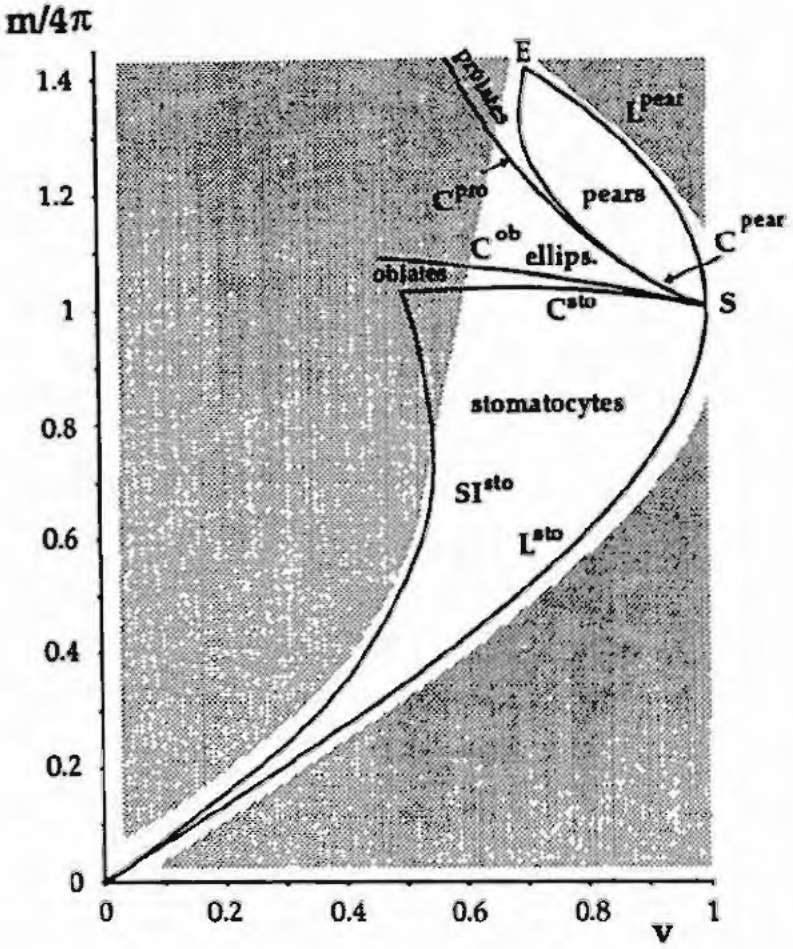

Figure 3.3: Phase diagram of the bilayer coupling model. This phase diagram shows the state of lowest energy as function of the reduced area difference m and of the reduced volume v. C^{pear} denotes the line of continuous transitions between up-down symmetric prolate/dumbbell shapes and up-down asymmetric pear-shapes. Likewise, C^{sto} denotes the locus of the continuous transitions between the oblate/discocyte shapes and the stomatocytes. L^{pear} and L^{sto} are limit curves which correspond to budding and the inclusion of a spherical cavity, respectively. S corresponds to a sphere. In the region between the prolate/dumbbell and discocyte regime, non-axisymmetric ellipsoids have lowest energy. This region is separated by continuous transitions C^{pro} and C^{ob} from the corresponding axisymmetric shapes. E denotes the point where two spheres of equal radii are sitting on top of each other. Along the line SI^{sto}, the two poles of the shape touch each other. In the shaded areas, the shape of lowest energy has not been determined so far. After (Seifert *et al.*, 1991b).

a direct minimization indicates (Schnitzler, 1993). Secondly, above the limit line L^{pear} and below L^{sto} , two types of shapes can occur which have not yet been investigated in detail either. One would expect that either the necks remain ideal and one of the spheres becomes a prolate or that shapes which involve three compartments with finite necks occur. From a more physical perspective one could consider how the membrane–membrane interaction such as van der Waals interaction in the region of the necks becomes a relevant parameter for a faithful description of the physics in this region (Käs *et al.*, 1993). The same remark applies to a third region which is to the left to the line SI^{sto} where the membrane self-intersects. Again, further energy terms should be invoked here. One could either apply just self-avoidance of the membrane, or one could allow for self adhesion, in which case at least one more parameter such as the adhesion energy becomes relevant.

3.5 Area–difference–elasticity model

In this variant, the constraint on the total mean curvature m is relaxed and becomes an elastic energy which arises physically from the relative compression and expansion of the two monolayers as derived in Sect. 2.4. In dimensionless units, the energy W as defined in Eq. (2.50) is given by

$$W(\alpha, v, m_0) = \kappa[G(v, m) + \alpha(m - m_0)^2/2], \tag{3.2}$$

where the scaled optimal area difference m_0 has been introduced in Eq. (2.56). Since the ADE model contains the three parameters v, m_0 and α, its phase diagram is more complex than that of the BC model even though no new shapes occur, due to the fact that the manifold of all shapes is only (degenerate) two-dimensional. A comprehensive exploration of the three-dimensional phase diagram has not yet been achieved. Two fairly detailed studies focused on the budding regime (Seifert *et al.*, 1991a; Miao *et al.*, 1994) and the prolate–oblate transition (Heinrich *et al.*, 1993), respectively.

3.5.1 Phase diagram for $v = 0.85$

In Fig. 3.4, we present the phase diagram at a paradigmatic fixed reduced volume $v = 0.85$, as it can be obtained by collecting the data from (Miao *et al.*, 1994) and (Heinrich *et al.*, 1993). Conjectured properties of the oblate/stomatocyte transition are also included.

As a recurrent theme in the ADE model, transitions which are continuous in the BC model ($\alpha = \infty$) become discontinuous at a tricritical point with decreasing α through a mechanism explained below. This phenomenon applies to the budding transition, as well as to the

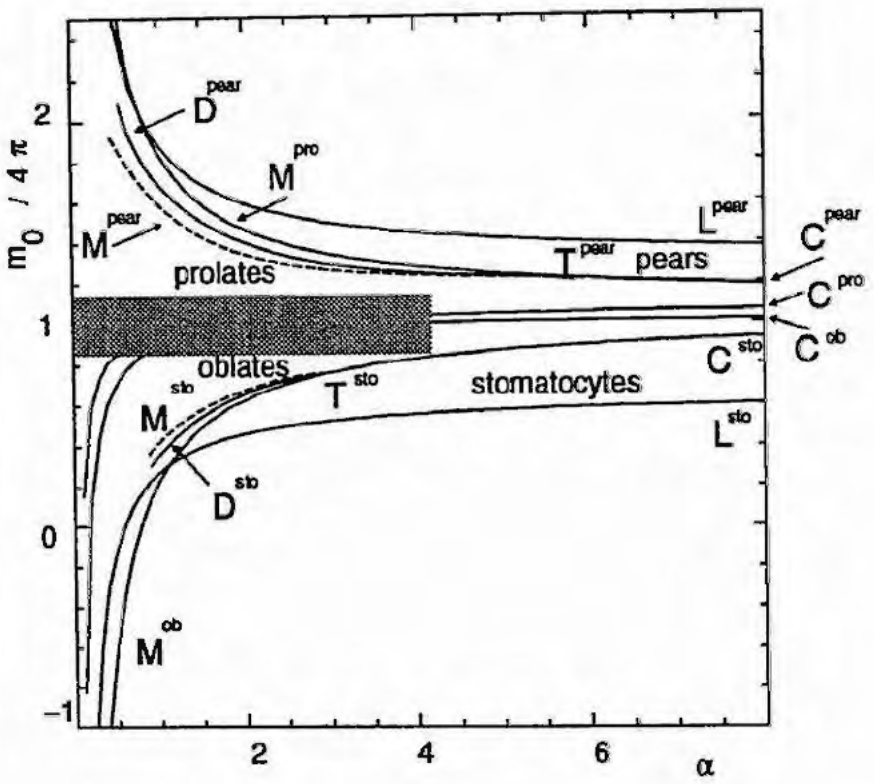

Figure 3.4: Phase diagram of the ADE model at fixed reduced volume $v = 0.85$ as a function of the optimal area difference m_0 and the rigidity ratio α. The curves C^{pro} and C^{ob} denote continuous transition to non-axisymmetric ellipsoids from prolates and oblates, respectively. D denotes the discontinuous prolate/oblate transition. T^{pear} and T^{sto} denote tricritical points. The other notation is as in Fig. 3.3. Above the limit lines L^{pear} and L^{sto}, the shape of lowest energy has not been determined so far. The location of the curves M^{pear}, M^{sto}, D^{pear}, and D^{sto} is only conjectured. The shaded region, which contains the prolate/oblate transition, is shown in detail in Fig. 3.5.

oblate–ellipsoid–prolate transition. The latter case is somewhat more complicated since the two separated continuous transitions finally become one discontinuous transition. First, the continuous transition between the ellipsoids and the prolates becomes discontinuous, and then these ellipsoids vanish as globally (and later as even locally) stable shapes. The transition then proceeds as a discontinuous transition from the oblates to the prolates with ellipsoids as saddle points in-between.

The important characteristics of the phase diagram shown in Fig. 3.4 can be summarized as follows. (i) The region where the prolates are locally stable widens with decreasing α.

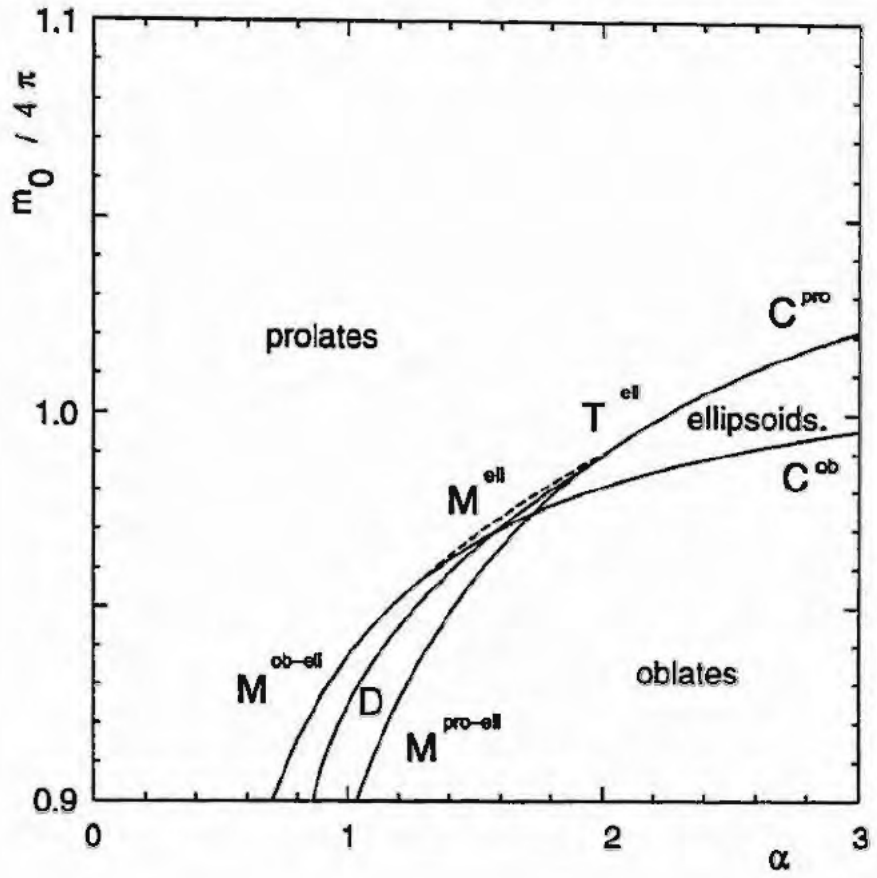

Figure 3.5: Detail from Fig. 3.4. T^{ell} is the tricritical point for the prolate/ellipsoid transition. M^{ell}, $M^{pro-ell}$, and M^{ob-ell} denote limits of metastability of the non-axisymmetric ellipsoids, the prolates and the oblates, respectively. The other notation is as in Fig. 3.4.

(ii) The continuous transition from the prolates to the pears becomes discontinuous below the tricritical point. For even smaller α, the prolates lose metastability beyond the limit line L^{pear}, which means that once budding takes place, it will lead to a vesiculated shape with infinitesimal neck. (iii) The non-axisymmetric ellipsoids vanish as ground state shapes for $\alpha \lesssim 1.7$. For $\alpha \lesssim 1.3$, there are not even any more locally stable ellipsoids. (iv) As $\alpha \to 0$, only one particular shape survives, which is the shape of minimal local curvature energy G discussed in Sect. 3.3 , which, for $v = 0.85$, is a prolate. (v) The oblate-stomatocyte transition has not yet been analysed in detail, but one would expect the same scenario as for the budding transition.

While the topology of this two-dimensional section persists for all values of $v \gtrsim 0.72$, the precise location of all transitions and limit shapes become functions of the reduced volume

v. For $v \lesssim 0.72$, the phase diagram is unknown in the budding region for the same reasons as discussed for the BC model. Disregarding this part of the phase diagram, it is clear that for $0.59 \lesssim v \lesssim 0.65$, the region of the oblates widens with decreasing α, whereas for $v \lesssim 0.59$ the stomatocytes spread.

As an important aside, we recall as a consequence from Sect. 2.5, that the phase diagram just discussed also holds in the presence of a non-zero spontaneous curvature c_0 provided m_0 is replaced by $m_0 + 2c_0/\alpha$.

3.5.2 Derivation

The derivation of the phase diagram as shown in Fig. 3.4 is based on the equivalence of the ensembles discussed in Sect. 2.6.1, which leads to a mapping of the energy diagrams from the BC model to the ADE model (Seifert *et al.*, 1991a; Miao *et al.*, 1994). The reader not interested in this more technical aspect should skip this section.

As the correspondence between the variants of the curvature model implicit in Eqs. (2.59) and (2.61) shows, any particular shape with v and m is a stationary shape for all parameter sets which obey the relation

$$m_0^{(n)} = m^{(n)} + (\partial G/\partial m)/\alpha. \tag{3.3}$$

Here, and in the following, the derivative of the bending energy $G(m)^{(n)}$ is taken at fixed v along a branch of stationary shapes labeled with $^{(n)}$. For each stationary shape, Eq. (3.3) establishes a one-to-one mapping from $(m^{(n)}, v)$ in the BC model to $(m_0^{(n)}, v)$ in the ADE model.

The relation (3.3) can also be derived directly by first varying the energy W (3.2) with respect to the shape at fixed m and v. This leads to the stationary shapes of the BC model, since the last term of (3.2) is constant under these conditions. This proves that every stationary shape of the ADE model is also a stationary shape of the BC model which has been shown more generally in Sect. 2.6.1. Finally, varying the energy W with respect to m leads to Eq. (3.3).

This mapping is very useful for the determination of the phase diagram in the ADE model from that of the BC-model since it allows to map, in particular, the location of symmetry breaking bifurcations such as C^{pear}, C^{pro}, C^{ob} and C^{sto} as well as the location of the limit lines L^{pear} and L^{sto} to any finite α section. One just needs to know $m(v)$ and $(\partial G/\partial m) = 2c_0(v)$ of these shapes.

For the limit lines L^{pear} and L^{sto}, the mapping can be performed analytically since $m(v)$ and $c_0(v)$ of these shapes are known form Eq. (3.1) and the ideal neck condition (2.72) if

the latter is written in dimensionless variables. One thus obtains

$$m_{0,L}(v) = m(v) + (m(v)/\alpha\pi)/[(m(v)/4\pi)^2 - 1]. \tag{3.4}$$

The determination of the phase diagram in the ADE model from that of the BC model, however, is non-trivial since the mapping (3.3) can become non-monotonic as a function of m. Indeed, differentiating (3.3) with respect to m leads to the relation,

$$\partial m_0^{(n)}/\partial m = 1 + \left(\partial^2 G^{(n)}/\partial m^2{}_{|v}\right)/\alpha, \tag{3.5}$$

which shows that with increasing α, the mapping (3.3) becomes non-monotonic whenever $\partial^2 G^{(n)}/\partial m^2 \equiv G^{(n)''}(v)$ is negative somewhere along a branch. For an illustration of this phenomenon, which ultimately changes the character of a bifurcation from continuous to discontinuous, we will consider the prolate-pear bifurcation where this mechanism has been studied in detail.

Based on numerically established properties of the second derivatives of the bending energy $G^{(n)}(v,m)$ of the BC model in the interval $0.72 < v < 1$, it is shown in (Miao *et al.*, 1994) that $\partial m_0^{(s)}/\partial m$ is positive everywhere on the symmetric branch, while on the asymmetric branch $\partial m_0^{(a)}/\partial m$ changes sign at the point $\alpha = \alpha_T(v)$, where $\alpha_T = -G^{(a)''}(v, m_C(v))$ and $m_C(v)$ denotes the area difference of the asymmetric shape at the bifurcation point.

These properties imply two different scenarios for the prolate/pear bifurcation in the ADE model, corresponding to the continuous and discontinuous transitions, C^{pear} and D^{pear}, respectively.

(i) For $\alpha > \alpha_T(v)$, the mapping (3.3) is monotonic for both the symmetric and asymmetric branches, and the topology of the energy diagram of the BC model is well preserved, as illustrated in Fig. 3.1a, so the symmetry-breaking transition is continuous. The corresponding phase boundary C^{pear} is given by

$$m_{0,C} = m_C + G^{(s,a)'}(v, m_C)/\alpha. \tag{3.6}$$

(ii) When $\alpha < \alpha_T(v)$, the mapping (3.3) becomes non-monotonic for the asymmetric branch, while it remains monotonic for the symmetric branch. As a consequence, a "wing" structure in the energy diagram, as shown in Fig.2b appears. The position of the cusp on the left side of the wing is determined by $G^{(a)''}(v,m) = -\alpha$. This relation determines the spinodal, M^{pear} , for the pears. The corresponding discontinuous budding transition occurs at D^{pear}, the precise location of which must be computed numerically.

The tricritical point T^{pear} at which C^{pear} and D^{pear} meet has coordinates $(\alpha_T(v), m_{0,T}(\alpha))$, where α_T satisfies the condition, $\alpha_T = -G^{(a)''}(v_T, m_C)$, and $m_{0,T}$ is given through the mapping (3.3).

A similar scenario has been found for the continuous oblate–ellipsoid– prolate transitions. With decreasing α, these transitions also become discontinuous. One would also expect that the same happens for the continuous oblate–stomatocyte transition for which the tricritical point has not yet been located.

3.6 Spontaneous curvature model

The phase diagram for the spontaneous curvature model depends on the two parameters v and the scaled spontaneous curvature c_0 as defined in Eq. (2.56). This phase diagram is shown in Fig. 3.6, as obtained by an analysis of the appropriate energy diagrams of the stationary shapes (Seifert *et al.*, 1991b). So far, there is no evidence that non-axisymmetric shapes could be relevant anywhere in the phase diagram.

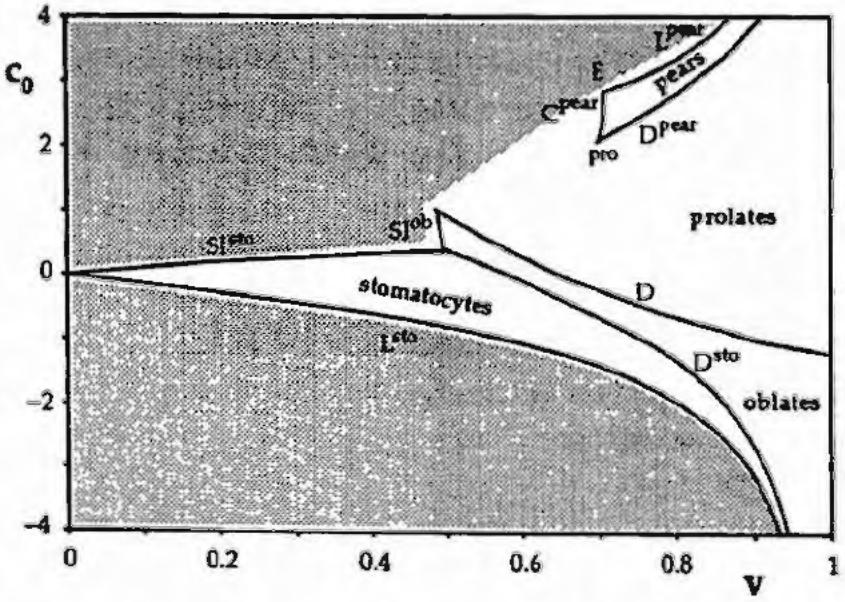

Figure 3.6: Phase diagram of the spontaneous curvature model. This phase diagram shows the shape of lowest bending energy as a function of the scaled spontaneous curvature c_0 and of the reduced volume v. The regions where the prolate/dumbbell, pear-shaped, oblate/discocyte and stomatocytes have lowest energy are separated by transition lines. The line C^{pear} denotes a continuous transition. All other transitions are discontinuous. At E, two spheres of equal size sit on top of each other. The lines L^{sto} and L^{pear} correspond to limit shapes with infinitesimal neck. Beyond the lines SI^{ob} and SI^{sto} self-intersecting states occur. In the shaded area, the shape of lowest energy has still to be determined. After (Seifert *et al.*, 1991b).

In the region of moderate c_0, the phase diagram is dominated by four large regions of axisymmetric shapes. For positive c_0, these are the pears which are separated by a strong first order transition from the prolates. With decreasing c_0, the prolates become oblates via another first order transition, which becomes weak in the spherical limit where it hits at $c_0 = -1.2$ the sphere. For negative c_0, the oblates undergo another strong first–order transition to the stomatocytes. In fact, all but one transition found so far are discontinuous in this model.

There are significant parts of the phase diagram where either self-interaction of the membrane has to be taken into account, or where even the analysis of the axisymmetric stationary shapes is still incomplete, which is particularly true in the vicinity of the point E where two spheres of equal size sit on top of each other. This shape does not cost energy in this model. For large positive c_0, a whole sequence of multiple vesiculated shapes appear since the energy now prefers spheres of radius $2/C_0$. This region has been investigated thoroughly in (Miao *et al.*, 1991; Miao, 1992).

3.7 Comparison to experiment

As far as the theory is concerned, the phase diagrams contain all the relevant information of each variant of the curvature model. The question then is whether one can decide in favor of a particular variant or, formulated within the ADE model, whether one can obtain a value of α on the basis experiments such as those discussed in Chapter 1. Since in these experiments temperature is changed, the temperature dependence of the parameters which determine the phase diagram has to be discussed first.

3.7.1 Temperature trajectories

An increase in temperature from an initial value T_0 leads to thermal expansion of the area of the two monolayers. It will be necessary to admit a small asymmetry γ of the expansion coefficients of the two monolayers (Berndl *et al.*, 1990; Seifert *et al.*, 1991b), β^{in} and β^{ex}, defined as

$$\beta^{in} \equiv \frac{1}{A^{in}} \frac{\partial A^{in}}{\partial T} \equiv \beta \quad \text{and} \quad \beta^{ex} \equiv \frac{1}{A^{ex}} \frac{\partial A^{ex}}{\partial T} \equiv (1+\gamma)\beta. \tag{3.7}$$

A typical value is $\beta \simeq 6 \times 10^{-3}/K$ (Evans & Needham, 1987), which is one order of magnitude larger than the expansion coefficient for the enclosed aqueous solution. The latter can therefore be neglected. However, one has to take into account that the thickness $2d$ of the

bilayer also becomes temperature dependent according to

$$\frac{1}{d}\frac{\partial d}{\partial T} \equiv \beta_d. \tag{3.8}$$

Assuming, for simplicity, temperature independent expansion coefficients, one finds for a temperature trajectory the expression

$$m_0 = \left(\frac{v(T_0)}{v}\right)^r \left(m_0(T_0) + b\left(\left(\frac{v(T_0)}{v}\right)^{\gamma q} - 1\right)\right), \tag{3.9}$$

parametrized by an initial point with $m_0 = m_0(T_0)$ and $v = v(T_0)$ on the trajectory (Berndl *et al.*, 1990; Seifert *et al.*, 1991b). The exponents are given by

$$q = (2+\gamma)/3, \tag{3.10}$$

and

$$r = \frac{2-\gamma-4\beta_d/\beta}{3(2+\gamma)}. \tag{3.11}$$

The latter value can be bounded theoretically by two limiting cases. (i) If the monolayer separation $2d$ does not change with temperature, one has $\beta_d = 0$ which leads to $r = 1/3$. (ii) If d decreases with temperature in such a way that the bilayer volume as given by $\sim Ad$ remains temperature independent, i.e. $\beta_d = -\beta$, one has $r = 1$. Experiments using nuclear magnetic resonance indicate that the latter case is a good approximation (Nezil & Bloom, 1992). Without asymmetry, i.e. for $\gamma = 0$, one obtains the simple expression

$$m_0(v) = m_0(T_0)\left(\frac{v(T_0)}{v}\right)^r. \tag{3.12}$$

The dimensionless coefficient b in (3.9), which determines the effect of an asymmetric expansion, is given by

$$b \equiv \frac{A^{ex}(T_0)}{d(T_0)[(A^{in}(T_0)/(4\pi)]]^{1/2}} \simeq 2\sqrt{\pi}\frac{R_0(T_0)}{d(T_0)}. \tag{3.13}$$

For giant vesicles, this coefficient is of order of $10^3 - 10^4$, which indicates that even a tiny asymmetry of the order of 10^{-3} has an enormous influence on a temperature trajectory as demonstrated first within the BC model (Berndl *et al.*, 1990). The physical basis for this surprising effect is the length-scale separation alluded to in Chapter 2. The relevant scale for changes in the optimal area difference is dR_0, whereas the scale for the absolute change in area is R_0^2. Thus, small differences in the thermal expansion of the two layers get "magnified" by a factor R_0/d. As a consequence, if the outer monolayer expands more than the inner one,

the additional area accumulated in this outer layer will cause budding since the formation of buds increases the area difference. Likewise a stronger increase of the area of the inner monolayer induces a transition to the discocytes and the stomatocytes.

This sensitive dependence of the thermal trajectory in the phase diagram indicates that it will be rather difficult in general to reproduce experiments on vesicle shape transformations. Presently, the available purity of the lipids does not exclude the presence of residual impurities which could result in an asymmetric expansion of the order of 10^{-3}. It would be highly beneficial to investigate this effect systematically by deliberately adding traces of a second (miscible) component to one of the monolayers. However, one then has to be aware of additional effects arising from the mixture as discussed in Chapter 8.

For a complete prediction of the temperature trajectory, the initial value $(m_0(T_0), v(T_0))$ has to be known. For axisymmetric vesicles, the volume as any other geometrical quantity such as the total mean curvature can be inferred, in principle, from the mean contour of the vesicle, if the orientation of the symmetry axis is known. However, thermal fluctuations as well as rotational diffusion of the vesicle limit the resolution. The reduced volume thus has been obtained within one percent accuracy while the total mean curvature m involves higher derivatives of the contour and therefore is prone to larger errors. In fact, no measurement of m has been published yet.

The optimal area difference m_0 is not accessible to any non-invasive direct measurement yet. According to the present understanding, this quantity depends on the number of molecules in the two monolayers as the vesicle is formed. If one assumes that the vesicles are relaxed with respect to the non-local bending energy right after they have been formed, i.e., $m = m_0 > 0$, the dimensionless equilibrium area difference m_0 would depend on the specific shape the vesicle acquired after closure. The difference between, e.g., a sphere and a capped cylinder leads to a difference of $O(1)$ in m_0 (Miao, 1992), which then leads to different temperature trajectories even if the thermal expansion is symmetric. Recently, the optimal area difference m_0 has been measured for vesicles aspirated in micropipets from which thin tethers are extruded (Yeung, 1994). The result shows a broad distribution of values around $m_0 = 0$ which would indicate that the area difference does not adjust to the shape in the moment of closure. Whether such a distribution of m_0 is specific to the set up of that experiment or whether it holds generally remains to be seen.

3.7.2 Budding transition

Given the uncertainties in the thermal asymmetry and the value of the initial area difference m_0, it is reasonable to focus first on those qualitative aspects which can be treated even

without detailed knowledge of the precise temperature trajectory. As an example for such an approach, consider the phase diagram of the budding region in the area-difference elasticity model shown in Fig. 3.7 . This is a section of the three-dimensional phase diagram in the region where budding occurs at a fixed value of $\alpha = 4$, chosen here for illustrative purposes (Miao *et al.*, 1994). Two different cases for the budding transition can be distinguished: (i) For a relatively small reduced volume v, the symmetry-breaking budding transition between the prolates and the pear-shaped vesicles is continuous. Weak pears are therefore stable and an increase in m_0 will progressively decrease the neck diameter until at L^{pear} the vesiculation line is reached. (ii) For a large reduced volume, the budding transition becomes discontinuous, with the line of instability extending well into the vesiculated region beyond the limiting line L^{pear}. Therefore, the theory for this value of α predicts a qualitative difference between budding at a small reduced volume and budding at a larger reduced volume.

If we ignore the thermal asymmetry for a moment, the two qualitatively different cases can be related to different values of the initial optimal area difference $m_0(v = 1)$ of the initial spherical shape. Two temperature trajectories for symmetric expansion ($\gamma = 0$) are displayed in Fig. 3.7. The theory predicts that for continuous budding to happen, a relatively large temperature increase is necessary (since budding takes place at small v), which will then lead to a limit shape with two rather equally sized spherical compartments. On the other hand, the larger is the initial difference in number of lipid molecules between the two layers, the smaller is the temperature interval necessary to reach discontinuous budding, and the smaller is the size of the final bud. In particular, for sufficiently large $m_0(v = 1)$, the prolate shape in the latter case becomes unstable beyond the vesiculation line L^{pear}, which means that once budding takes place the new equilibrium shape is vesiculated and there will be no stable pears with finite necks.

This scenario does depend on the material parameter α for which at present the best estimate is $\alpha \simeq 1$, which is supported by derivations using standard elasticity theory as sketched in Sect. 2.4, as well as by experimental measurements (Waugh *et al.*, 1992; Yeung, 1994). For such a value, the tricritical point T^{pear} displayed in Fig. 3.7, has disappeared into the practically unaccessible region at $v \lesssim 0.72$. Budding is then predicted to be discontinuous for all v. These statements also hold in the presence of an asymmetric expansion provided the trajectory hits the budding transition D^{pear}.

The clear theoretical prediction of discontinuous budding for uni-lamellar vesicles ($\alpha \simeq 1$) is still in partial conflict with some experiments. Experimentally, two apparently different scenarios for the budding transition have been reported: (i) For DMPC- vesicles, a slow increase in temperature leads continuously from a prolate to a pear with weak up–down asymmetry which upon further temperature change jumps to a vesiculated shape with a

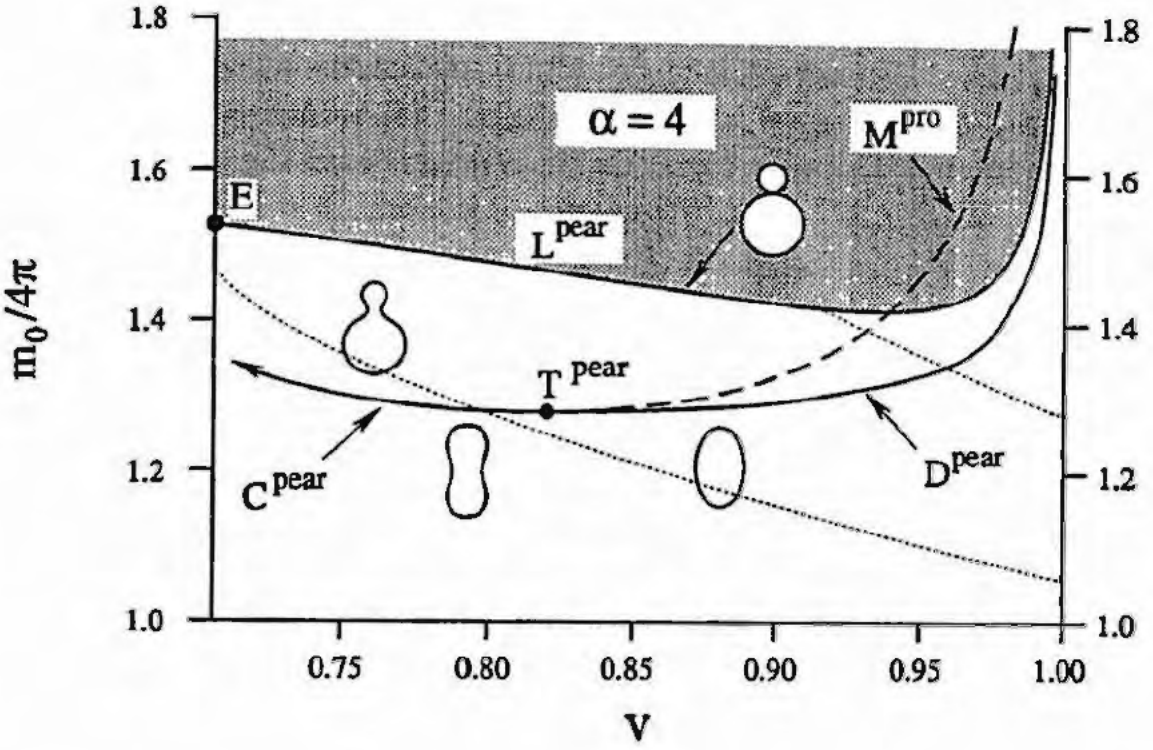

Figure 3.7: Phase diagram of the area-difference elasticity model in the budding region for rigidity ratio $\bar{\kappa}/\kappa = \alpha = 4$ as a function of the equilibrium area difference Δa_0 and of the reduced volume v. The lines C^{pear} and D^{pear} denote a continuous and a discontinuous budding transition, respectively, separated by the tricritical point T^{pear}. For a discontinuous transition, the prolates become infinitesimally unstable at the line M^{pro}. L^{pear} is the vesiculation curve where two spheres of different radii are connected by an ideal neck. At E, the two spheres have equal size. The dotted lines show two temperature trajectories (3.12) for symmetric thermal expansion. (Miao *et al.*, 1994).

narrow neck (Käs & Sackmann, 1991). (ii) For SOPC- vesicles in sucrose/glucose solutions, discontinuous budding is observed without the pear-shaped intermediates (Döbereiner, n.d.). A similar sequence can also be obtained for DMPC-vesicles provided they are kept under some tension before the heating starts (Käs & Sackmann, 1991).

The second experimental scenario is compatible with the predictions of a discontinuous budding of the area-difference elasticity model for $\alpha \simeq 1$. To explain experimental scenario (i) within the area-difference elasticity model is impossible. The apparent continuous transition from the symmetric shape could be reconciled by postulating a larger value of α, which is,

e.g., expected to apply for multi-lamellar vesicles (Svetina & Zeks, 1992). However, the apparent transition from a wide neck to a narrow neck is not even contained in any of the curvature models discussed so far. Further energy terms of the type $q(m - m_0)^3$ could, in principle, provide such a scenario (Kās *et al.*, 1993) but only with the ad-hoc assumption of an amplitude q of the order of 10^2. However, one expects any corrections to the area-difference-elasticity (2.50) arising from elastic interactions to be of the order of $d/R_0 \simeq 10^{-3}$. This magnitude is not sufficient to cause a discontinuous transition between two different neck sizes.

Two alternative explanations for the discrepancy could be that either the pears with weak up–down asymmetry correspond to long-lived dynamical fluctuations around a metastable shape (Miao *et al.*, 1994), or that an external inhomogeneity breaks the symmetry. First, one indeed expects long relaxation times near an instability since the time-scale $t_f \equiv \eta R_0^3/\kappa$ for long-wave length bending fluctuations (Brochard & Lennon, 1975; Milner & Safran, 1987) acquires an additional factor $1/(v_c - v)$ near an instability at $v = v_c$ (Miao *et al.*, 1994). Thus, the time-scale for a shape fluctuation towards the unstable mode t_f then formally diverges due to "critical slowing-down". In practice, this divergence will be cut-off by the decay of the metastable shape as soon as the energy barrier becomes comparable to the thermal energy T. In such a scenario, the "stable" pears would be long-lived fluctuations around a still metastable symmetric shape. Secondly, close to the transition, the symmetric shape is sensitive to any asymmetry which could arise from residual inhomogeneities of either the membrane or the measuring chamber. In this case, the closer to the instability the shape is, the larger is the mean asymmetry in the shape. Recent experiments indicate that both effects may contribute to the apparent stability of the weak pears (Döbereiner, n.d.).

3.7.3 Other shape transformations

Even though the budding transition has been studied most intensively there are further shape transformation which should also be related with the theory. The reentrant transition as shown in Fig. 1.2, has been reported to show no hysteresis at all (Berndl *et al.*, 1990; Kās & Sackmann, 1991). This transition could be explained within the bilayer couple model as demonstrated by the theoretical contours shown in Fig. 1.2 (Berndl *et al.*, 1990). The character of this transition will also persist in the ADE model at large enough α, but not for $\alpha \simeq 1$. Taking the experiment as well as the theory seriously, one would conclude that the vesicles for which this transition has been observed are multi-lamellar, which would correspond to an effectively larger α (Svetina & Zeks, 1992).

The discocyte-stomatocyte transition as shown in Fig. 1.3 was first reported to be con-

tinuous (Berndl *et al.*, 1990). However, closer inspection revealed a discontinuous character (Käs & Sackmann, 1991). So far, there are no comprehensive quantitative calculations of this transition within the ADE model at moderate α. Experimentally, this transition occurs more rarely than budding. This fact fits with the theoretical picture within the ADE model since one either needs a considerable negative asymmetric expansion coefficient γ, or an initial area difference smaller than the relaxed value 4π to reach this part of the phase diagram.

Obviously, more experimental information about these shape transitions are necessary before a comprehensive quantitative picture can emerge. To this end, it would be helpful to control the area difference m_0 better, which according to current wisdom depends on the number of molecules in the two monolayers.

There are two effects which indicate that m_0 can be modified by other factors than temperature. First, it was shown in (Farge & Devaux, 1992) and in (Mui *et al.*, 1994) that redistributing lipids from one monolayer to another by applying a transmembrane pH-gradient induces shape transformations similar to those predicted theoretically as one increases m_0. Secondly, the effect mentioned above, that precooling leads to budding, can, somewhat speculatively, also be related to changes in m_0 arguing from an intriguing suggestion (Boroske *et al.*, 1981). There, it is proposed that osmotically enforced flow of water through the membrane drags along lipid molecules. Since precooling also forces liquid to flow through the membrane, one could wonder whether such a treatment also causes an increase in m_0. In the phase diagram, shown in Fig. 3.7, this would shift the initially spherical vesicle upwards. A temperature trajectory starting at the sphere would then reach the budding line for a smaller temperature increase, and the size of the buds should be smaller. So far, there are no systematic tests of such an hypothesis.

Chapter 4

Fluctuations

The shape of lowest energy as calculated and systematized in the previous chapters does not include any effect of thermal fluctuations. Shape fluctuations that arise from the remarkable softness of the membrane are visible under the microscope. For phospholipid membranes, these fluctuations usually are not large enough to invalidate the notion of a well-defined mean shape, but they are an experimentally interesting and theoretically challenging phenomenon.

In this chapter, first, a theoretical approach to treat these fluctuations is presented in Sect. 4.1. The emphasis here will be mainly on elucidating the role of the constraints. Our approach has the advantage that all variants of the curvature model can be treated on the same footing. This leads to a transparent discussion of how fluctuations differ among the variants of the curvature model, or how they depend on α within the ADE model. In this respect, the present approach looks superior to a related scheme developed by Peterson, mainly applied to discocytes in the SC and the BC model, where the role of the constraints is somewhat hidden in the formalism.[1] Moreover, our approach allows to clarify and quantify the role of an effective tension for fluctuating vesicles. This concept has first been introduced for almost planar membranes (Helfrich & Servuss, 1984), for which it is thoroughly discussed in (David & Leibler, 1991). For vesicles, the notion arises from the intuitively reasonable expectation that the area constraint should restrict the fluctuations. However, for a non-spherical mean shape, there never has been a precise quantification of this tension let alone a prescription for how to calculate it.

The basic expansion parameter for these fluctuations is the ratio T/κ which is considered to be small. Such an expansion breaks down in the spherical limit, where another small parameter with the quantity $1-v$ enters. This limit is important since the bending rigidity, κ, has been extracted from the experimental analysis of the fluctuations of quasi-spherical

[1] (Peterson, 1985a; Peterson, 1985b; Peterson, 1985c; Peterson *et al.*, 1992; Peterson, 1992).

vesicles.[2] The analysis of these experiments is based on a theory in which the area constraint is not treated exactly but rather with a Lagrange multiplier, called "effective" or "entropic" tension (Milner & Safran, 1987). This approach demands further vindication since even though Lagrangean multipliers are well established for implementing constraints for mean shapes, i.e., for calculations involving the first variation, there is no justification a priori to use them for the calculation of fluctuations (which involves the second variation) in a constrained ensemble. In Sect. 4.2, we set up a scheme which allows exact treatment of the area constraint in the spherical limit. Our results, together with a calculation of the relative area fluctuations in the conventional approach, allow determination of the range of validity of the conventional treatment of the quasi-spherical case.

This chapter presents unpublished work and is inevitably more technical than the rest of the treatise even though we focus on the general theory while specific numerical results obtained with the new scheme will be discussed elsewhere (Nikolic *et al.*, 1994). Since later chapters are logically almost independent of the present chapter, it can be skipped without harm.

4.1 Gaussian fluctuations with constraints

4.1.1 Formalism

In this subsection, we set up an expansion of the fluctuations around the stationary shape in the small parameter T/κ. The fluctuating shape can be parametrized by

$$\mathbf{R}(s_1, s_2) = \mathbf{R}_0(s_1, s_2) + \epsilon(s_1, s_2)\mathbf{n}(s_1, s_2), \tag{4.1}$$

where $\mathbf{n}(s_1, s_2)$ is the local normal vector. The quantities of interest are both the thermal shift of the mean shape $< \epsilon(s_1, s_2) >$, which will be shown not to vanish, and correlation functions like $< \epsilon(s_1, s_2)\epsilon(s_1', s_2') >$. The bracket $< \ldots >$ denotes the appropriate thermal average and will be defined below.

The local normal displacement $\epsilon(s_1, s_2)$ is expanded,

$$\epsilon(s_1, s_2) = \sum_i a_i \epsilon_i(s_1, s_2), \tag{4.2}$$

[2] Experiments on quasi-spherical fluctuations are analysed in (Schneider *et al.*, 1984b; Engelhardt *et al.*, 1985; Bivas *et al.*, 1987; Faucon *et al.*, 1989; Duwe *et al.*, 1990; Meleard *et al.*, 1992). In an ingenious set-up, the bending rigidity was also determined in a micro-pipet experiment by measuring the area stored in the fluctuations (Evans & Rawicz, 1990). The bending rigidity has also been determined by measuring the fluctuations of cylindrical membranes (Schneider *et al.*, 1984a) and fluctuations of almost planar membrane segments (Mutz & Helfrich, 1990) .

in a set of basis functions $\{\epsilon_i\}$. For axisymmetric vesicles, the spherical harmonics

$$\epsilon_i(s_1, s_2) \equiv Y_{l,m}(s\pi/s^*, \phi). \tag{4.3}$$

with $a_{l,-m} = (-1)^m a^*_{l,m}$ are a convenient basis. Here, s^* is the length of the contour from north pole to south pole. The formal index i has thus become a double index (l, m) and the $\sum_i$ is defined as

$$\sum_i \equiv \sum_{l=0}^{l_{max}} \sum_{m=-l}^{l} \tag{4.4}$$

with some upper cutoff l_{max}. This leads to a total number of modes

$$N = \sum_{l=0}^{l_{max}} \sum_{m=-l}^{l} = (l_{max} + 1)^2. \tag{4.5}$$

In order not to overburden the notation we will keep the short hand notation with just one index i. The expansion based on Eqs. (4.2) and (4.3) can deal with any axisymmetric stationary shape, whether it is star-shaped or not. In particular, this expansion is not restricted to nearly spherical shapes.

We will first consider the fluctuations in the BC model, the other cases then becoming trivial modifications. The geometrical quantities area, volume, mean curvature as well as the bending energy G can be expanded in the set $\{a_i\}$. Formally, one thus obtains

$$G = G_0 + g_i a_i + (1/2) a_i G_{ij} a_j + O(a_i^3), \tag{4.6}$$

$$A = A_0 + R_0^2 \left(d_i^{(1)} a_i + (1/2) a_i D_{ij}^{(1)} a_j + O(a_i^3) \right), \tag{4.7}$$

$$V = V_0 + R_0^3 \left(d_i^{(2)} a_i + (1/2) a_i D_{ij}^{(2)} a_j + O(a_i^3) \right), \tag{4.8}$$

and

$$M = M_0 + R_0 \left(d_i^{(3)} a_i + (1/2) a_i D_{ij}^{(3)} a_j + O(a_i^3) \right). \tag{4.9}$$

Here, and from now on, summation over double indices will be understood. Specifically for axisymmetric vesicles, the quantities g_i, G_{ij}, d_i^α and D_{ij}^α can be expressed as integrals over the contour. The integrands are quantities such as the local curvature and Legendre polynomials and derivatives thereof. The specific expressions are lengthy (Nikolic *et al.*, 1994) and will not be needed for the general discussion to follow.

Since $\mathbf{R}_0(s_1, s_2)$ is a stationary shape at constant area, volume and mean curvature, enforced by the Lagrange multipliers Σ, P and Q, we have from Eq. (2.58) for all i

$$\kappa g_i + \Sigma R_0^2 d_i^{(1)} + P R_0^3 d_i^{(2)} + Q R_0 d_i^{(3)} = 0. \tag{4.10}$$

Thermal expectation values are now defined as

$$< h\{a_i\} >\equiv \frac{1}{Z}\int \mathcal{D}\{a_i\}\delta\left(\frac{A-A_0}{R_0^2}\right)\delta\left(\frac{V-V_0}{R_0^3}\right)\delta\left(\frac{M-M_0}{R_0}\right)\exp\left(\frac{-\kappa(G-G_0)}{T}\right)h\{a_i\}. \tag{4.11}$$

The partition function Z is defined as

$$Z\equiv\int \mathcal{D}\{a_i\}\delta\left(\frac{A-A_0}{R_0^2}\right)\delta\left(\frac{V-V_0}{R_0^3}\right)\delta\left(\frac{M-M_0}{R_0}\right)\exp\left(\frac{-\kappa(G-G_0)}{T}\right). \tag{4.12}$$

The crucial issue is to define the measure $\mathcal{D}\{a_i\}$, which should physically correspond to an integration over all surfaces close to the stationary shape not counting any surface twice. We will argue in Sect. 4.1.4. below that the naive measure

$$\int \mathcal{D}\{a_i\}\equiv\prod_{l=0}^{l_{max}}\left(\prod_{m=0}^{l}\int_{-\infty}^{\infty}\frac{d\Re\,(a_{l,m})}{\sqrt{2\pi}}\right)\left(\prod_{m=1}^{l}\int_{-\infty}^{\infty}\frac{d\Im\,(a_{l,m})}{\sqrt{2\pi}}\right). \tag{4.13}$$

is sufficient to the low order in T/κ in which we work.

It is convenient to introduce a generating functional

$$Z(\{J_i\})\equiv\int \mathcal{D}\{a_i\}\delta\left(\frac{A-A_0}{R_0^2}\right)\delta\left(\frac{V-V_0}{R_0^3}\right)\delta\left(\frac{M-M_0}{R_0}\right)\exp\left(\frac{-\kappa(G-G_0)}{T}\right)\exp(J_i a_i), \tag{4.14}$$

from which correlation functions can be obtained by simple derivatives such as

$$< a_i >= \partial_{J_i} lnZ|_{\{J_i=0\}} \tag{4.15}$$

and

$$< a_i a_j >= \partial_{J_i}\partial_{J_j} lnZ|_{\{J_i=0\}}. \tag{4.16}$$

The essential step is to write the three δ-functions in (4.11) as Fourier integrals in the form

$$\delta(x)=\exp\left(\frac{-\kappa\lambda^\alpha x}{T}\right)\int_{-\infty}^{\infty}\frac{dk^\alpha}{2\pi}\exp(ik^\alpha x) \tag{4.17}$$

where $\alpha = 1,2,3$ (no summation on α!) and the set of scaled Lagrange multipliers $\{\lambda^\alpha\}$ is defined as $\lambda^1\equiv\Sigma/\kappa$, $\lambda^2\equiv P/\kappa$ and $\lambda^3\equiv Q/\kappa$, respectively. The prefactor in front of the integral in (4.17) will compensate the linear term $g_i a_i$ when inserted into the generating funtional (4.14). For small T/κ, it will be sufficient to use the expansions (4.6-4.9) up to quadratic order in a_i. Inserting these expansions into the generating functional, one gets

$$Z(\{J_i\})\equiv\int \mathcal{D}\{a_i\}\left[\prod_{\gamma=1}^{3}\int_{-\infty}^{\infty}\frac{dk^\gamma}{2\pi}\right]\exp\left(-\frac{\kappa}{2T}a_i(S_{ij}-\frac{T}{\kappa}ik^\alpha D^\alpha_{ij})a_j\right)\exp\left((ik^\beta d^\beta_l+J_l)a_l\right). \tag{4.18}$$

Here, the *stability matrix* **S** with matrix elements

$$S_{ij} \equiv G_{ij} + \lambda^\alpha D^\alpha_{ij} \tag{4.19}$$

is obtained from the second variation of both the curvature energy and the geometrical constraints.

To set up a perturbation theory, it is useful to note that $a_i \sim (T/\kappa)^{1/2}$, $k^\alpha \sim (T/\kappa)^{-1/2}$, and $J_i \sim (T/\kappa)^{-1/2}$, which follows from the fact that generically both S_{ij} and d_i are of order 1. Since we are interested in small T/κ we can thus expand the first exponential in the expression (4.18) and write it in the form

$$\exp\left(-\frac{\kappa}{2T}a_i(S_{ij} - \frac{T}{\kappa}ik^\alpha D^\alpha_{ij})a_j\right) \approx \exp\left(-\frac{\kappa}{2T}a_i S_{ij} a_j\right)\left(1 + i\frac{1}{2}k^\alpha \partial_{J_m} D^\alpha_{mn}\partial_{J_n}\right). \tag{4.20}$$

It can be checked that higher order terms in this expansion do not contribute to the low order T/κ.

If the stability matrix **S** is positive definite, the Gaussian integrals over the $\{a_i\}$ in (4.18) can be performed easily. This leads to

$$Z(\{J_i\}) = \frac{1}{\det^{1/2}\mathbf{S}}\left[\prod_{\alpha=1}^{3}\int_{-\infty}^{\infty}\frac{dk^\alpha}{2\pi}\right]\left(1 + i\frac{1}{2}k^\alpha\partial_{J_m}D^\alpha_{mn}\partial_{J_n}\right)\exp\left(\frac{T}{2\kappa}(ik^\beta d^\beta_i + J_i)S^{-1}_{ij}(ik^\gamma d^\gamma_i + J_j)\right). \tag{4.21}$$

In fact, a slight complication arises here from the presence of trivial zero-modes associated with rigid motion of the shape (Peterson, 1985b). The solution of how to overcome this more technical issue will be discussed in Sect. 4.1.4 below. Finally, we perform the Gaussian integrals over the k^α which yields

$$Z(\{J_i\}) = \frac{1}{\det^{1/2}\mathbf{S}}\frac{1}{\det^{1/2}\mathbf{W}}\frac{1}{(2\pi)^{3/2}}\left(1 - \frac{1}{2}\partial_{J_m}\partial_{J_n}D^\alpha_{mn}(W^{\alpha\beta})^{-1}d^\beta_p S^{-1}_{ps}J_s\right)\exp\left(\frac{T}{2\kappa}J_i C_{ij}J_j\right). \tag{4.22}$$

The matrix **W** with elements

$$W^{\alpha\beta} \equiv d^\alpha_i S^{-1}_{ij} d^\beta_j. \tag{4.23}$$

is a 3×3 matrix with respect to the Greek indices. The correlation matrix **C** has elements

$$C_{ij} \equiv \left(S^{-1}_{ij} - d^\alpha_k S^{-1}_{ik} W^{\alpha\beta^{-1}} S^{-1}_{jl} d^\beta_l\right) \quad . \tag{4.24}$$

4.1.2 Correlation functions

If the generating functional (4.22) is inserted into (4.16), the correlation functions of the amplitudes $\{a_i\}$ are obtained as

$$< a_i a_j >= \frac{T}{\kappa}C_{ij} = \frac{T}{\kappa}\left(S^{-1}_{ij} - d^\alpha_k S^{-1}_{ik} W^{\alpha\beta^{-1}} S^{-1}_{jl} d^\beta_l\right) \quad . \tag{4.25}$$

In order to discuss this expression from a general perspective, it is useful to classify the set of modes $\{\epsilon_i\}$ according to their symmetry properties. Modes that break a symmetry of the stationary shape will be called *symmetry-breaking modes*. For an axisymmetric vesicle, all modes with index $m \neq 0$ are symmetry-breaking modes. If, moreover, the stationary shape possesses reflection symmetry, the modes with $m = 0$ and l uneven belong to this class, too. By symmetry, the first variation in the geometrical quantities and the bending energy vanishes identically for these modes, i.e., $d_i^\alpha = g_i = 0$. The remaining *symmetry-preserving modes* do not change the symmetry of the mean shape and will thus, in general, have linear terms $d_i^\alpha \neq 0$ and $g_i \neq 0$.

The stability matrix **S** factors in these two classes and, moreover, within each class in different subclasses according to the symmetry of the respective modes. In particular, for an axisymmetric mean shape with reflection symmetry, the modes with different index $|m|$ do not mix, and neither do those with different parity but the same $|m|$. Therefore, one can discuss the correlations of these two classes of modes separately.

For the *symmetry-breaking modes*, we have the simple result

$$< a_i a_j >= \frac{T}{\kappa} S_{ij}^{-1} \tag{4.26}$$

for the correlation function, which is remarkable for the following reason. Suppose we had calculated the correlation function in the Φ-ensemble (2.57) in which the terms $\Sigma A + PV + QM$ count as "real" energy assuming that the "fields" Σ, P and Q are external parameters. For fluctuations in the Φ−ensemble, we would have obtained exactly the result (4.26) since the stability matrix S is nothing but the second variation of the energy Φ as follows from Eq.(4.19). Thus, the correlations of all symmetry breaking modes do not depend on whether one imposes hard constraints or whether one considers the terms $\Sigma A + PV + QM$ as contributing to the energy. This result has profound consequences for the interpretation of the Lagrange multipliers Σ, P and Q in later applications. In particular, one can consider Σ as a tension restricting (or promoting, depending on its sign) the fluctuations.

However, the equivalence of the fluctuations in the BC-model and the Φ-ensemble is not complete since for all modes which preserve the axisymmetry, i.e., in particular, for fluctuations of the contour of an axisymmetric vesicle, the additional term in (4.24) shows that fluctuations in the constrained ensemble are different from those where the $\Sigma A + PV + QM$ term is treated as a real energy. This distinction in the correlation function between modes that break a symmetry and those that do not is a central result of this approach.

4.1.3 Thermal shift of the mean shape

The modes that do not break a symmetry of the stationary shape acquire a finite temperature shift to make up for the area – and, strictly speaking, also for the volume and the mean curvature – stored in the fluctuating modes. If (4.22) is inserted into equation (4.15), one obtains

$$< a_i >= -\frac{T}{\kappa}\, d_k^{\alpha}\, W^{-1\alpha\beta}\, D^{\beta}_{mn} \left(2S^{-1}_{kn} C_{mi} + S^{-1}_{ki} C_{mn}\right). \tag{4.27}$$

This expression yields the shift in the mean shape which then follows as

$$< \mathbf{R}(s_1, s_2) >= \mathbf{R}_0(s_1, s_2) + \sum_i < a_i > \epsilon_i(s_1, s_2)\mathbf{n}(s_1, s_2). \tag{4.28}$$

For an axisymmetric vesicle, this expression can be reduced to a shift of the mean contour, since $\sum_i$ includes contributions from the $(m = 0)$-modes only. The thermal shift is of order T/κ and thus much smaller than a typical fluctuation, which scales as $a_i \sim (T/\kappa)^{1/2}$.

4.1.4 Remarks on the measure

The correct definition of a measure related to a fluctuating fluid membrane is a delicate problem. The purpose of this section, which draws strongly on the illuminating works (Cai *et al.*, 1994) and (Nelson & Powers, 1993), is to present the evidence that the naive measure used in (4.13) yields the correct results for the correlation function (4.25) and the thermal shift (4.27) to the low order T/κ in which we work.

Defining a measure for the integration over surfaces requires a discretization. While one could use a grid of size a in real space, any expansion in basis functions usually resembles more to a Fourier representation. The appropriate generalization of a Fourier transformation on the stationary shape are the eigenfunctions $\{\hat{\epsilon}_i\}$ of the Laplace-Beltrami operator (2.65). If the set of these eigenfunctions $\{\hat{\epsilon}_i\}$ are truncated at an eigenvalue of the order of $1/a^2$, this set should provide a reasonable basis for an expansion of the normal displacement $\epsilon(s_1, s_2)$.

In defining a measure for the expansion coefficients $\hat{a}_i$ of a normal displacement in the basis $\{\hat{\epsilon}_i\}$, one has to avoid over-counting surfaces which are the same except for reparametrization. This problem is tackled in (Cai *et al.*, 1994) in some detail. It is shown that in the normal gauge we are using here, the Fadeev-Popov factor $\mathcal{F}$ which takes care of this reparametrization can be expanded as form $\mathcal{F} = 1 + \text{const} \times \epsilon^2$ which leads to $\mathcal{F}(\hat{a}_i) = 1 + \hat{\mathcal{F}}_{ij}\hat{a}_i\hat{a}_j$, where $\hat{\mathcal{F}}_{ij}$ is a matrix which depends on the stationary shape.

Thus, at this stage, the proper measure to use in (4.11) and (4.12) would have been

$$\int \mathcal{D}\{\hat{a}_i\} \equiv \prod_{i=1}^{N} \int_{-\infty}^{\infty} \frac{d\hat{a}_i}{\sqrt{2\pi}} \left(1 + \hat{\mathcal{F}}_{ij}\hat{a}_i\hat{a}_j\right). \tag{4.29}$$

Since it is convenient to stick with the basis $\{\epsilon_i\}$, one should express this measure in terms of the $\{a_i\}$ which yields

$$\int \mathcal{D}\{\hat{a}_i\} = \mathcal{J} \prod_{i=1}^{N} \int_{-\infty}^{\infty} \frac{da_i}{\sqrt{2\pi}} (1 + \mathcal{F}_{ij} a_i a_j) . \tag{4.30}$$

Here, $\mathcal{J}$ is the Jacobian for the linear transformation from $\{\hat{\epsilon}_i\}$ to $\{\epsilon_i\}$ and $\mathcal{F}_{ij}$ arises from $\hat{\mathcal{F}}_{ij}$ by the appropriate transformation. The crucial point is that using this measure (4.30) instead of (4.13) does not change the results (4.25) and (4.27) to lowest order in T/κ. First, the Jacobian $\mathcal{J}$ is just a number since $\{\hat{\epsilon}_i\}$ and $\{\epsilon_i\}$ are related by a linear transformation. Secondly, the Fadeev-Popov factor yields only a higher order correction as can be verified easily.

Apart from the Fadeev-Popov factor, it is stressed in (Cai *et al.*, 1994) that there is another correction to the measure which arises from the fact that the displaced surface has, in general, a different area than the original surface and thus, superficially, has more (or less) degrees of freedom. For a general surface, this so-called Liouville factor has not yet been calculated in normal gauge. Still, it is clear that this factor cannot modify the correlation functions given in (4.25) to this order in T/κ. Less obvious is its effect on the thermal shift (4.27). Since we keep the area of the fluctuating surface constant, one would expect that the Liouville factor does not modify this expressions either but a rigorous proof of this statement has to be left for future work.

Finally, we comment on the fact that due to Euclidean invariance, several trivial zero modes appear in the expansion (4.2). For a generic shape, there are three translations and three rotations which leave the shape invariant (Peterson, 1985b). These modes should not be included in the functional integral (4.13) from the outset. In practice, one can diagonalize the stability matrix S where these modes show up as $N_e = 5$ or 6 zero modes depending on whether or not the shape is axisymmetric.

The functional integral (4.13) should thus be replaced by

$$\int \mathcal{D}\{a_i\} \to \int \mathcal{D}\{\tilde{a}_i\} \equiv \tilde{\mathcal{J}} \prod_{i=1}^{N-N_e} \int_{-\infty}^{\infty} \frac{d\tilde{a}_i}{\sqrt{2\pi}} . \tag{4.31}$$

Here, the set $\{\tilde{a}_i\}$ are the expansion coefficients with respect to a basis $\{\tilde{\epsilon}_i\}$ of eigenvectors of the stability matrix S. The product runs only over those modes which do not belong to the Euclidean zero eigenvalues of S. Again the Jacobian, $\tilde{\mathcal{J}}$, is an irrelevant number. In this new basis, quantities like $g_i, G_{ij}, d_i^{\alpha}$ and D_{ij}^{α} should acquire a tilde, too. We assume that from Eq.(4.20) onwards this change of basis has been tacitly performed, and that the tildes have been dropped to keep the notation simple.

4.1.5 Results for other variants

The formalism and the discussion of the results have been set up within the BC model. A strength of the approach introduced here is its flexibility with which it can be used to discuss mean shape shifts and correlations in the other variants of the curvature model.

For the SC model, we have only two constraints but a different energy. Technically speaking, this amounts to replacing G by $G-2C_0M+C_0^2A/2$ which entails the replacements

$$g_i \to g_i - 2C_0R_0d_i^{(3)} + (C_0R_0)^2 d_i^{(1)}/2 \tag{4.32}$$

and

$$G_{ij} \to G_{ij} - 2C_0R_0D_{ij}^{(3)} + (C_0R_0)^2 D_{ij}^{(1)}/2. \tag{4.33}$$

Since the Lagrange multipliers are accordingly changed as shown in Table 2.2, the stability matrix occurring in (4.18) remains exactly the same as the one given in (4.19). Therefore, the correlation functions of the symmetry-breaking modes for the SC-model are exactly the same as in the BC-model. For the symmetry-preserving modes, both the fluctuations and the mean shape shifts are still given by (4.25) and (4.27), respectively. However, the sums over Greek indices run only through 1 and 2, which lead to different numerical values.

For the ADE model, the energy G has to be replaced by $G+(\alpha/2R_0^2)(M-M_0)^2$. With the corresponding changes in the g_i and the G_{ij}, one finds for the stability matrix the replacement

$$S_{ij} \to S_{ij} + \alpha d_i^{(3)} d_j^{(3)}. \tag{4.34}$$

With this modification, the results (4.27) and (4.25) for the mean shape shift and the correlation function still holds, with Greek indices running only through 1 and 2. Since $d_i^{(3)} = 0$ for all symmetry-breaking modes, the correlation functions for these modes are again identical to those in the BC-model. The difference between the various ensembles shows up only in the correlations involving symmetry-preserving modes.

For the ADE model with spontaneous curvature, the same results as for the ADE model without spontaneous curvature hold. Thus, a spontaneous curvature within the ADE model has, for $\alpha \neq 0$, no observable effects whatsoever in Gaussian fluctuations. Likewise, it is obvious how to obtain the correlation functions for the most general energy B defined in (2.60).

4.1.6 Stability

So far, we have implicitly assumed that the stationary shape is locally stable with respect to the deformations as parametrized by the expansion (4.2) once the Euclidean modes are

excluded. Of course, the same approach also leads to a stability criterion which can be read off from the correlation matrix C defined in Eq. (4.25). Due to the presence of constraints, the matrix C has to have three zero eigenvalues for the BC model and two zero eigenvalues for those variants where only two hard constraints are imposed. These eigenvalues always show up in the class of symmetry-preserving modes. If, moreover, the correlation matrix has negative eigenvalues, the shape is unstable.

Two cases of negative eigenvalues of the correlation matrix must be distinguished. If the negative eigenvalue arises within the modes which break a symmetry, the stability matrix already exhibits this negative eigenvalue. Such a shape will be unstable with respect to the corresponding eigenvector in all variants of the curvature model. This result is the basis for the statement made in Sect. 3.2.1 that stability with respect to a deformation which breaks a symmetry does not depend on the variants of the curvature model under consideration.

If the negative eigenvalue of the matrix C arises within the modes which keep the symmetry of the shapes, then the stability of this particular shape indeed depends on the variant of the curvature model under consideration. An example are the pears with the weak asymmetry, which are unstable for small α and become stable for larger α as discussed in Sect. 3.1.

4.1.7 Spherical limit

As the mean shape around which the expansion has been performed approaches the sphere, the fluctuations should become smaller since for a sphere as $T = 0$-shape, there is no area available for fluctuations at constant volume. In the approach outlined above, the modes with different l no longer mix in this limit. Therefore, the correlation matrix is given by the inverse of the stability matrix S, which becomes in the spherical limit

$$< |a_{l,m}|^2 > \approx \frac{T}{\kappa} \frac{1}{(l+2)(l-1)(l^2+l-6)} \tag{4.35}$$

for all variants of the curvature model.

This expression diverges for the $l = 2$-mode, which points to an inconsistency. In fact, in the spherical limit another small parameter, $1 - v$, arises which invalidates the naive expansion in T/κ.

4.2 Quasi-spherical vesicles

4.2.1 Expansion around the sphere

The spherical limit has to be analysed within a different approach, which allows to keep track of both small parameters, T/κ and $1-v$. The fluctuating shape is not expanded around the corresponding stationary shape but rather around a sphere with the same volume

$$V \equiv \frac{4\pi}{3} R_V^3, \tag{4.36}$$

which defines R_V. We consider a fixed area

$$A \equiv (4\pi + \Delta) R_V^2, \tag{4.37}$$

which defines the (dimensionless) excess area Δ used traditionally as a small parameter instead of $1-v$.

A quasi-spherical vesicle can be parametrized by spherical harmonics

$$R(\theta,\phi) = R_V \left(1 + \sum_{l\geq 2}^{l_{max}} \sum_{m=-l}^{l} u_{l,m} Y_{lm}(\theta,\phi) \right), \tag{4.38}$$

where $|m| \leq l$ and $u_{l,-m} = (-1)^m u_{l,m}^*$. Expanding the geometrical quantities as well as the bending energy around a sphere, one has (Helfrich, 1986; Milner & Safran, 1987; Ou-Yang & Helfrich, 1989)

$$G = 8\pi + \frac{1}{2} \sum_{l\geq 1}^{l_{max}} \sum_{m=-l}^{l} |u_{l,m}|^2 (l+2)(l+1)l(l-1) + O(|u_{l,m}|^3), \tag{4.39}$$

$$A = R_V^2 \left(4\pi \left(1 + \frac{u_{0,0}}{\sqrt{4\pi}} \right)^2 + \sum_{l\geq 1}^{l_{max}} \sum_{m=-l}^{l} |u_{l,m}|^2 (1 + l(l+1)/2 + O(|u_{l,m}|^3)) \right), \tag{4.40}$$

and

$$V = R_V^3 \left(\frac{4\pi}{3} \left(1 + \frac{u_{0,0}}{\sqrt{4\pi}} \right)^3 + \sum_{l\geq 1}^{l_{max}} \sum_{m=-l}^{l} |u_{l,m}|^2 + O(|u_{l,m}|^3) \right). \tag{4.41}$$

The volume constraint (4.36) fixes the amplitude $u_{0,0}$ as a function of the other amplitudes

$$u_{0,0} = -\sum_{l\geq 1}^{l_{max}} \sum_{m=-l}^{l} |u_{l,m}|^2 / \sqrt{4\pi}, \tag{4.42}$$

where we truncate from now on cubic terms. If the relation (4.42) is inserted into (4.40), the area constraint (4.37) becomes

$$\sum_{l\geq 1}^{l_{max}} \sum_{m=-l}^{l} |u_{l,m}|^2 \frac{(l+2)(l-1)}{2} = \Delta \tag{4.43}$$

Since the $(l=1)$-modes correspond to translations, which have to be omitted, from now on all sums start at $l=2$. It is convenient to absorb both the l-dependence of the area term and a factor T/κ into the amplitudes by defining

$$v_{l,m} \equiv u_{l,m}\left(\frac{\kappa}{T}\frac{(l+2)(l-1)}{2}\right)^{1/2}. \tag{4.44}$$

We also define the ratio

$$\tau \equiv \frac{T}{\kappa\Delta}. \tag{4.45}$$

4.2.2 Exact treatment of the area constraint

We determine the amplitudes in the minimal model since the other variants of the curvature model lead to the same results at the level considered here as shown in Sect. 4.2.4. below.

The mean-square amplitudes $< |v_{l,m}|^2 >$ then follow from the constraint (4.43) and the Boltzmann factor with the energy G as

$$\begin{aligned} < |v_{l,m}|^2 > &= \frac{1}{Z}\int \mathcal{D}\{v_{l,m}\}\delta\left(\sum_{l\geq 2}\sum_{m=-l}^{l}|v_{l,m}|^2 - 1/\tau\right)|v_{l,m}|^2 \exp\left(-\sum_{l\geq 2}\sum_{m=-l}^{l} p_l|v_{l,m}|^2\right) \\ &= -\frac{1}{(2l+1)}\frac{\partial}{\partial p_l}\ln Z. \end{aligned} \tag{4.46}$$

After performing the derivative, p_l has to be set to

$$p_l \equiv l(l+1). \tag{4.47}$$

The partition function Z is defined as

$$Z \equiv \int \mathcal{D}\{v_{l,m}\}\delta\left(\sum_{l\geq 2}\sum_{m=-l}^{l}|v_{l,m}|^2 - 1/\tau\right)\exp\left(-\sum_{l\geq 2} p_l|v_{l,m}|^2\right). \tag{4.48}$$

The factor $1/(2l+1)$ in (4.46) arises from the degeneracy of the energy with respect to m.

The discretized functional integral is defined as

$$\int \mathcal{D}\{v_{l,m}\} \equiv \prod_{l=2}^{l_{max}}\left(\prod_{m=0}^{l}\int_{-\infty}^{\infty}\frac{d\Re\,(v_{l,m})}{\sqrt{2\pi}}\right)\left(\prod_{m=1}^{l}\int_{-\infty}^{\infty}\frac{d\Im\,(v_{l,m})}{\sqrt{2\pi}}\right). \tag{4.49}$$

Without the constraint, the partition function would be a trivial Gaussian integral. Introducing the usual Fourier transformation for the δ–function, $\delta(x) = \int_{-\infty}^{\infty} d\lambda/2\pi e^{-i\lambda x}$, the integrals over the $v_{l,m}$ become Gaussian and can easily be performed. Thus one obtains

$$Z = \int_{-\infty}^{\infty}\frac{d\lambda}{2\pi}\, e^{i\lambda/\tau}\prod_{l\geq 2}^{l_{max}}(p_l + i\lambda)^{-(l+1/2)}. \tag{4.50}$$

In principle, this one-dimensional integral could be analysed numerically. However,as shown below, the approximations made by ignoring higher order terms in (4.39)-(4.41) are consistent only for small and for large τ. In both cases, an analytical calculation of Z is possible.

For $\tau \ll 1$, i.e., for $T/\kappa << \Delta$, the integral can be treated by a saddle-point-like approach. First, one applies Cauchy's theorem and closes the path of integration in the upper complex λ half-plane. The integrand has branch-cuts originating at $\lambda = ip_l$ which we choose parallel to the positive real-λ-axis. For small τ, only the singularity with the smallest imaginary part which is the branch-cut along $\lambda = ip_2 + \epsilon$ contributes. The integral around this branch leads to

$$Z = \frac{8}{3}\frac{\partial^2}{\partial p_2^2}\left[e^{-p_2/\tau}\int_0^\infty d\epsilon\, e^{i\epsilon/\tau}(i\epsilon)^{-1/2}\prod_{l\geq 3}^{l_{max}}(p_l - p_2 + i\epsilon)^{-(l+1/2)}\right]\left[1 + O(e^{-(p_3-p_2)/\tau})\right]. \quad (4.51)$$

For small τ, the integral yields

$$Z \approx \frac{8}{3}\frac{\partial^2}{\partial p_2^2}\left[e^{-p_2/\tau}\Gamma(1/2)\tau^{1/2}\prod_{l\geq 3}^{l_{max}}(p_l - p_2)^{-(l+1/2)}\right]. \quad (4.52)$$

Inserting this into Eq.(4.46) and expressing the result in terms of the amplitudes $u_{l,m}$ leads to

$$< |u_{l,m}|^2 >= \frac{T}{\kappa}\left[\frac{1}{(l+2)(l-1)(l^2+l-6)} + O(\tau)\right] \quad (4.53)$$

for $l \geq 3$ and

$$< |u_{l,m}|^2 >= \frac{\Delta}{5}\left[\frac{1}{2} - \tau\sum_{l\geq 3}\frac{2l+1}{(l+2)(l-1)(l^2+l-6)} + O(\tau^2)\right] \quad (4.54)$$

for $l = 2$.

The leading term for $l \geq 3$ is exactly what we found in Sect. 4.1.7 in the spherical limit. Thus, the direct evaluation of the correlation functions in the spherical limit shows that the procedure described in Sect. 4.1.7 holds (for $l \geq 3$) in the double limit $\Delta \to 0$ *after* $T/\kappa \to 0$. In addition, the leading term for the amplitude for the $(l = 2)$-modes is obtained correctly. These modes pick up most of the excess area. Of course, the distribution of this area among the five $(l = 2)$-modes cannot be obtained in the quadratic approximation. Note also that the area constraint is obeyed exactly as the second order contribution in (4.54) shows.

In principle, one could continue the expansions (4.53) and (4.54) to higher orders in τ. However, this would lead to misleading results since the terms which have been omitted in the quadratic expansions (4.39)-(4.41) are more relevant than those higher order terms.

Consider, e.g., the omitted terms of the form $u_{2,m}^{2n}u_{4,m'}^{2}$ with $n \geq 1$, which are of the order $\Delta^n T/\kappa$. In the limit $\tau \to 0$, such a term is not small compared to $(T/\kappa)\tau$ which are the next to leading order term in (4.53). This comparison shows that in order to improve the values given in (4.53) one would have to include all terms of the form $u_{2,m}^{2n}u_{4,m'}^{2}$, i.e., one would have to expand around the stationary shape rather than around the sphere.

For $\tau \gg 1$, i.e. for $\Delta \ll T/\kappa$, integrating over the $u_{l,m}$ is not so convenient. Inspection of (4.46) shows that in this case the bending energy can be treated as small perturbation. The zero order term is defined by the partition function

$$Z_0 \equiv \int \mathcal{D}\{v_{l,m}\}\delta\left(\sum_{l\geq 2}\sum_{m=-l}^{l}|v_{l,m}|^2 - 1/\tau\right) \tag{4.55}$$

In lowest order, all $v_{l,m}$ thus have the same amplitude $< |v_{l,m}|^2 >= 1/(\tau N)$, which leads to

$$< |u_{l,m}|^2 > \approx \frac{2\Delta}{N(l+2)(l-1)}. \tag{4.56}$$

In this regime, all N modes share the available excess area as previously observed by (Milner & Safran, 1987). Corrections to this result are for the order $1/\tau$ and can be obtained by expanding the exponential in (4.46) and performing the averages with Z_0. In the limit $\Delta \to 0$, i.e. for $\tau \to \infty$, the fluctuations vanish. However, one then enters a different physical regime in which the stretching of the membrane must be taken into account.

In summary, the analysis given in this section shows that an analytical calculation of the fluctuations of quasi-spherical vesicles taking into account the area constraint exactly is possible for large and small τ. An expansion beyond the leading term for small τ does not fail due to the absence of an analytical scheme but rather due to the relevance of the higher order terms in the expansions (4.39)-(4.41).

4.2.3 Conventional approach with effective tension

We now discuss the conventional approach to fluctuations in the quasi-spherical limit (Schneider *et al.*, 1984b; Milner & Safran, 1987; Faucon *et al.*, 1989). First, in these works the relevance of the higher order terms in the expansions (4.39)-(4.41) are tacitly neglected. Therefore, this approach inevitably suffers from the same deficiencies as the exact approach in this respect. Secondly, the area constraint is not treated exactly by introducing a δ-function in the partition function (4.48) but rather by a Lagrange multiplier which requires further justification.

We discuss this approach here for the minimal model since the other variants lead to the same result as shown in Sect. 4.2.4. The mean-square amplitudes in this approach are

calculated with the Boltzmann factor

$$\exp\left(-(\kappa G + \bar{\Sigma} A)/T\right), \tag{4.57}$$

where the "tension" $\bar{\Sigma}$ is another, yet free, Lagrangean multiplier to be distinguished by the over-bar from the Lagrange multiplier Σ used in calculating the stationary shape. After inserting the quadratic expansions (4.39)-(4.41) into energy and area, with $u_{0,0}$ replaced by the volume constraint (4.42), one obtains

$$\kappa G + \bar{\Sigma} A \approx const + \frac{\kappa}{2} \sum_{l \geq 2}^{l_{max}} \sum_{m=-l}^{l} |u_{l,m}|^2 (l+2)(l-1)\left((l+1)l + \bar{\sigma}\right), \tag{4.58}$$

with the dimensionless effective tension

$$\bar{\sigma} \equiv \bar{\Sigma} R_V^2 / \kappa. \tag{4.59}$$

If this expression is used as a Boltzmann weight for the amplitudes $\{u_{l,m}\}$, one immediately obtains the mean square amplitudes (Milner & Safran, 1987)

$$< |u_{l,m}|^2 >= \frac{T}{\kappa} \frac{1}{(l+2)(l-1)\left((l+1)l + \bar{\sigma}\right)}. \tag{4.60}$$

These expressions for the mean square amplitudes have been used to determine experimentally the bending rigidity κ from the contour fluctuations of quasi-spherical vesicles using phase contrast microscopy combined with fast image processing (Schneider *et al.*, 1984b; Engelhardt *et al.*, 1985; Bivas *et al.*, 1987; Faucon *et al.*, 1989; Duwe *et al.*, 1990; Meleard *et al.*, 1992). In this approach, $\bar{\sigma}$ is usually either set to 0 or treated as a fit parameter for which one typically obtains values in the range $0 \lesssim \bar{\sigma} \lesssim 100$.

Since the Lagrangian multiplier $\bar{\Sigma}$ has been introduced only to enforce the area constraint, it should, in fact, be eliminated in favor of the excess area Δ which is the physically meaningful quantity. Inserting the mean square amplitudes (4.60) into the expansion of the area and comparing with the constraint (4.37) yields an implicit equation (Bivas *et al.*, 1992),

$$\sum_{l \geq 2}^{l_{max}} \frac{2l+1}{l^2 + l + \bar{\sigma}(\Delta)} = \frac{2\Delta\kappa}{T} = \frac{2}{\tau}, \tag{4.61}$$

for $\bar{\sigma}$. An analogous relation was first derived for almost planar membranes (Helfrich & Servuss, 1984). The relation (4.61) shows that $\bar{\sigma}$ depends on the excess area only in the combination $\Delta\kappa/T = 1/\tau$. Thus, after elimination of the effective tension, the mean square amplitudes as given by (4.60) depend only on the three quantities, T/κ, τ, and the cutoff l_{max}.

In general, (4.61) has to be inverted numerically to yield $\bar{\sigma} = \bar{\sigma}(\tau, l_{max})$. It is instructive to discuss limit cases analytically. For small τ, one finds

$$\bar{\sigma} \approx -6 + \frac{5}{2}\tau + O(\tau^2). \tag{4.62}$$

Inserting this value into (4.60), one recovers the exact limits (4.53) and (4.54). However, the next to leading order terms in an expansion in τ of either (4.60) or (4.53) do *not* coincide.

The fact that the effective tension is negative for small τ may look strange at first sight, but becomes clear in view of the relation (2.59). In fact, $\Sigma R_0^2/\kappa = -6$ is also the spherical limit of the (dimensionless) Lagrangean multiplier for prolate and oblate ellipsoids. The effective tension for fluctuations is negative, thus promoting fluctuations, because if area is taken up by the fluctuations with $l \geq 3$, the curvature energy stored in the $(l = 2)$-modes decreases. For $l \geq 3$, the fluctuations with area constraint are thus larger than without an area constraint which shows again that one should interpret the effective tension quite carefully.

For large τ, one obtains from (4.61)

$$\bar{\sigma} \approx \frac{\tau}{2} l_{max}^2, \tag{4.63}$$

which after insertion into the mean square amplitudes again coincides with the exact limit (4.56).

If the inversion of (4.61) is performed analytically by replacing the sum with an integral, one obtains the exponential dependence of the tension on the excess area

$$\bar{\sigma} \approx \frac{l_{max}^2 + l_{max} - 6e^{2/\tau}}{e^{2/\tau} - 1}. \tag{4.64}$$

For intermediate values of τ in the range $2 \gg \tau \gg 1/\ln l_{max}$, one thus finds

$$\bar{\sigma} \approx l_{max}^2 e^{-2/\tau}. \tag{4.65}$$

The consistency of this approach where the area constraint is treated by a Lagrangean multiplier can be checked by calculating the fluctuations $\delta\Delta$ in the dimensionless excess area defined as

$$\delta\Delta \equiv \frac{(<\Delta^2> - \Delta^2)^{1/2}}{\Delta} = \frac{\tau}{\sqrt{2}} \left(\sum_l \frac{2l+1}{(l^2 + l + \bar{\sigma}(\tau))^2} \right)^{1/2}. \tag{4.66}$$

For this quantity, one obtains in the three regimes

$$\delta\Delta \approx \begin{cases} \sqrt{2/5}, & \tau \ll 1/\ln\, l_{max} \\ \dfrac{\tau}{\sqrt{2N}} e^{1/\tau}, & 1/\ln\, l_{max} \ll \tau \ll 2 \\ \sqrt{2/N}, & 2 \ll \tau \end{cases}, \tag{4.67}$$

where we recall $N \approx l_{max}^2$ for large l_{max}.

Taken at face value, this is a disturbing result. Only for small excess area, the fluctuations show the $\sim 1/\sqrt{N}$ behavior characteristic of large systems. For large and intermediate excess area, the relative area fluctuations are larger and become of order 1 for $\tau \lesssim 1/\ln\ l_{max}$. However, we have seen above that the approach with the effective tension yields the correct result in the limit $\tau \to 0$. The apparent discrepancy arises from the area fluctuations stored in the $l = 2$ modes. If those are neglected by restricting the sum in (4.66) to $l \geq 3$, one obtains, for $\tau \lesssim 1/\ln\ l_{max}$, $\delta\Delta = O(\tau)$, which is consistent with the finding that in the limit $\tau \to 0$ the approach with the effective tension yields the correct result. The fluctuations that lead to $\delta\Delta = O(1)$ are those of the $(l = 2)$-modes for which the approach with the effective tension fails in order T/κ as shown above.

Experimentally, the crucial range is not quite $\tau \to 0$ but rather τ small but finite, say $\tau \simeq 1/\ln\ l_{max}$. In this regime, the relative area fluctuations are of the size $\delta\Delta = O(\tau)$ which may become about 10% for $l_{max} = 1000$. One would expect that the amplitudes of the low lying modes then carry a similar error. How large the error actually is could be determined by calculating the integral (4.50) numerically and then comparing the results with the conventional approach. A first step towards such a comparison for $l_{max} = 20$ has been performed by a Monte Carlo simulation in (Bivas *et al.*, 1992) in a quite narrow τ range. However, one should always keep in mind that neglecting higher order terms in the expansions (4.39)-(4.41) adds additional errors of the order τ. To include those effects would require an expansion in (4.39)-(4.41) beyond the quadratic order (Ou-Yang & Helfrich, 1989). At some point, these tedious calculations have to be done if one wants to extract from the analysis of quasi-spherical vesicle fluctuations both a high precision measurement of the bending rigidity and information as to which variant of the curvature model applies.

4.2.4 Equivalence of all variants in the spherical limit

We finally show that all variants of the curvature model are equivalent in the spherical limit. The other variants differ from the minimal model in the respective energy B, which can be written for the spherical limit in the form

$$B = \kappa G + g(A, M), \tag{4.68}$$

with an obvious $g(A, M)$. The expansion of the mean curvature M in the spherical limit is given by

$$M = R_V \left(4\pi \left(1 + \frac{u_{0,0}}{\sqrt{4\pi}} \right) + \sum_{l \geq 1}^{l_{max}} \sum_{m=-l}^{l} |u_{l,m}|^2 l(l+1)/2 \right)$$

$$= R_V \left(4\pi + \sum_{l\geq 2}^{l_{max}} \sum_{m=-l}^{l} |u_{l,m}|^2 (l+2)(l-1)/2 \right). \tag{4.69}$$

For the latter relation, we fixed $u_{0,0}$ by the volume constraint (4.42). Once this is done, the expansion of the mean curvature turns out to be proportional to the expansion of the area (4.40). This fact lies behind the equivalence of the ensembles in the spherical limit. The expansion of the total energy B now becomes with $A_V \equiv 4\pi R_V^2$ and $M_V \equiv 4\pi R_V$

$$B - 8\pi\kappa - g(A_V, M_V) = \frac{\kappa}{2} \sum_{l\geq 2}^{l_{max}} \sum_{m=-l}^{l} |u_{l,m}|^2 (l+2)(l-1)\left(l(l+1) + \bar{\sigma}_B\right), \tag{4.70}$$

with

$$\bar{\sigma}_B \equiv \frac{R_V^2}{\kappa} \frac{\partial g}{\partial A}|_{(A=A_V, M=M_V)} + \frac{R_V}{\kappa} \frac{\partial g}{\partial M}|_{(A=A_V, M=M_V)}. \tag{4.71}$$

For the calculation of the fluctuations in the spherical limit as in Sect. 4.2.2, the only modification for the other variants will thus be a constant shift in the quantities p_l which will be defined for the other variants by

$$p_l \equiv l(l+1) + \bar{\sigma}_B. \tag{4.72}$$

Such a shift of p_l, however, does not affect the results for the mean square amplitudes. Likewise, in the conventional approach using $\bar{\Sigma}$ to ensure the area constraint, the effective tension in (4.59) will be defined as

$$\bar{\sigma} \equiv \bar{\Sigma} R_V^2/\kappa + \bar{\sigma}_B. \tag{4.73}$$

Since the Lagrange multiplier $\bar{\Sigma}$ has no independent physical significance in this approach and the amplitudes depend only on the effective tension $\bar{\sigma}$, the details of the variant of the curvature model do not effect any the results. This fact has a merit and a drawback. The merit is that the fluctuations of quasi-spherical vesicles are universal in the sense that they depend only in the local bending rigidity, the temperature and the excess area which should make the analysis of experimental data simpler. On the other hand, this universality shows that one can not expect to decide on a specific variant of the curvature model on the basis of the conventional analysis of quasi-spherical fluctuations. This universality has independently been shown within the ADE model in (Yeung, 1994).

Chapter 5

Vesicles of non–spherical topology

Topology has not yet played any role in this investigation since as argued in the introduction, topological changes seem not to occur on the experimentally accessible time-scales. Still, vesicles of non-spherical topology do exist if the bilayer sheet closes in this topology during the poorly understood swelling process. In fact, shapes of vesicles of toroidal topology have been predicted theoretically (Ou-Yang, 1990; Seifert, 1990; Seifert, 1991c) and, at the same time, toroidal vesicles have been found independently in experiments (Mutz & Bensimon, 1991). While one may first suppose that the different topology does not play any significant role, quite the contrary is true. For vesicles with more than one handle or hole, i.e. for genus $g \geq 2$, the ground state can be degenerate. The reason for this degeneracy is the conformal invariance of the curvature energy, which has non-trivial consequences only for $g \geq 2$, even though this invariance is a general property that is not restricted to any topology. Based on this invariance, it was theoretically predicted (Jülicher *et al.*, 1993a) that these vesicles should exhibit a novel diffusion process in shape space called conformal diffusion for which, recently, very strong evidence was experimentally found, indeed (Michalet, 1994).

The first three sections of this chapter are devoted to the mathematical notions that are used for the theoretical description of these phenomena. In Sect. 5.1, we discuss conformal invariance of the curvature energy. In Sect. 5.2, Willmore surfaces and the Willmore problem are defined and discussed for each topological class. The role of the geometrical constraints under conformal transformations is derived in Sect. 5.3.

Based on these concepts, in Sects. 5.4 through 5.6, we present the theoretical predictions for vesicles of genus 1, genus 2, and higher genus, respectively. Each of these sections closes with a discussion of the experimental data available at present.

5.1 Conformal invariance of the local curvature energy

The central concept necessary for understanding the new features of vesicles of non-spherical topology is the conformal invariance of the local curvature energy G (2.51), which is a stronger property than the scale invariance referred to in Sect. 2.6.2.[1] The conformal transformations in three dimensions comprise a ten parameter group. It consists of translations (three parameters), rotations (three parameters) and scale transformations (one parameter), all of which do not change the shape in any non-trivial fashion. The non-trivial conformal transformations are the inversions in a sphere which map $\mathbf{R}$ to $\mathbf{R}'$ with

$$\mathbf{R}' = \mathbf{R}_0 + (\mathbf{R} - \mathbf{R}_0)/(\mathbf{R} - \mathbf{R}_0)^2. \tag{5.1}$$

The center $\mathbf{R}_0$ of the sphere yields the remaining three parameters. The local quantity $(H^2 - K)dA$ is invariant under conformal transformation in three dimensions as can be shown by inserting the mapping (5.1) (for $\mathbf{R}_0 = \mathbf{0}$) into the expression given in Sect. 2.1 for H, K and dA, respectively. Since the topology of a closed surface and thus of $\oint dA\ K$ does not change under a conformal transformation, the energy G is, in fact, a conformal invariant.

Rather than using inversions, it is more convenient for many applications to work with special conformal transformations. Such a transformation consists of an inversion at a unit sphere in the center of origin $\mathbf{R} \rightarrow \mathbf{R}/R^2$, a translation by a vector a and another inversion at a unit sphere in the center of origin. Every point $\mathbf{R}$ is thus transformed to $\mathbf{R}'$, with

$$\mathbf{R}' = \frac{\mathbf{R}/R^2 + \mathbf{a}}{(\mathbf{R}/R^2 + \mathbf{a})^2} \quad . \tag{5.2}$$

Two successive special conformal transformations (5.2) with translation vectors $\mathbf{a}_1$ and $\mathbf{a}_2$ are equivalent to one special conformal transformation with $\mathbf{a} = \mathbf{a}_1 + \mathbf{a}_2$, i.e., the special conformal transformations form a commutative three parameter subgroup. Since for $\mathbf{a} \rightarrow \mathbf{0}$, the special conformal transformation becomes the identity, an expansion in a is feasible, which is the main advantage of using special conformal transformations.

5.2 Willmore surfaces and Willmore problem

Willmore surfaces are defined as the stationary points of the curvature energy G, i.e., a shape is a Willmore surface if it obeys $\delta^1 G = 0$ (Willmore, 1982; Pinkall & Sterling, 1987). If the surface is free of self-intersections, it is called embedded. The Willmore problem consists in

[1] The conformal invariance of G has been known to mathematicians for a long time (Thomsen, 1924). In the context of vesicles, it was recalled in (Duplantier, 1990; Duplantier *et al.*, 1990).

finding the Willmore surface $\mathcal{S}_g$ of lowest energy G for any given genus g irrespective of any further constraints, i.e., in finding the absolute minimum of G for given topology (Willmore, 1965; Willmore, 1982). For any shape $\mathcal{S}_g$ that is a solution to this problem, all conformal transformations of $\mathcal{S}_g$ are solutions, too.

5.2.1 Genus 0

For spherical topology, one can prove that the sphere with $G \equiv G_0 = 8\pi$ is the only embedded Willmore surface (Bryant, 1984). Since spheres remain spheres under conformal transformations, the Willmore problem has a unique solution for spherical topology.

5.2.2 Genus 1

For toroidal topology, there is no definite answer to the Willmore problem yet. Willmore himself conjectured that the Clifford torus shown in Fig. 5.1 minimizes G (Willmore, 1965; Willmore, 1982). The Clifford torus is an axisymmetric torus, which can be parametrized by

$$\mathbf{R}(\theta,\phi) = \begin{pmatrix} (\sqrt{2}+\sin\theta)\cos\phi \\ (\sqrt{2}+\sin\theta)\sin\phi \\ \cos\theta \end{pmatrix}, \tag{5.3}$$

where $0 \le \theta, \phi \le 2\pi$. Its curvature energy is $G = G_1 \equiv (\pi/2)8\pi$ and its reduced volume is $v_{cl} \equiv 3/(2^{5/4}\pi^{1/2}) \simeq 0.71$. Among the evidence for Willmore's conjecture is the fact that the Clifford torus is proven to be the shape of lowest G among all axisymmetric tori (Langer & Singer, 1984).

Conformal transformations of the Clifford torus generate a *one*-parameter family of non-axisymmetric shapes. This can be seen by applying a special conformal transformation (5.2) to the Clifford torus as given by (5.3); see Fig. 5.1 for an example. A special conformal transformation with vector $\mathbf{a}(s) = (s\cos\phi, s\sin\phi, 0)$ generates a one-parameter family of non-axisymmetric shapes with varying reduced volume $v_{cl} \le v(s) < 1$. This family of shapes can be described in a closed analytical form (Fourcade, 1992). For $s = 2^{1/4}\pi^{1/2}/(2^{1/2}+1)$, it ends up at a limit shape with $v = 1$, which consists of a sphere with an infinitesimal handle.

A special conformal transformation with $\mathbf{a} = (0, 0, a_Z)$ applied to the Clifford torus, does not generate any new shape but is rather equivalent to a scale-transformation due to the special ratio $\sqrt{2}$ of the generating radii of the Clifford torus. In contrast, for a general axisymmetric toroidal shape with a reflection plane, a conformal transformation (5.2) with $\mathbf{a} = (0, 0, a_Z)$ would generate a shape with broken up-down symmetry. Thus, even though the special conformal transformations involve the three parameters (a_X, a_Y, a_Z), there is only

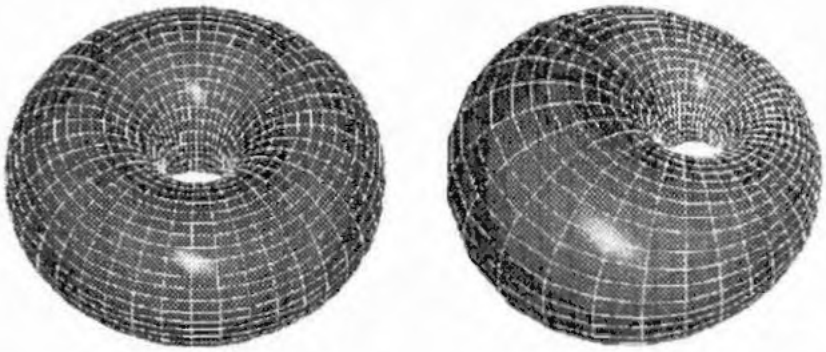

Figure 5.1: Clifford torus and a shape generated by a conformal transformation. (Jülicher *et al.*, 1993b).

a one-parameter family of special conformal transformations which produces new shapes when applied to the Clifford torus due to its special symmetry properties.

Apart from the Clifford torus, there are further embedded Willmore surface but those turn out to be *unstable* stationary points of the functional G (Pinkall, 1985; Kusner, 1994).

5.2.3 Genus 2

For genus 2, the Willmore problem is solved tentatively by Kusner's conjecture (Kusner, 1989), that the so-called Lawson surface shown in Fig. 5.2 is the shape of minimal curvature energy. The rational behind Kusner's conjecture arises from a connection between minimal surfaces in S^3, which is the three-dimensional unit sphere in R^4, and Willmore surfaces in R^3: Any compact minimal surface in S^3 becomes a Willmore surface when projected stereographically from S^3 to R^3. The value of the curvature energy G is twice the respective area in S^3 (Pinkall & Sterling, 1987). The reverse does not hold: A Willmore surface in R^3 does not need to be a minimal surface in S^3.

Lawson has found a whole family $\xi_{m,k}$ (with $m \geq k \geq 0$ and genus $g = mk$) of minimal surfaces in S^3 by first solving Plateau's problem for a certain geodesic quadrilateral in S^3 (Lawson, 1970). If the resulting surface is extended by reflections across its geodesic boundary arcs, a compact minimal surface $\xi_{m,k}$ in S^3 is obtained, which after projection to R^3 yields a Willmore surface also called $\xi_{m,k}$. The Clifford torus is the particular member $\xi_{1,1}$ while all $\xi_{m,0}$ correspond to a sphere. The Lawson surface as shown in Fig. 5.2 is the

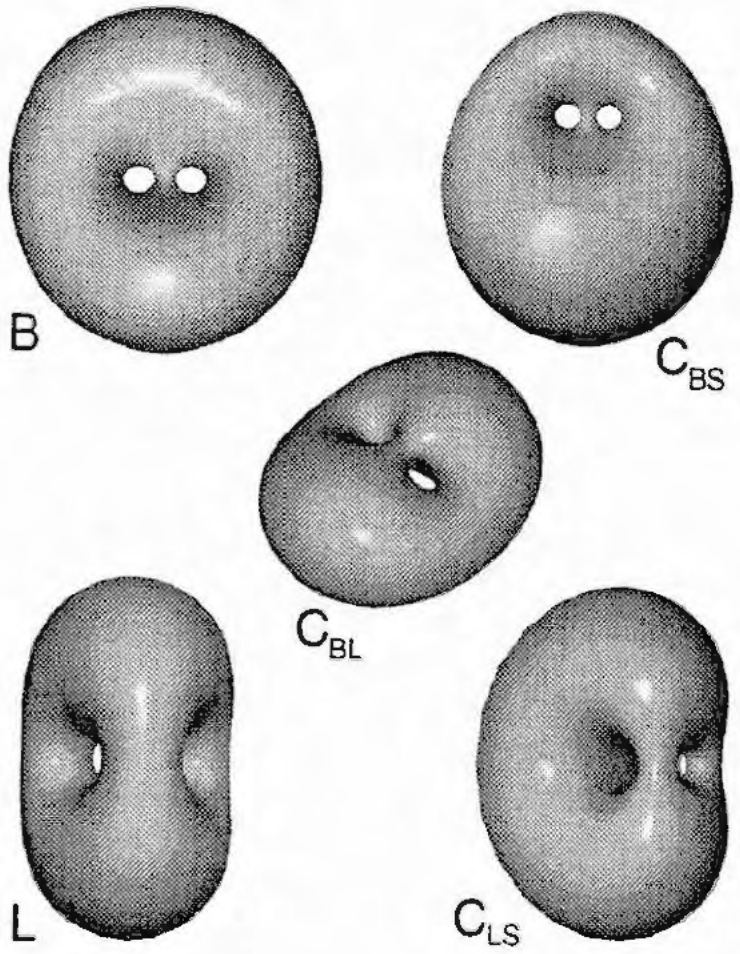

Figure 5.2: Lawson surface (L) and some shapes obtained by conformal transformations including the "button" surface (B). The other labels refer to the phase diagram Fig. 5.7. (Jülicher *et al.*, 1993a).

member $\xi_{2,1}$, which has been shown to have a quite small area in S^3 and which is thus a good candidate for Willmore's problem (Kusner, 1989).

In general, there is no analytical description known for the minimal surfaces $\xi_{m,k}$ in S^3 and thus no explicit representation of the corresponding surface in R^3. However, there are surfaces $\Xi_{m,k}$ in S^3 which can be considered as approximations to these minimal surfaces since they contain the same geodesic arcs. The surfaces $\Xi_{m,k}$ are defined by (Lawson, 1970)

$$\mathcal{I}m(z^{m+1}) + |w|^{m-k}\mathcal{I}m(w^{k+1}) = 0, \tag{5.4}$$

using the representation $S^3 = \{(z,w), |z|^2 + |w|^2 = 1\}$ and z, w complex numbers.

The Lawson surface as it is shown in Fig. 5.2 was obtained by first mapping the surface

$\Xi_{2,1}$ from S^3 to R^3 by a stereographic projection. The resulting shape was then triangulated and used as an initial shape for a further numerical minimization of G by an algorithm described in (Schnitzler, 1993). The shape thus obtained should be a close approximation to the Lawson surface. In fact, this algorithm yields the energy $G = G_2 \simeq 1.75 \times 8\pi$ thus corroborating the result obtained in (Hsu *et al.*, 1992), where a different algorithm described in (Brakke, 1992) was used.

The Lawson surface has a threefold symmetry axis and a mirror symmetry plane perpendicular to this axes. Moreover it is invariant under inversions in the center. The conformal transformations of the Lawson surface comprise a three parameter family of shapes. This family can be parametrized by the vector a of the special conformal transformation which must be applied to the Lawson surface (centered in the origin) in order to generate this specific shape. The topology of this space $\mathcal{W}$ of shapes is that of the Lawson surface itself since whenever the vector a approaches the Lawson surface the resulting shape becomes a sphere with two infinitesimal handles (Jülicher, 1993). Whenever the vector a of the special conformal transformation applied to the Lawson surface points along an axis of high symmetry, the resulting shape has higher symmetry, too. Some of these shapes are shown in Fig. 5.2. In general, a conformal transformation of the Lawson surface has no obvious symmetry left. Again, there exist other embedded Willmore surfaces but so far no stable ones are known (Kusner, 1994).

5.2.4 Genus ≥ 3

For higher genus, little is known about the solution of Willmore's problem. Supported so far by limited numerical results (Hsu *et al.*, 1992), Kusner's conjecture states that the global minimizer for G is given by the stereographic projection of the shape $\xi_{g,1}$ from S^3 to R^3 (Kusner, 1989).

As an exact result, a strict upper bound to the minimal energy, $G_g < 16\pi$, can be proven for any genus (Kusner, 1989). An informal motivation for this result follows from considering two concentric spheres connected by narrow necks. The two spheres contribute an energy 16π while the necks can be made of catenoids, which are minimal surfaces with no energy. The subtlety, of course, lies in the appropriate matching of the necks with the spheres in such a way that $G_g < 16\pi$.

For $g \geq 3$, besides $\xi_{3,1}$ further locally stable embedded Willmore surfaces are known (Karcher *et al.*, 1988; Hsu *et al.*, 1992).

5.2.5 An aside: energy of handles

The solutions, or more precisely conjectures, on Willmore's problem can be used to comment on the energy of handles. In the limit $v \to 1$, the conformal transformation of the Clifford torus becomes a sphere with a small handle attached to it. One obtains thus the minimal energy of a handle, G_h, as $G_h = G_1 - G_0 = (\pi/2 - 1)8\pi$ (Seifert, 1991c).

Likewise, in the limit $v \to 1$, which can be approached along various paths, the conformal transformation of the Lawson surface always becomes a sphere with two handles close together. The energy "stored" in the two handles, $G_2 - G_0 \simeq 0.75 \times 8\pi$, is less than the energy $2G_h$ of two independent handles. Thus, the two handles obtained in this way "interact" and lower their energy. A similar statement holds for n handles whose energy can be bounded by $G_n - 8\pi \leq 8\pi$ for optimal interaction.

5.3 Constraints and conformal invariance

The mathematical results described above cannot immediately be carried over to real vesicles since those are determined not only by the minimum of G but also by additional contributions to the energy, such as the area-difference elasticity, as well as by the geometrical constraints. Neither the area, nor the volume and the mean curvature are conformal invariants.

5.3.1 Expansion for special conformal transformations

The effect of special conformal transformations on the geometrical quantities A, V and M can be worked out analytically for small $|\mathbf{a}| \ll 1$ (Seifert, 1991b). A special conformal transformation acting on a surface $\mathcal{S}$ with initial values $V = V_1$, $A = A_1$, and $M = M_1$ generates a new shape with

$$A(\mathbf{a}) = A_1(1 - 4\mathbf{R}^A \cdot \mathbf{a} + O(\mathbf{a}^2)), \tag{5.5}$$

$$V(\mathbf{a}) = V_1(1 - 6\mathbf{R}^V \cdot \mathbf{a} + O(\mathbf{a}^2)), \tag{5.6}$$

and

$$M(\mathbf{a}) = M_1(1 - 2\mathbf{R}^M \cdot \mathbf{a} + O(\mathbf{a}^2)). \tag{5.7}$$

Here, $\mathbf{R}^A \equiv (\oint dA\mathbf{R})/A$ is the center of area, $\mathbf{R}^V \equiv (\int dV\mathbf{R})/V$ is the center of volume and $\mathbf{R}^M \equiv (\oint dAH\mathbf{R})/M$ is the center of mean curvature.

From the expressions (5.5) to (5.7), one derives for the reduced variables, the quite similar relations

$$v(\mathbf{a}) = v_1(1 + 6(\mathbf{R}^A - \mathbf{R}^V)) \cdot \mathbf{a} + O(\mathbf{a}^2)) \tag{5.8}$$

and

$$m(\mathbf{a}) = m_1(1 + 2(\mathbf{R}^A - \mathbf{R}^M) \cdot \mathbf{a} + O(\mathbf{a}^2)). \tag{5.9}$$

The terms of order $\mathbf{a}^2$ are given explicitly for axisymmetric shapes in (Seifert, 1991b).

5.3.2 Symmetry of stationary shapes

For small $\mathbf{a}$, a special conformal transformation induces a first variation of the shape under which the functional Φ (2.57) should be invariant for any stationary shape. This condition together with the small $\mathbf{a}$ expansion given above implies a surprising symmetry property of any stationary shape. If the terms linear in $\mathbf{a}$ from the expansions (5.5) to (5.7) are inserted as first variation into the general stationarity condition (2.58), one immediately gets the relation

$$2\Sigma A\mathbf{R}^A + 3PV\mathbf{R}^V + QM\mathbf{R}^M = 0, \tag{5.10}$$

which has to hold for any stationary shape of the functional Φ. This relation is the conformal equivalent to the homogeneity relation (2.66) derived from the scale invariance of G. The homogeneity relation can, in fact, be used to eliminate one Lagrangean multiplier in (5.10) in favor of the other two. One thus obtains (Seifert, 1991b)

$$3PV(\mathbf{R}^V - \mathbf{R}^A) + QM(\mathbf{R}^M - \mathbf{R}^A) = 0, \tag{5.11}$$

which shows that one of the following two propositions holds true for any stationary shape of Φ. (i) The end points of the three vectors $\mathbf{R}^A$, $\mathbf{R}^V$, and $\mathbf{R}^M$ are collinear; or (ii) $\Sigma = P = Q = 0$, i.e. the shape is a Willmore surface and thus a stationary shape of G.

Since there are no other Willmore surfaces of spherical topology besides the sphere, the first proposition has to hold for any other stationary shape of spherical topology. By symmetry, collinearity holds for all shapes which have at least an n-fold axis of symmetry and thus, in particular, for axisymmetric shapes and for ellipsoids. Consequently, one expects that the ground state for those cases in any of the curvature models has generically at least a n-fold axis and one can thus exclude whole classes of shapes as candidates for the ground state just by symmetry (Seifert, 1991b). There is a caveat to this statement since it is conceivable that there are shapes without symmetry but which still have the property that the end points of the three vectors are collinear. Generically, however, shapes without this minimal symmetry are not stationary and, in fact, no stationary shapes with less than a two-fold axis of symmetry has yet been found for spherical topology.

5.3.3 Stability with respect to special conformal transformations

Special conformal transformations can be used to derive a necessary (but, in general, not sufficient) criterion for stability of a stationary shape (Seifert, 1991b). The idea is to apply a special conformal transformation to a stationary shape and then to compare the energy of the shape thus obtained with the energy of a stationary shape on the same branch at the same reduced volume and mean curvature m, (or m_0 in the ADE model.) This criterion, which can be formulated in terms of the second order expressions of (5.8) and (5.9), is easy to check for axisymmetric shapes by a simple numerical integration of geometrical quantities over the contour.

With this technique, the stability of the prolates and the oblates with respect to a symmetry breaking deformation towards pears and the stomatocytes, respectively, has been checked (Seifert, 1991b). Surprisingly, within a large region of parameters, the instability obtained in this way is extremely close to the "true" instability as found by solving the shape equations for the pears and the stomatocytes directly. This result indicates that the special conformal transformations are a very good approximation to the true unstable mode. This positive result encourages the use of special conformal transformations for an efficient approximate stability analysis with respect to breaking the axisymmetry. The implicit assumptions, however, are (i) that the symmetry of the instability is accessible by a special conformal transformation[2] and (ii) that the true instability and the one with respect to special conformal transformations are still close together for cases for which an independent check has not yet been performed.

5.4 Shapes and phase diagrams for genus 1

5.4.1 Phase diagrams

The phase diagrams for vesicles of toroidal topology have been investigated theoretically by a combination of two techniques. First, the axisymmetric stationary shapes have been determined by solving the appropriate shape equations (Seifert, 1990; Seifert, 1991c; Jülicher *et al.*, 1993b). The solutions to these coupled nonlinear differential equations are a discrete set of sheets. Secondly, the stability of the axisymmetric shapes of lowest energy with respect to special conformal transformations is investigated.

Three different sheets of axisymmetric shapes can be distinguished which are illustrated by both their energy G and their cross section in Fig. 5.3, for fixed $v = 0.55$: (i) the sheet of

[2]An example for an instability which can not be accessed by special conformal transformations is the breaking of the axisymmetry of prolates and oblates towards non-axisymmetric ellipsoids (Seifert, 1991b).

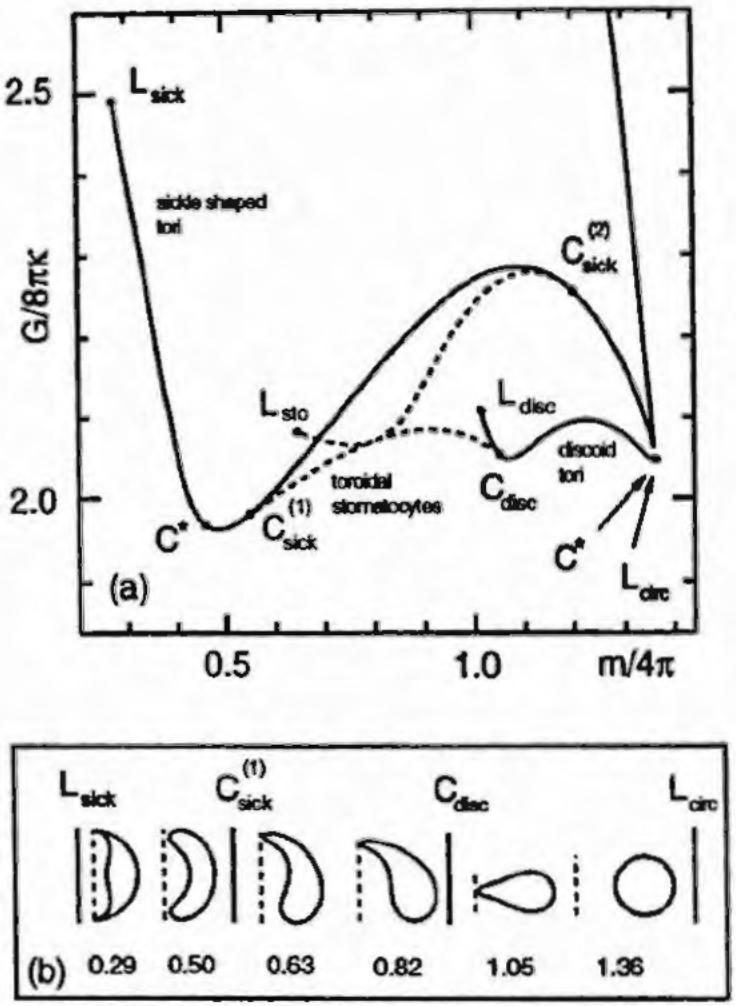

Figure 5.3: (a) Energy G of the axisymmetric stationary shapes in the BC model versus the total mean curvature m for fixed reduced volume $v = 0.55$. Three different branches can be distinguished: (i) a branch of discoid tori, (ii) a branch of sickle–shaped tori and (iii) a branch of toroidal stomatocytes. The toroidal stomatocytes bifurcate from the other branches at the points $C^{(1)}_{sick}$, $C^{(2)}_{sick}$ and C_{disc}. All three branches end at different types of limit shapes. L_{sick}, L_{sto} and L_{disc} are limit shapes with a vanishing hole diameter. At L_{circ}, a limit shape with perfectly circular cross section is reached. Some parts of these axisymmetric branches are unstable with respect to symmetry breaking conformal transformations. These instabilities occur at the points C^*. (b) Sequence of axisymmetric shapes of minimal energy G for fixed reduced volume $v = 0.55$ and several values of m. The first and the last shape are unstable with respect to non–axisymmetric deformations. (Jülicher *et al.*, 1993b).

sickle–shaped tori, (ii) the sheet of discoid tori, and (iii) the sheet of toroidal stomatocytes, which do not have a symmetry plane perpendicular to the symmetry axis. Both the discoid

tori and the sickle–shaped tori have reflection symmetry. They can be distinguished from each other as different sheets since they are separated, except for one shape which is that of the Clifford torus. Therefore, starting with the Clifford torus, which has an exactly circular cross section, the two different ellipsoidal deformations of the contour lead to the sheets of discoide and sickle–shaped tori. The sheet of toroidal stomatocytes bifurcates from the sheet of sickle–shaped tori and from the sheet of discoide tori, thus connecting these two sheets.

Various types of limit shapes, where the sheets end and the shape becomes singular, can be distinguished. For all three sheets, one class of limit shapes occurs where the hole diameter vanishes. Formally, these shapes represent a connection to the spherical topology and are denoted by L_{sick}, L_{disc} and L_{sto}. Other classes of limit shapes include tori with exactly circular cross section L_{circ} and shapes with diverging hole diameter. A detailed discussion of the limit shapes is given in Appendix B of (Jülicher *et al.*, 1993b).

In a second step, the stability of these shapes with respect to special conformal transformations is checked (Jülicher *et al.*, 1993b). If, for a given set of parameters, the axisymmetric shape of minimal energy is found to be unstable, the ground state must be non-axisymmetric for these parameters. Even though one cannot expect to obtain the region of the non-axisymmetric ground states exactly, this method gives at least a lower bound on the extension of this region. This lower bound should be a reasonable approximation since (i) it becomes exact in the neighborhood of the Clifford torus, and (ii) the same approximation works excellently for the prolate/pear and oblate/stomatocyte bifurcation for vesicles of spherical topology as mentioned above. The phase diagram obtained in this way within the BC model, the ADE model for $\alpha = 1$, and the SC model are shown in Figs. 5.4, 5.5, and 5.6, respectively.

Common to all phase diagrams is the large region of non-axisymmetric shapes which are separated from the axisymmetric shapes by the instability line C^*. This large region is reminiscent of the degeneracy of the Willmore problem since in the BC model, in particular, the conformal transformations of the Clifford torus lie along a curve from the Clifford torus to the sphere. For m slightly above or below this curve, the ground state is, of course, still non–axisymmetric. Again, there are no discontinuous transitions for the BC model. For toroidal topology, the phase diagram for the ADE model at $\alpha = 1$ resembles more the BC than the SC phase diagram in contrast to what we observed for the budding transition for spherical topology. In particular, the toroidal stomatocytes do not show up in the phase diagram for the SC model, whereas they occupy a small region for the BC model as well as for the ADE model.

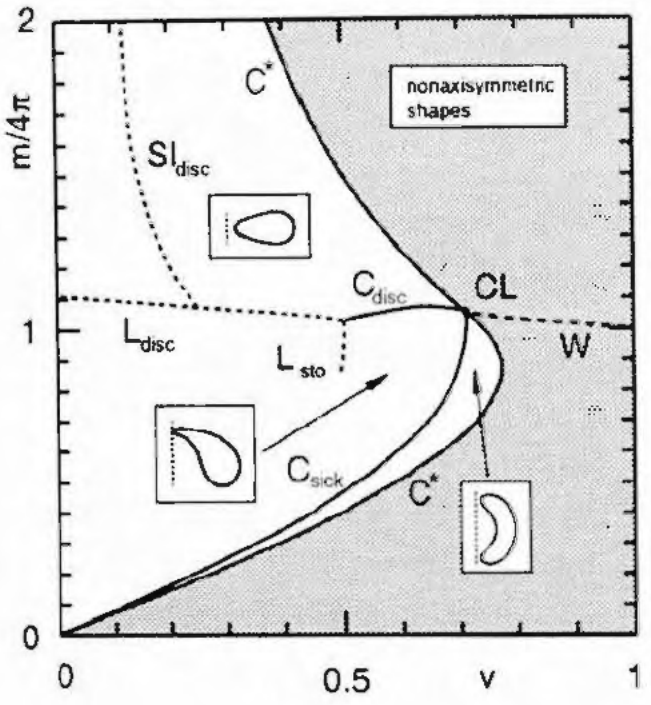

Figure 5.4: Phase diagram for toroidal vesicles in the BC model. Three axisymmetric regions, which are separated by continuous shape transformation lines C_{sick} and C_{disc}, can be distinguished: (i) discoid tori, (ii) sickle-shaped tori and (iii) toroidal stomatocytes. The line C^* indicates the instability with respect to axisymmetry breaking conformal transformations. On the right hand side of this line, non-axisymmetric shapes have minimal energy. Along the dashed line W, conformal transformations of the Clifford torus connect the Clifford torus with the sphere. The lines L_{disc} and L_{sto} represent limit shapes with vanishing hole diameter. The contour of discoid tori begins to self-intersect at the line SI_{disc}. (Jülicher *et al.*, 1993b).

5.4.2 Experiments

All classes of shapes predicted by the theoretical work except for the sickled-shaped tori have been found in experiments. The first observations of toroidal shapes reported mainly Clifford tori (Mutz & Bensimon, 1991). In this case, however, the membrane was partially polymerized, which should become a relevant perturbation of the fluid membrane considered here at least beyond the percolation threshold. In a subsequent study (Fourcade *et al.*, 1992),

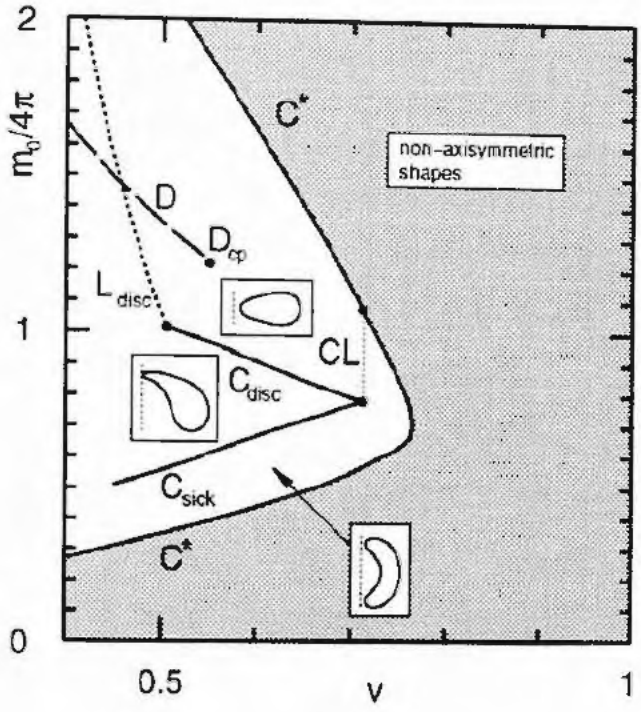

Figure 5.5: Phase diagram for toroidal vesicles in the ADE model with $\alpha = 1$. The phase diagram is similar to that of the BC model shown in Fig. 5.4. Three axisymmetric regions which are separated by continuous shape transformation lines C_{sick} and C_{disc} can be distinguished: (i) discoid tori, (ii) sickle-shaped tori and (iii) toroidal stomatocytes. The line L_{disc} represent limit shapes with vanishing hole diameter. The instability with respect to axisymmetry breaking conformal transformations is denoted by C^*. Within the region of axisymmetric shapes with reflection plane, discontinuous shape transformations from circular tori to discoid tori occur along the line D. This line ends up in a critical point D_{cp}. The Clifford torus is the shape of minimal energy along the dotted line CL. (Jülicher *et al.*, 1993b).

shapes of quasi-circular cross-section, which theoretically belong to the discoid sheet, have been found, as well as non-axisymmetric shapes which resemble conformal transformations of the Clifford torus (see the experimental Fig. 1.4). In a comprehensive work, (Michalet, 1994) reports the existence of (i) tori with quasi-circular cross section for a volume range $0.3 \lesssim v \lesssim v_{cl}$, (ii) non-axisymmetric shapes resembling conformal transformations of the Clifford torus in the range $v_{cl} \lesssim v \lesssim 0.92$, (iii) discoid tori with and without axisymmetry and (iv) non-axisymmetric toroidal stomatocytes.

These observations can be related to the theoretical predictions as follows. The quasi-

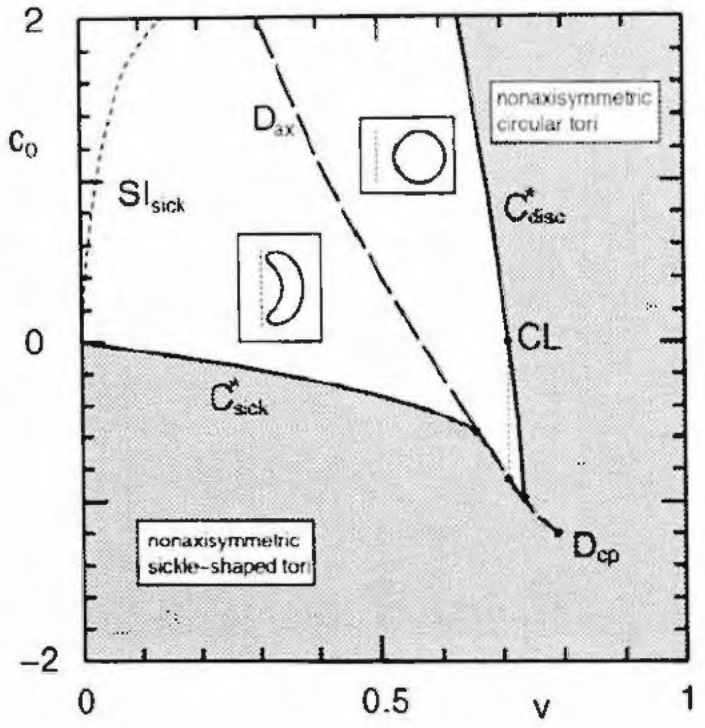

Figure 5.6: Phase diagram for toroidal vesicles in the SC model. The two model parameters are the reduced volume v and the reduced spontaneous curvature c_0. The line D_{ax} which ends in the critical point D_{cp}, represents the line of discontinuous shape transformations. It separates a region of circular tori from a region of sickle-shaped tori. At the dotted line SI_{sick}, the sickle-shaped tori self-intersect. The two dashed lines C^*_{sick} and C^*_{disc} represent lines of instability of axisymmetric shapes with respect to symmetry breaking conformal transformations. They serve as approximations for the exact continuous shape transformations of axisymmetry breaking. Two different types of non-axisymmetric shapes can be distinguished: (i) non-axisymmetric sickle-shaped tori and (ii) non-axisymmetric circular tori. For $c_0 = 0$, the Clifford torus (CL) appears in the phase diagram on the line C^*_{disc}. The Clifford torus is the minimal energy shape along the dotted line with $v = v_{cl}$. (Jülicher *et al.*, 1993b).

circular shapes as well as the non-axisymmetric shapes are indeed ground state for all variants of the curvature models for a large range of parameters. Michalet reports that the breaking of the axisymmetry takes place close to $v \sim v_{cl}$ which would favor the SC model since there the instability line is quite steep as a function of v (see Fig. 5.6). The experimental observation of discoid tori and toroidal stomatocytes, on the other hand, could rule out the SC model since these shapes do not occur as ground states. However, they do occur as metastable states, and one has to be careful with discarding a model simply on the basis

that an observed shape does not occur as ground state.

At present, there remains a disturbing experimental observation which claims the occurrence of non-axisymmetric toroidal stomatocytes (Michalet, 1994). This observation is in discrepancy with theoretical work for two reasons. First, the axisymmetric toroidal shapes from which such a shape would have to bifurcate are all stable with respect to special conformal transformations. Secondly, as discussed in Sect. 5.3.2, the occurrence of such shapes with only one symmetry plane as ground state (or even metastable state) can be expected to indicate, generically, that the corresponding shape is a Willmore surface for which there is neither theoretical nor experimental evidence.

In summary, even though it is too early to decide on a particular variant of the curvature model on the basis of the experiments on genus 1 vesicles, Michalet's comprehensive study demonstrates the potential of a detailed comparison between theory and experiment.

5.5 Shapes and phase diagram for genus 2

5.5.1 Conformal diffusion

The threefold degeneracy for the Willmore problem for genus 2 has profound consequences for the phase diagram which becomes qualitatively different from the phase diagram for spherical or toroidal topology (Jülicher *et al.*, 1993a). The new features are most easily described within the BC model.

The three-dimensional space $\mathcal{W}$ of conformal transformations of the Lawson surface can be projected onto the two-dimensional (v, m)-plane. This leads to a region W in the phase diagram where the ground state is one-dimensional degenerate as shown in Fig. 5.7. A quantitative expression for the conformal mode which corresponds to this degeneracy can be obtained from the expressions (5.8) and (5.9) for special conformal transformations with small a. Thus, the conformal mode that conserves both v and m can be identified as the special conformal transformation with a obeying the differential equation (Jülicher *et al.*, 1993a)

$$d\mathbf{a}/ds = (\mathbf{R}^A - \mathbf{R}^V) \times (\mathbf{R}^A - \mathbf{R}^M) \tag{5.12}$$

where s parametrizes the path in the space $\mathcal{W}$. In general, the conformal mode $\mathbf{a}(s)$ that solves (5.12) destroys all symmetry planes of the shapes in the region W. However, along the path $\mathbf{a}(s)$ which is a closed loop within $\mathcal{W}$, there are two different shapes which have one symmetry plane left. These shapes are shown in Fig. 5.8 for the conformal mode with $(v, m) = (0.78, 1.027)$ as they have been obtained by numerical integration of (5.12) (Jülicher *et al.*, 1993a).

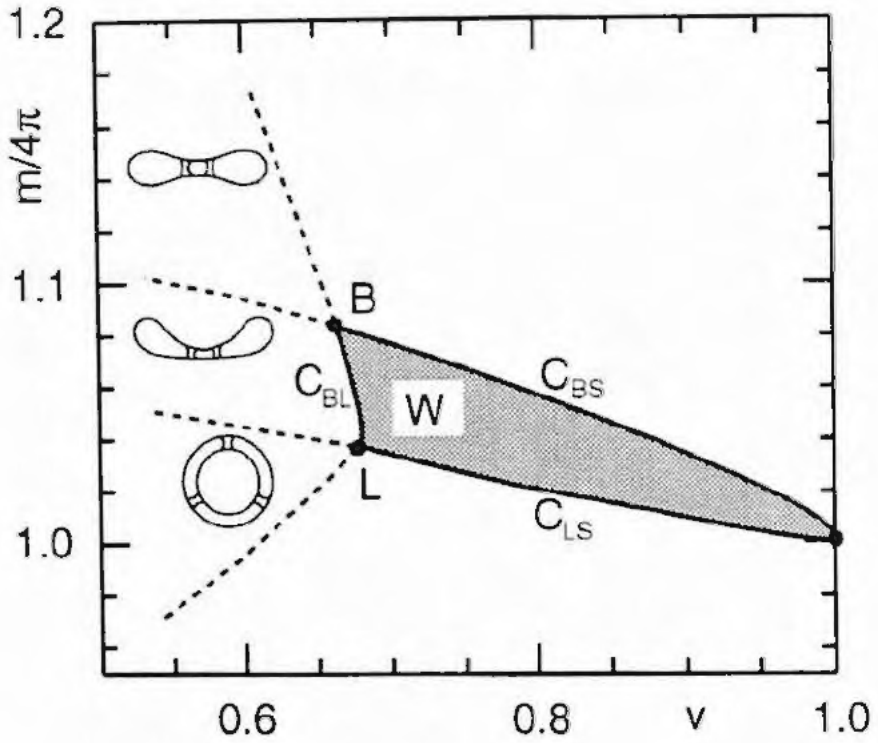

Figure 5.7: Phase diagram for genus 2 in the BC model. The letters along the boundary of the region of conformal degeneracy refer to the shapes shown in Fig.5.2. (Jülicher *et al.*, 1993a).

The boundary of the region W in the phase diagram is obtained by mapping out the conformal transformations of the Lawson surface along the high symmetry directions. There is one special shape with high symmetry on this boundary, which is called the Button surface also shown in Fig. 5.2. It has three orthogonal mirror symmetry planes and inversion symmetry. The shapes along C_{BS}, C_{BL}, and C_{LS} as shown in Fig. 5.2 constitute the boundary of the region W since these shapes have at least two mirror-planes, which implies that $\mathbf{R}^A, \mathbf{R}^V$ and $\mathbf{R}^M$ are collinear and there is no conformal mode left, as can be seen from (5.12).

The existence of the phase W persists in the ADE model for arbitrary $\alpha > 0$. Whenever m_0 lies in the range of m-values which span the phase W at constant v, the area-difference-elasticity is zero and the ground state in the ADE model also shows this one-fold conformal degeneracy.

The degeneracy of the ground state in the phase W should have observable consequences

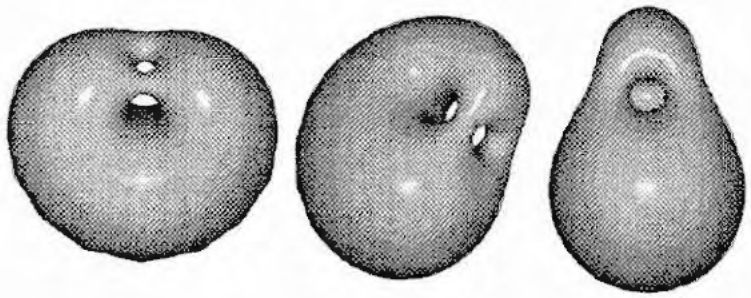

Figure 5.8: Shapes along a trajectory of conformal diffusion. All shapes have the same area, volume and integrated mean curvature. (Jülicher *et al.*, 1993a)

whenever a vesicle v and m_0 belong to this phase. Because of thermal excitation its shape will permanently change within a diffusion process along the conformal trajectory. In analogy to rotational and translational diffusion, this phenomenon has been called conformal diffusion (Jülicher *et al.*, 1993a).

The experimental verification of conformal diffusion would thus yield strong support for the energy G as the appropriate energy for vesicles. However, its manifestation would not directly confirm the ADE term since any energy B which can be written in the form (2.60) leads to this degeneracy for those parameters for which $\partial g/\partial A = \partial g/\partial V = \partial g/\partial M = 0$. Note that for the SC model $\partial g/\partial M = -2C_0$ and, thus, there is no conformal diffusion in this variant for $C_0 \neq 0$.

From a theoretical point of view, there are two caveats to the prediction of conformal diffusion. First, there definitely will be correction terms to the energy W of the order of $O(d/R)$. Those terms, however, are much smaller than the thermal energy and will therefore not be strong enough to prevent this phenomenon from happening. Another objection could result from the breaking of conformal invariance due to fluctuations. In a related context, it is known that scale invariance of the local curvature energy is broken by fluctuations, which leads to a length-scale dependent renormalization of the bending rigidity (2.18). In a similar fashion, conformal invariance may also be broken by fluctuations. How relevant such an effect is compared with the thermal energy available for overcoming small perturbations remains to be investigated.

5.5.2 Phase diagram beyond the conformal phase

Outside of the degenerate conformal phase W, the shapes of minimal energy are no longer Willmore surfaces with constant energy $G = G_2$, but rather unique shapes with an energy $G = G(v, m) > G_2$, which can also be classified by their symmetry properties (Jülicher *et al.*, 1993a). The topology of the phase diagram beyond W can be deduced by extending the symmetry of the shapes along the boundary of W as shown in Fig. 5.7. The phases thus obtained are in accordance with the rule of collinearity discussed in Sect. 5.3.2. They can all be separated by continuous transitions according to the expectation that in the BC model all transitions are indeed continuous. Neither the precise location of these transitions in the BC model is known, nor do we know at present whether some of these transitions are preempted by first order transitions for the ADE model as one could expect for small enough α. The shapes and shape transitions outside of W could be calculated with a numerical minimization of triangulated surfaces taking into account the appropriate constraints but this has not yet been done comprehensively.

It is instructive to note the similarity of the phase diagram for genus–2 with the one for genus–1 as shown in Fig. 5.4. The three axisymmetric families of genus–1 shapes, the discoid tori, toroidal stomatocytes and the sickle–shapes tori, correspond to the three phases on the left side of W. The corresponding shapes indeed look very similar, even though the additional hole of the genus–2 shapes necessarily breaks the axisymmetry. Likewise, the line W of genus–1 Willmore tori in Fig. 5.4 corresponds to the region W for genus-2 vesicles in Fig. 5.7.

5.5.3 Experiments

The first experimental observation of genus–2 vesicles reported a shape very similar to the button surface shown in Fig. 5.2 (Fourcade *et al.*, 1992). In a comprehensive study (Michalet, 1994), several button shapes have been found, one of which is shown in Fig. 1.5, as well as shapes which have the symmetry of the phases adjacent to the conformal phase W. Since at present the experimental determination of the reduced volume, let alone that of the mean curvature, is difficult for non-axisymmetric shapes lacking a simple comparison surface, the observed shapes can be related only qualitatively to the theoretical phase diagram.

As to the observation of conformal diffusion, Michalet gathered strong evidence by recording very slow shape transformations of shapes with a typical time scale t_{cf} of the order of a minute (Michalet, 1994). This is indeed the typical diffusion time expected since by dimensional analysis $t_{cf} = \eta R_0^3/T = (\kappa/T)t_b \simeq 25 t_b$ (Jülicher *et al.*, 1993a). Here, $t_b = \eta R_0^3/\kappa$ is the time-scale for long-wavelength bending fluctuations, which is of the order of a second,

and η is the solvent viscosity. The shape fluctuations Michalet recorded are different from bending fluctuations because there was no "mean" shape around which these fluctuations took place. Since only a cross-section of the shape can be observed, the main experimental problem is to distinguish conformal diffusion from slow rotational diffusion, which happens on a similar time-scale as t_{cf}.

5.6 Vesicles of higher genus

The theoretical prediction of conformal diffusion holds for higher genus as well, since, for $g \geq 2$, the solution to the Willmore problem is threefold degenerate with respect to conformal transformations (Karcher *et al.*, 1988; Hsu *et al.*, 1992). In addition, for higher genus, there occur further locally stable embedded Willmore surfaces which will give rise to degenerate local minima and even degenerate saddle points. In the (v, m)- phase diagram, the resulting degenerate phases may overlap and be connected by "regular" non-degenerate sheets. Obviously, a whole variety of interesting transitions can be expected in these systems, which are yet just rudimentarily investigated.

Experimentally, several shapes of higher genus have been found (Michalet *et al.*, 1994). A striking phenomenon is the occurrence of strong fluctuations of the position of the necks in shapes shown in Fig. 1.6, which correspond to those in the lower left corner of the phase diagram for genus-2. Even though these fluctuations do not correspond to conformal diffusion, their energy is quite small and, indeed, vanishes for $v \to 0$, which can be understood with a simple scaling estimate as follows.

For two concentric spheres of distance d connected by N necks, the linear distance L between necks scales as $L \sim R/\sqrt{N}$. For a neck connecting two planar sheets a distance d apart, the curvature energy scales as $\kappa(d/L)^2$, where L is the "size" of the circular patch where the neck is supposed to match the sheets (Michalet *et al.*, 1994). This power law anticipates a long-range interaction between necks. Displacing one neck a distance ϵL from its mean position in a lattice of necks costs an energy $\kappa(d/L)^2\epsilon^2$. Thus, the mean square amplitude of the position of the neck in units of mean neck separation become $< \epsilon^2 > \sim (T/\kappa)(L/d)^2 \sim (T/\kappa)(R/d)^2/N$. As a criterion for strong fluctuations, one can take that $< \epsilon^2 > \sim 1$. Thus, one expects strong fluctuations whenever

$$N \lesssim (T/\kappa)(R/d)^2 \sim (T/\kappa)/v^2. \tag{5.13}$$

This result differs qualitatively from the one presented in (Michalet *et al.*, 1994) where it is argued that the necks behave like a gas of free particles with a hard core radius $\sim \sqrt{dL}$. Such a description leads to a criterion for strong fluctuations, $N \lesssim 1/v \sim R/d$, that does

not involve temperature.

A refined theory should include the interaction between many necks, which is certainly important in the same way as the energy of n interacting handles is different from n times the energy of one handle as pointed out in Sect. 5.2.5. Likewise, for small d, one could include the interaction between the "spherical" parts of the shape, as has been done for necks connecting planar bilayers (Goos & Gompper, 1993). Finally, one may ask whether in the limit $R, N \to \infty$, with R^2/N fixed, a regular "lattice" of necks exists. Such an ordered state would require an effective long-range curvature interaction in order to beat the Mermin-Wagner theorem, which rules out two-dimensional "crystals" for systems with short range-interactions (Mermin & Wagner, 1966).

Chapter 6

Adhesion

The isolated or free vesicle, whose conformations and fluctuations we studied so far, is a theoretical model system which is quite challenging for detailed quantitative studies from an experimental perspective. Except for the analysis of quasi-spherical fluctuations, the permanent rotation and (less so) the translation of the vesicle in a measuring chamber render a quantitative analysis of both the mean shape and the fluctuations difficult, as long as the experimental recording techniques are confined to a single focus plane. With the advent of more sophisticated equipment like confocal laser scanning microscopy, this restriction may become less severe.

Experimentalists, however, have designed various set-ups by which vesicles can be spatially confined and manipulated so that the Brownian rotation becomes less of a problem. Among these techniques are binding a vesicle to a substrate either through attractive forces or through gravitation by filling it with a slightly denser liquid than the surrounding solution. Such a vesicle no longer exhibits significant translational diffusion. Therefore, its shape fluctuations, in particular those of its bound part, are accessible to much more sensitive techniques such as reflection interference contrast microscopy (Rädler, 1993; Rädler *et al.*, 1994). Evans has perfected the manipulation of vesicles by micropipets with which mutual adhesion can be studied in a controlled way (Evans, 1980a; Evans, 1990). Apart from these controlled means to adhere a vesicle, accidental adhesion has been observed optically in dilute suspensions (Servuss & Helfrich, 1989). Mutual adhesion of smaller vesicles can be studied by freeze-fracture electron microscopy, see, e.g. (Bailey *et al.*, 1990).

In fact, adhesion or interaction of membranes is an important topic not only as a means to orient a vesicle but rather for its ubiquitous occurrence in biological, biochemical and biophysical processes. In biology, adhesion of a vesicle represents an essential step for many processes such as endo- and exo-cytosis or fusion of cells (Alberts *et al.*, 1989). Efficient drug delivery by small vesicles requires an understanding of the interaction of the liposomes

with cell membranes (Lasic, 1994). Biosensors are based on the binding of membranes to substrates.

For a bound vesicle, the membrane segment close to the wall can experience a variety of inter-molecular forces (Israelachvili, 1991). The range of these forces is typically of the order of a few nanometers. The corresponding potential should have a minimum at finite distance in order to allow for a bound state at all, as discussed in Sect. 6.1. For vesicles that are much larger than this distance, the details of the spatial variation of the interaction potential should be irrelevant. In Sect. 6.2, we therefore replace this microscopic potential by a phenomenological contact potential, and analyse the effect of such an additional energy to the shape of a vesicle (Seifert & Lipowsky, 1990). This shape will be governed by the competition between adhesion and bending energies. As a central result, this competition leads to an adhesion transition. The effect of the finite range of the potential and of thermal fluctuations on both the shape of bound vesicles and the adhesion transition are discussed in Sects. 6.3 and 6.4, respectively. Since these sections are mainly theoretical, we close in Sect. 6.5 with numerical estimates of the relevant phenomena and discuss the few available experiments that can be related to our theoretical approach.

6.1 Bound planar membranes

Before we turn to bound vesicles, we briefly review in this section some of the extensive work on the adhesion of planar membranes in microscopic potentials for three reasons. (i) It is instructive to discuss an almost planar adhering membrane along the same lines as we discussed the fluctuations of an almost planar free membrane in Sects. 2.2 and 2.3. (ii) The contact potential approach discussed in Sect. 6.2 leads to a curvature-driven adhesion transition from a bound to a free state for closed vesicles (Seifert & Lipowsky, 1990). Since planar membranes can undergo a thermally driven unbinding transition (Lipowsky & Leibler, 1986; Mutz & Helfrich, 1989), it is important to discuss the interplay of these two mechanisms. (iii) In the next chapter, the dynamical fluctuations of a bound almost planar membrane are investigated. In order to classify the various regimes, an understanding of the static equilibrium fluctuations is a prerequisite.

6.1.1 Forces and effective potential

An almost planar membrane in the vicinity of a substrate experiences several kinds of forces (Israelachvili, 1991). It is useful to characterize and classify these forces by the effective potential $V(l)$ which they exert on a membrane at distance $l(x,y)$ from a substrate located

at $z = 0$ (Lipowsky & Leibler, 1986).

For charged membranes, the Coulomb interaction provides a long range potential $V(l) \sim 1/l$. On length scales beyond the Debye length, which depends on the salt concentration, this interaction becomes exponentially screened. Even for an uncharged membrane, the fluctuating dipoles lead to the van der Waals interaction which decays like a power law with various regimes depending on the separation. If the membrane is impermeable to large molecules, these molecules can be used to build up an osmotic pressure which pushes a membrane towards a substrate, yielding a linear potential in l. Finally, there are short range repulsive interactions. These include the "hydration forces", which are supposed to arise from a local rearrangement of hydrogen bondings near the membrane (Rand & Parsegian, 1989). More recently, the effect of local protrusions of the lipid molecules (Israelachvili & Wennerström, 1990) has been shown to lead to such an effective potential, too (Lipowsky & Grotehans, 1993).

If all these forces are summarized in a potential $V(l)$, the energy of an almost planar bilayer membrane near a substrate is given by

$$F^a = \int dx\, dy \left\{ \frac{\kappa}{2}(\nabla^2 l)^2 + \frac{\Sigma}{2}(\nabla l)^2 + V(l) \right\} . \tag{6.1}$$

For the bound part of a large vesicle, the tension Σ arises physically from the area constraint, as will be discussed in Sect. 6.4.1. Using the energy (6.1), the membrane is described within the classical model. Including the bilayer aspect along the lines of Sect. 2.3 leads to new effects for static problems only if a coupling between the separation l and the monolayer densities $\phi^{\pm}$ is introduced. Such a coupling could arise from the van der Waals interaction. Its exploration is left to future work.

6.1.2 Gaussian fluctuations

In a first step, the potential $V(l)$ is replaced by its harmonic approximation around the minimum l_0 with curvature

$$\Omega \equiv d^2V/dl^2|_{l=l_0}. \tag{6.2}$$

For a small local displacement,

$$h(x,y) \equiv l(x,y) - l_0, \tag{6.3}$$

of the membrane from the minimum, the free energy F_0^a of an adhering bilayer membrane in given by

$$F_0^a \equiv \frac{1}{2}\int \frac{d^2q}{(2\pi)^2} h_{\mathbf{q}} \left(\kappa q^4 + \Sigma q^2 + \Omega\right) h_{\mathbf{q}}^* \equiv \frac{1}{2}\int \frac{d^2q}{(2\pi)^2} h_{\mathbf{q}} E_0^a(q) h_{\mathbf{q}}^* , \tag{6.4}$$

where the latter relation defines the "energy" E_0^a.

Depending on the strength of the tension Σ, two cases must be distinguished theoretically.

(i) For *weak* tension ($\Sigma \ll 2\sqrt{\Omega\kappa}$), the tension term never dominates the energy E_0^a which thus exhibits only one cross-over length-scale at

$$\xi \equiv (\kappa/\Omega)^{1/4}. \tag{6.5}$$

For $q < 1/\xi$, the fluctuations of such a membrane are dominated by the potential, while for $q > 1/\xi$, they are governed by bending elasticity.

(ii) For *strong* tension ($\Sigma \gg 2\sqrt{\Omega\kappa}$), the tension dominates the energy in an intermediate range $\xi_\Sigma^{-1} < q < \xi_\kappa^{-1}$, with the two crossover length scales

$$\xi_\Sigma \equiv \sqrt{\Sigma/\Omega} \quad \text{and} \quad \xi_\kappa \equiv \sqrt{\kappa/\Sigma}. \tag{6.6}$$

The static height-height correlation functions are given in harmonic approximation as

$$< h_{\mathbf{q}} h^*_{\mathbf{q}'} >= \frac{T}{E_0^a(q)}(2\pi)^2\delta(\mathbf{q}-\mathbf{q}'). \tag{6.7}$$

6.1.3 Non-trivial fluctuations

The Gaussian approximation described above ignores both the presence of the hard wall constraint, $l(x,y) > 0$, and non-linear effects of the potential. Scaling theory as well as systematic work by renormalization group techniques show that this is permissible only for certain kinds of interaction potentials $V(l)$. For tension-less membranes ($\Sigma = 0$), three regimes must be distinguished depending on the range of the attractive and repulsive part of the direct interaction $V(l)$ (Lipowsky, 1990).

(i) *Mean-field regime:* If the direct *repulsive* part decays slower than $1/l^2$ for large l, Gaussian fluctuations capture the essential physics, and the presence of the hard wall can be ignored.

(ii) *Weak fluctuation regime:* If the *attractive* part of the direct potential decays slower than $1/l^2$ for large l, the effect of the hard wall can be incorporated by adding the "fluctuation potential" or "Helfrich-interaction" (Helfrich, 1978)

$$V_{fl}(l) \equiv c\frac{T^2}{\kappa l^2} \tag{6.8}$$

to the direct potential, and then calculating Gaussian fluctuations as above. Here, c is a numerical factor of order unity.

(iii) *Strong fluctuation regime:* If the attractive part decays faster than $1/l^2$ for large l, the effect of the hard wall is non-trivial, and superposition of direct interaction and fluctuation potential fails. In this regime, either renormalization group methods or Monte Carlo simulations are required to determine the effective fluctuations properly (Lipowsky, 1990; Lipowsky & Zielinska, 1989).

The effect of a non-zero tension on the membrane is to suppress fluctuations (Helfrich & Servuss, 1984). Therefore, the naive Gaussian approximation is valid for a larger class of potentials. In fact, it turns out that all direct potentials whose attractive and repulsive parts decay like power laws belong to the mean-field regime. For exponential interactions, the effect of the hard wall is extremely subtle and details of the direct interaction become crucial (Lipowsky, 1990).

These theoretical results will provide enough of a background to understand the effects of non-linear fluctuations for the adhesion of vesicles and the dynamics of adhering membranes.

6.2 Adhesion in a contact potential

6.2.1 Contact potential and contact curvature

For a vesicle bound to a substrate one may, in a first step, take advantage of the effective length-scale separation between the size of the vesicle and the range of the direct interactions which is of the order of several nanometers. Thus, one replaces the microscopic interaction potential $V(l)$ by an effective contact energy W, which can be identified by the value of the effective interaction potential at the mean separation of the membrane from the substrate. If the vesicle and the wall have the contact area A^*, the vesicle gains the adhesion energy (Seifert & Lipowsky, 1990)

$$F_a = -WA^*, \tag{6.9}$$

which must be added to the curvature energy.

Such a contact potential does not alter the shape equations found for free vesicles. It rather enters the boundary condition at the point of contact. First, the contact angle is necessarily π since any sharp bend would have an infinite curvature energy. This implies that the membrane is curved only in one direction, and $1/R_2^* = 0$ along the line of contact. Second, the contact curvature $1/R_1^*$ is determined by (Seifert & Lipowsky, 1990)

$$1/R_1^* = (2W/\kappa)^{1/2}, \tag{6.10}$$

which follows from minimizing with respect to the area of contact. This boundary condition, which does not depend on the area of the vesicle, holds for all variants of the curvature model.

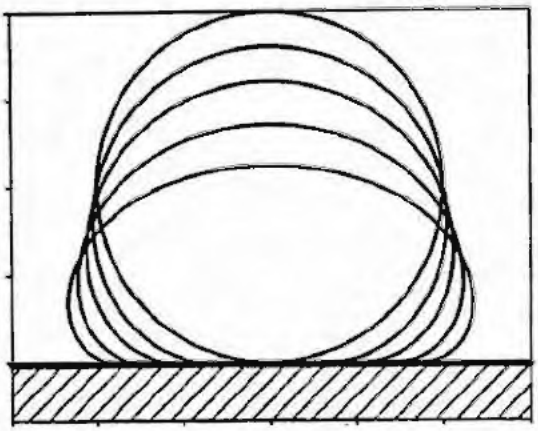

Figure 6.1: Shapes of bound vesicles which all have the same area for reduced adhesion energy w=2.0, 2.9, 4.1, 6.4, and 10.2 (Seifert & Lipowsky, 1990).

6.2.2 Adhesion transition

Solving the shape equations for axisymmetric shapes with the boundary condition (6.10) leads to a variety of bound shapes which can be arranged in a phase diagram as in the case of free vesicles. The basic physics behind the competition between adhesion and curvature energy becomes already evident in a minimal model, which contains only the local bending energy G (2.51), the adhesion energy F_a, a constraint on the total area $A = 4\pi R_0^2$ and no volume constraint. Such a model depends only on the reduced potential strength

$$w \equiv W R_0^2/\kappa. \tag{6.11}$$

Several shapes for different w are shown in Fig. 6.1. With decreasing strength of the contact potential w, the area of contact A^* also decreases and vanishes for $w = w_a = 2$. For the unscaled potential strength W, the area of contact vanishes at the size-dependent value

$$W_a = 2\kappa/R_0^2. \tag{6.12}$$

For $W = W_a$, the bound shape resembles the free shape corresponding to the same constraint, which is a sphere except for the fact that the contact curvature $1/R_1^* = 2/R_0$ is *twice* the curvature of the sphere. However, the contact *mean* curvature $H^* \equiv (1/R_1^* + 1/R_2^*)/2 = 1/R_0$ is equal to the mean curvature of the sphere. For $W < W_a$, an attractive potential does not lead to a bound shape with finite area of contact. Thus, the vesicle undergoes a continuous adhesion transition at $W = W_a$ (Seifert & Lipowsky, 1990).

A somewhat more complex situation arises when, in addition to the area, the enclosed volume is also kept constant. The phase diagram becomes two-dimensional, and depends

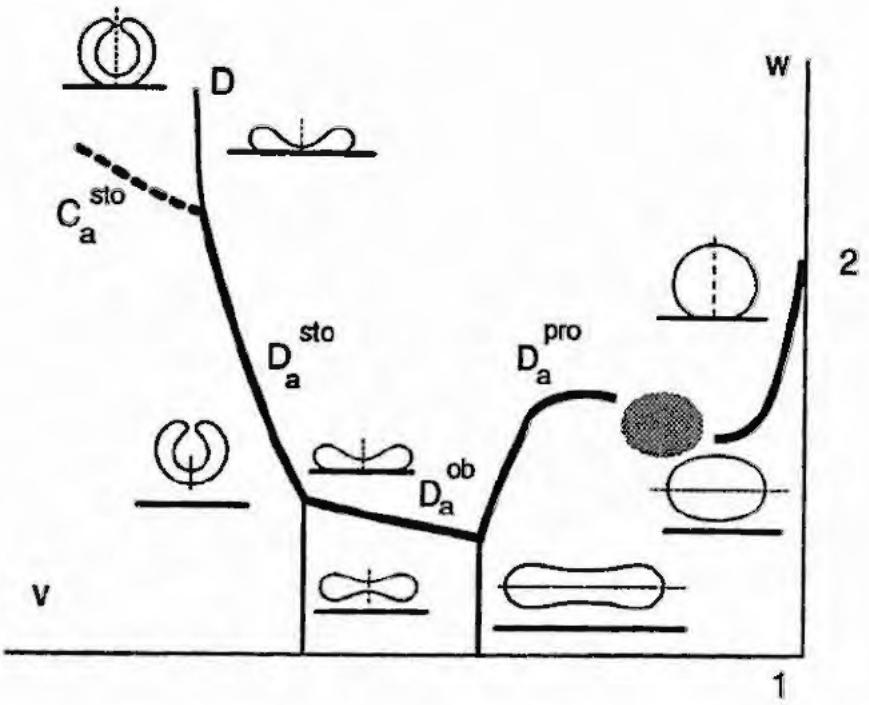

Figure 6.2: Schematic phase diagram with free and bound shapes at constant area and volume. The heavy lines show the adhesion transition at $w = w_a(v)$, which can be discontinuous (D_a^{pro}, D_a^{ob} and D_a^{sto}) or continuous (C_a^{sto}). In the dashed region, non-axisymmetric bound shapes are relevant. The dashed straight lines across the shapes denotes the axis of symmetry (Seifert & Lipowsky, 1993).

on v and w. This phase diagram is shown in Fig. 6.2, together with some bound shapes (Seifert & Lipowsky, 1993; Lipowsky & Seifert, 1991b; Lipowsky & Seifert, 1991a). Its main characteristic is the line of adhesion transitions $w_a(v)$ which separates bound from free states. The transition can be continuous or discontinuous depending on the reduced volume.

The four-dimensional phase diagram for adhesion with explicit inclusion of the area-difference elasticity energy has not yet been studied. In analogy to the free case, one expects that the non-local energy favors continuous adhesion transitions and the occurrence of non-axisymmetric shapes.

6.2.3 Relevance of non-axisymmetric shapes

For adhesion, non-axisymmetric shapes are more relevant than in the case of free vesicles, since the axisymmetry of free prolates is broken if these shapes adhere with their long axis parallel to the substrate. Such a bound shape can no longer be obtained by solving the

axisymmetric shape equations. However, some insight into the relevance of non-axisymmetric bound shapes can be obtained as follows (Seifert & Lipowsky, 1993). The critical value W_a for the *continuous* adhesion transition for the stomatocytes and the oblates (not appearing in the phase diagram) obeys the condition that for small A^*, the contact mean curvature of the bound shape, $H^* \equiv (1/R_1^* + 1/R_2^*)/2 = 1/2R_1^*$, becomes identical to the mean curvature H_f of the corresponding free shape at the point of contact. Using (6.12) this condition locates the *continuous* adhesion transition at

$$W_a = 2\kappa H_f^2. \tag{6.13}$$

For a sphere, one has $H_f = 1/R_0$ and one recovers the relation (6.12).

If the condition (6.13) is also valid for a (hypothetical) continuous transition of the prolates and dumbbells (with their axis of symmetry parallel to the wall), one finds that non-axisymmetric bound prolates show up as lowest energy states in the phase diagram, as indicated in Fig. 6.2. It remains to be seen whether the adhesion transition to these states is continuous at $W_a = 2\kappa H_f^2$ (where H_f is the mean curvature at the equator of the prolate) or discontinuous at $W_a < 2\kappa H_f^2$, and how far this region of non-axisymmetric bound shapes extends in the phase diagram. With increasing W, these non-axisymmetric states should then undergo a transition to axisymmetric bound shapes.

6.2.4 Effective contact angle

The adhesion transition takes place for $R_0 = R_a \equiv (w_a(v)\kappa/W)^{1/2}$, where w_a is of $O(1)$. For large vesicles with $R_0 \gg R_a$, i.e. for strong adhesion $W \gg W_a$, the shape of the bound

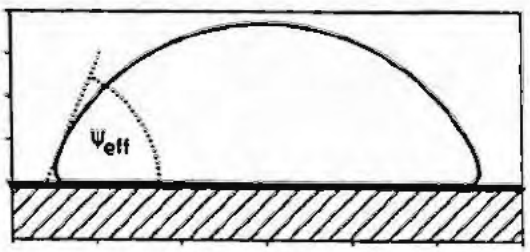

Figure 6.3: Spherical cap conformation for strong adhesion w=375 and effective contact angle $\Psi_{eff} = 65.5°$ (Seifert & Lipowsky, 1990).

vesicle approaches a simple limit shape. If only the area is constrained, this limit shape is a pancake with an energy

$$\kappa G + F_a \approx -2\pi W R_0^2 + 2\pi g (2\kappa W)^{1/2} R_0 \tag{6.14}$$

with the numerical coefficient $g \simeq 2.8$ (Lipowsky & Seifert, 1991b). If in addition the volume is constrained, the vesicle becomes a spherical cap for strong adhesion as shown in Fig. 6.3. In both cases, an *effective contact angle* Ψ_{eff}, which obeys a Young-Dupré equation, can be defined (Seifert & Lipowsky, 1990),

$$W = \Sigma(1 + \cos \Psi_{eff}) \tag{6.15}$$

with $\Psi_{eff} = 0$ for the pancake. In Eq. (6.15), the quantity Σ is the (numerical) value of the Lagrange multiplier for the area constraint. It also obeys the Laplace equation $2\Sigma + P/R_0 = 0$, where P is the Lagrangean multiplier used to implement the volume constraint. Thus, in this limit, $W \gg W_a$, the curvature energy becomes irrelevant, and adhesion of vesicles resembles wetting by liquid droplets.

6.2.5 Digression on strong adhesion: adhesion-induced rupture and fusion

For strong adhesion, elastic stretching of the membrane becomes relevant. In fact, the energetic competition which determines the conformation does not involve the balance between curvature energy and the adhesion energy, but rather the balance between the adhesion energy and the elastic energy

$$F_k \equiv (k/2)(A - A_0)^2/A_0. \tag{6.16}$$

Here, k is the area compressibility modulus of the order of 10^2 mJ/m^2 . Such an extended model leads to the same shape equations as the model with a hard area constraint. Even the boundary condition (6.10) remains unchanged. The phase diagram, however, changes due to the additional energy. Balancing the adhesion energy with the stretching term leads to the adhesion-induced stretching of the order of

$$(A - A_0)/A_0 \simeq W/k. \tag{6.17}$$

Identifying $k(A - A_0)/A_0$ with an elastic tension Σ_{el}, we find the relation $\Sigma_{el} \sim W$ for strong adhesion. The bound vesicle ruptures, as soon as Σ_{el} exceeds the lysis tension, which is known experimentally to happen at about $(A - A_0)/A_0 \simeq 0.03$ (Evans & Needham, 1987). From (6.17) one then derives that any adhesion potential stronger than $0.03k$ induces rupture.

After the bound vesicle has ruptured, its conformation becomes an open disc. Such a bound disc has an energy (Lipowsky & Seifert, 1991b)

$$F_{bd} = -4\pi W R_0^2 + 4\pi \Sigma_e R_0, \tag{6.18}$$

where Σ_e is the edge tension along the circumference of the bound disk. A comparison of the energy (6.18) with the energy (6.14) of a pancake shows that for $R_0 \gg R_{bd} \equiv \Sigma_e/W$ the bound disc always has lower energy.

The limit of strong adhesion can also be reached from a different route even if the original adhesion energy was not "strong". If more and more bound vesicles cover the substrate, they will come into contact and may fuse. For free vesicles, fusion of two vesicles with equal area $A \equiv 4\pi R_0^2$ (but no constraint on the volume) leads to a gain in energy $\Delta F_{fv} = 8\pi\kappa + 4\pi\kappa_G$. If two bound vesicles fuse, the gain in energy ΔF_{bv} is always larger than ΔF_{fv} and satisfies $\Delta F_{bv} \geq \tilde{g}\pi\kappa + 4\pi\kappa_G$ with $\tilde{g} \simeq 8.3$ (Lipowsky & Seifert, 1991b). For large R_0, this energy gain behaves as $\Delta F_{bv} \approx 4\pi g(\sqrt{2}-1)(\kappa W)^{1/2} R_0$, where (6.14) has been used. Thus, adhesion favors fusion. As the size of the fused vesicle increases, its shape becomes more like a pancake. If the elastic tension exceeds the threshold for lysis, the pancake ruptures and becomes an open bound disc.

These crude energetic considerations lead to a scenario where vesicles adhere to the wall, fuse at the wall and rupture. Finally, the open discs will also fuse, thus forming a bilayer parallel to the wall. Experimental evidence for such a scenario comes from X-ray scattering of a vesicle suspension which revealed a lamellar structure at the air-water interface (Cevc *et al.*, 1990). The strong temperature dependence of the dynamics of formation of the lamella that was found experimentally demonstrates that the kinetics of this process is quite subtle.

6.3 Adhesion in a potential with finite range: The pinned state

The contact potential is well-suited for studying the mean shape of bound vesicles, but is less convenient for discussion of the effect of thermal fluctuations. In such a potential, a membrane segment is either subject to the full adhesion energy if bound, or does not feel the substrate at all, if free.

In this section, we therefore consider adhesion of vesicles in a potential with non-zero range (Evans, 1985) as a prerequisite for the discussion of fluctuations in the next section. On the level of minimization of the energy, a potential with non-zero range can easily be introduced by replacing the contact term $-WA^*$ by the energy

$$F_a \equiv \oint ds_1 ds_2 \sqrt{g}\, V(l), \tag{6.19}$$

where $l = Z(s_1, s_2)$ is the local distance of the membrane segment with coordinates (s_1, s_2) from the wall. Here we assume that the interaction couples only to the membrane rather than to the enclosed liquid.

The shape equations and the boundary conditions get modified by this energy. So far, there have been no explicit calculation for three dimensional axisymmetric vesicles in such a potential even though this poses no principal problem. However, a closely related system, the adhesion of two-dimensional vesicles (i.e., ring polymers with rigidity (Leibler *et al.*, 1987; Maggs & Leibler, 1990)) in such a potential with finite range, has been investigated in considerable detail (Seifert, 1991a). The essential results of this study can be understood by simple scaling considerations which have the virtue of being easily transferable to the three-dimensional case (Seifert & Lipowsky, 1993).

In this section, these scaling arguments for the three-dimensional case are presented. Specifically, power law potentials of the form

$$V(l) = A\left(\frac{a}{l}\right)^r - B\left(\frac{a}{l}\right)^s, \tag{6.20}$$

with $r > s > 0$ and $A, B > 0$ are considered. Here, a is a molecular length-scale. This class of potentials has a single minimum at $l = l_0$, which we will also call the "range" of the potential, and a depth

$$V^0 \equiv V(l_0). \tag{6.21}$$

In the limit $B \to 0$, the minimum diverges like $l_0 \sim 1/B^{1/(r-s)}$ and the depth of the minimum vanishes as $V^0 \sim B^{r/(r-s)}$. In the following, l_0 and V^0 rather than A and B are used to characterize the potential.

The shape of minimal energy of a vesicle in such a potential can be classified into two cases depending on the range l_0 and on the size of the vesicle R_0 (Seifert & Lipowsky, 1993).

(1) For $R_0 \lesssim l_0$, i.e., for *small* vesicles or *long-range* potentials, the whole bound vesicle is exposed to the adhesion potential $V(l)$. The deviations from the free shape (with the same constraints) are significant, if the variation of the potential along the contour of the vesicle becomes comparable to the bending energy which scales as $\sim \kappa$. This happens at the potential strength $V^0 = V_f^0$, where

$$V_f^0 \sim \kappa {l_0}^2 / R_0^4, \tag{6.22}$$

as can be estimated by expanding the potential around its minimum. Thus, for $V^0 \ll V_f^0$, the bound vesicle keeps more or less its free shape and gains an energy

$$\Delta F \sim -V^0 R_0^2, \tag{6.23}$$

compared to the energy of a free vesicle at the same constraints, while for $V^0 \gtrsim V_f^0$ the adhesion potential deforms the free shape. A calculation of this specific shape would require solving the shape equations.

(2) For $l_0 \ll R_0$, i.e., *large* vesicles or *short-range* potentials, only the adjacent part of the vesicle is exposed to the potential and one should recover the results for the contact potential case. In fact, the limiting behaviour for small l_0/R_0 depends on the potential strength:

(i) If $V^0 > W_a$, where W_a is the critical value for the adhesion transition found in the contact potential, the vesicle in the smooth potential $V(Z)$ approaches, in the limit of small l_0/R_0, the same shape obtained for adhesion in a contact potential with strength $W = V^0$. In particular, the boundary condition (6.10) also evolves in this limit without being imposed. This limit has been considered explicitly for two-dimensional vesicles (Seifert, 1991a).

(ii) For $V^0 < W_a$, the vesicle approaches in the same limit the free shape (satisfying the same constraints). It remains, however, *pinned* in the (narrow) potential minimum up to the limit $l_0 = 0$ where, formally, it becomes pinned in only one point (Seifert, 1991a). Indeed, the area which is actually exposed to the potential well vanishes as $l_0 R_0$, which yields the energy gain

$$\Delta F \sim -V^0 l_0 R_0, \tag{6.24}$$

for small l_0/R_0 in the pinned state. If the adhesion transition found in a contact potential has been *discontinuous*, the finite range l_0 leads to a transition between the bound and the pinned state at

$$V^0 = V_a^0(l_0, R_0), \quad \text{with} \quad \lim_{l_0 \to 0} V_a^0(l_0, R_0) = W_a. \tag{6.25}$$

With increasing l_0 (or decreasing R_0), this discontinuous transition terminates in a critical point (Seifert, 1991a). If the adhesion transition in the contact potential has been *continuous*, the finite range l_0 leads to a smooth crossover between the bound and the pinned state. The pinned state, thus, replaces the free state found for adhesion in a contact potential.

6.4 Influence of thermal fluctuations

6.4.1 Fluctuations in the bound state

Gaussian fluctuations around the bound shape of minimal energy in a potential with non-zero range can, in principle, be treated using the formalism introduced in Chapter 4 since the adhesion potential just contributes to the first and second variation of the energy.

Even though a specific analysis for this problem has not yet been performed, a few general conclusions can be drawn. For a vesicle in the bound state, the fluctuations of its bound part

whose mean shape is planar can be described by the effective energy (6.4) in the following sense. For wavelengths that are small compared with the linear extension of the bound part R_0^*, the second variation of the bending energy just becomes the first term in (6.4). As the theorem proven in Sect. 4.1.2 shows, the area constraint leads to an effective tension Σ whose value is given by the Lagrange multiplier that corresponds to this mean shape. Finally, a harmonic approximation of the adhesion energy leads to the last term in the energy (6.4).

Obviously a detailed analysis of the fluctuations of bound vesicles is desirable for several reasons. First, the crossover to long wavelength fluctuations, which are shape dependent, should be studied. In the spherical cap limit, an effective theory for the cap-like conformation may evolve. Then one can study whether the cap-like part and the bound part interact only via effective boundary conditions along the rim. Finally, the role of the constraints for fluctuations which preserve the axisymmetry is more subtle as shown in Sect. 4.1.2. A priori, one can not expect to describe these fluctuations with the effective energy (6.4). For small wavelength, however, the effective energy may be recovered in the sense that the corrections arising from the constraints become small.

Since vesicles are finite systems, any bound state will eventually unbind through thermal activation. The concept of Gaussian fluctuations around a bound mean shape is meaningful only if the energy difference ΔF between the free and the bound state is large compared with the thermal energy T, i.e. for $|\Delta F| \gg T$. If this relation holds true, the bound state remains bound for exponentially long time scales.

6.4.2 Thermal activation of the pinned state

As a criterion for a characteristic depth $V^0 = V_u^0$ at which thermal activation sets in, we take the relation $|\Delta F(V_u^0)| \simeq T$. With the estimates (6.23) and (6.24), one obtains (Seifert & Lipowsky, 1993)

$$V_u^0 \sim \begin{cases} T/R_0^2 & \text{for} \quad R_0 \lesssim l_0 \\ T/(R_0 l_0) & \text{for} \quad l_0 \ll R_0 \lesssim R_c \equiv (\kappa/T) l_0. \end{cases} \tag{6.26}$$

The length scale R_c arises from the consistency requirement that $V^0 < V_a^0 \simeq W_a$, which was assumed when using the estimate (6.24) for ΔF. The breakdown of this relation for $R_0 > R_c$ indicates that large vesicles will not enter the pinned regime because the energy gain ΔF of such a pinned state would be smaller than the thermal energy T. Therefore, these large vesicles unbind at values of the potential depth V^0 for which the analysis at $T = 0$ would predict bound vesicles with finite contact area. Another physical mechanism must govern the unbinding of these large vesicles.

6.4.3 Thermal unbinding of large vesicles: role of effective tension

To understand the unbinding of large vesicles with $R_0 \gg l_0$, we start from the observation that fluctuations of the bound part of the vesicle can be described by the effective free energy (6.4) of an almost planar membrane in a potential $V(l)$ subject to a tension Σ, given by the value of the Lagrange multiplier belonging to this shape.

An infinite planar membrane subject to an attractive power law potential is bound for any non-zero value of the tension. Therefore, a necessary condition for the unbinding of a vesicle is that the linear dimension of its contact area, R_0^*, becomes smaller than the length-scale $\xi_\Sigma = \sqrt{\kappa/\Sigma}$, which was introduced in Eq. (6.6) as the crossover length below which the tension becomes irrelevant. Whether this condition is sufficient for the unbinding of the vesicle depends on the fact of whether or not a tensionless membrane at the corresponding strength of the potential is unbound, i.e., whether or not the corresponding V^0 is smaller than V^0_{open} where V^0_{open} is the critical strength for the unbinding of open tensionless membranes in such a potential. Renormalization group and scaling arguments show that for potentials of the class (6.20) with an exponent $s > 2$, V^0_{open} is non-zero and scales like $V^0_{open} \sim T^2/\kappa l_0^2$ (Lipowsky & Leibler, 1986; Lipowsky, 1990).

Using these two criteria, one can indeed derive the critical strength V_u^0 for the unbinding of vesicles with area constraints by a scaling argument as follows. As long as the vesicle is in the spherical cap conformation, $R_0^* \sim R_0$, and $\Sigma \sim V^0$, as given by the Young-Dupré equation. Combining these results, one finds that for $V^0 \lesssim \kappa/R_0^2$ the tension has become irrelevant. This value is indeed below the critical strength for the unbinding of tensionless membranes if the vesicle is larger than l_0. Thus, the unbinding of closed vesicles happens via thermal fluctuations of their bound part at the critical strength

$$V_u^0 \sim \kappa/R_0^2 \quad \text{for} \quad R_0 \gtrsim l_0. \tag{6.27}$$

The restriction in size given here matches the regime found for thermal activation of the pinned state. As a final consistency check, note that the vesicle loses the spherical cap conformation at a strength of the potential which also scales like κ/R_0^2. The critical strength for unbinding due to fluctuations of large vesicles, thus, exhibits the same size-dependence as the curvature-driven adhesion transition in the contact potential. The numerical prefactors, however, which are unaccessible within this simple scaling picture, will be different.

In summary, small vesicles unbind by thermal activation of the "whole" vesicle, large vesicles unbind via thermal fluctuations of their bound part (Seifert & Lipowsky, 1993). The area constraint leads to an effective tension which in turn leads to a size dependence of the critical depths of the potential. The different regimes for the unbinding of vesicles in potentials of the type (6.20) are summarized in Fig. 6.4.

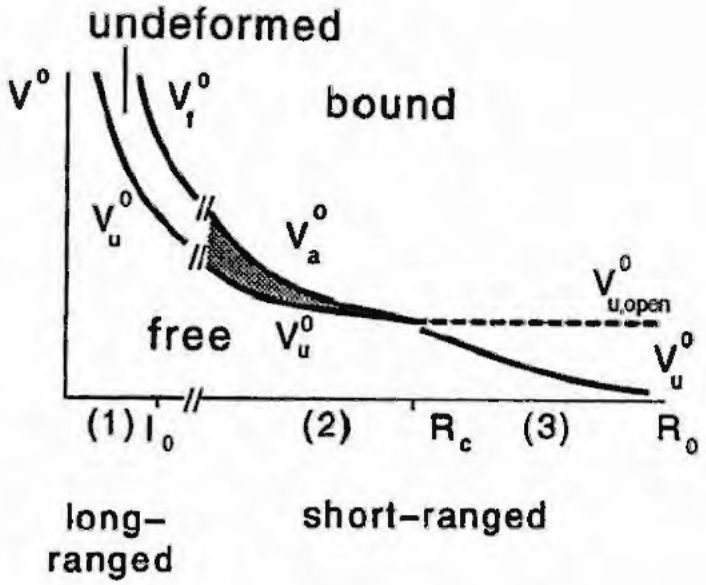

Figure 6.4: Schematic phase diagram for adhesion in a potential with finite range at finite temperature T. Depending on the three length scales l_0, R_0 and R_c, three different regimes of unbinding must be distinguished: (1) In a long-ranged potential ($R_0 \lesssim l_0$), decreasing the potential depth V^0 leads to a smooth crossover at $V^0 \simeq V_f^0$ where the bound shape changes from the deformed to an undeformed shape that is still bound. Such a vesicle unbinds via thermal activation at $V^0 \simeq V_u^0$. (2) In a short-ranged potential ($l_0 \ll R_0$), small vesicles with $R_0 < R_c$ first undergo the curvature-driven transition at $V^0 \simeq V_a^0$ from a bound state with finite contact area to the pinned state (shaded area) with the nearly free shape. These small vesicles then unbind via thermal activation at $V^0 \simeq V_u^0$. (3) Large vesicles with $R_0 > R_c$, cannot enter the regime of pinned states since they unbind via shape fluctuations in the contact zone at $V^0 \simeq V_u^0 \simeq \kappa/R_0^2$. $V_{u,open}^0$ denotes the critical strength for the unbinding of tensionless open membranes. (Seifert & Lipowsky, 1993).

It is desirable to check the predictions based on scaling arguments presented here with more rigorous techniques. Since an application of renormalization group techniques as developed for the unbinding of open membranes to the unbinding of a closed vesicle poses both conceptual and practical problems, computer simulations might be the only alternative to the approach discussed here.

Less clear is the situation for the unbinding of large vesicles in a potential governed by exponential forces since the critical behavior for the unbinding of a planar membrane under tension is not universal in these potentials. If the infinite planar membrane under finite tension unbinds at a zero strength of the potential, one can argue as above. However, those cases for which the infinite planar membrane *with* tension unbinds at a finite critical strength

$V^0_{open}(\Sigma)$ are more delicate. For the bound vesicle, the effective tension acting on the bound part decreases as $\Sigma \sim V^0$ with decreasing strength of the potential. The latter relation can formally be inverted to yield $V^0 = V^0(\Sigma)$. The vesicle will unbind when $V^0(\Sigma) = V^0_{open}(\Sigma)$ is reached. In this case, the critical value for the unbinding would not depend on the size of the vesicle in contrast to what was found for power law potentials. As a consequence, the two regimes, (i) unbinding due to thermal activation and (ii) unbinding due to fluctuations of the bound part, would not necessarily have to match. Clearly, more work is needed to understand unbinding of vesicles in short-range potentials.

6.5 Estimates and experiments

In this section, we estimate the relevant length-scales for adhesion of vesicles and discuss the few experiments on bound vesicles available so far.

The crucial quantity in the theory is the interaction potential $V(l)$. Information about the adhesion potential can be inferred mainly from two experimental techniques. First, X-ray diffraction on oriented multi-layers yields the potential as a function of the mean separation between layers, which can be varied by changing the osmotic pressure (Parsegian *et al.*, 1979; Rand & Parsegian, 1989). The effective contact potential can then be identified with the value of the potential $V(l)$ in the minimum l_0 in the absence of an external pressure. Secondly, effective contact potentials can also be inferred from micro-pipet aspiration experiments (Evans, 1990) and from video microscopy of dilute systems (Servuss & Helfrich, 1989).

With these techniques, effective interactions are measured which may be renormalized due to the effect of fluctuations. These fluctuations can be more or less restricted either by lateral tension, such as applied with the micro-pipet technique or more severely, by immobilizing the membranes on a surface force apparatus (Marra & Israelachvili, 1985). Consequently, the different experimental methods give, in general, different values for the effective contact potential W, which are in the range between $10^{-4} - 1$ mJ/m^2. For rough estimates in this section, we will use the value of 1 mJ/m^2 for *strong* adhesion, and the value of 10^{-4}mJ/m^2 for *weak* adhesion.

The contact curvature $1/R_1^*$ expected from these estimates span $1/R_1^* \simeq 1/(10\text{nm})$ for strong adhesion (using $\kappa = 10^{-19}$J) and $1/R_1^* \simeq 1\mu\text{m}^{-1}$ for weak adhesion. The latter value clearly is accessible by light microscopy. The adhesion transition, driven by the competition between adhesion energy and curvature energy, happens when the contact curvature becomes of the order of the size of the vesicle. Thus, one would expect that it should be observable by light microscopy for large vesicles. However as the discussion on the effect of fluctuations has shown, this mechanism will apply only below a crossover radius R_c of the order of $l_0(T/\kappa)$

introduced in Eq. (6.26). If we ignore the, at present, unaccessible numerical prefactors, one expects $R_c \simeq 0.1\mu$m with the typical values $l_0 = 4$nm and $\kappa/T = 25$. Such a crossover is below optical resolution, which would mean that vesicles accessible by light microscopy cannot reach the pinned regime. The crossover radius might, however, be shifted to larger values using multi-lamellar vesicles because κ is proportional to the number of bilayers.

The most thorough experimental study of the morphology of bound vesicles along the lines outlined here has been performed by Rädler (Rädler & Sackmann, 1992a; Rädler, 1993; Rädler *et al.*, 1994). The main technique consists in using reflection interference contrast microscopy (Zilker *et al.*, 1987; Zilker *et al.*, 1992; Rädler & Sackmann, 1992b) to measure distances from a coated substrate with a resolution of the order of a nanometer whereas the lateral resolution is confined to an optical wave-length. With this technique, a contact curvature of the order of $1/(10\mu\text{m})$ has been reported, from which the contact energy has then been determined. Similar values have also been found in dilute membrane systems (Servuss & Helfrich, 1989). Spherical cap-like conformations are clearly seen in micro-pipet experiments as well as in electron microscopy for smaller vesicles (Bailey *et al.*, 1990). Pancakes for strong adhesion have also been found in Rädler's study.

The unbinding of vesicles has not yet been verified experimentally even though evidence for a thermally driven unbinding transition in dilute membrane systems has been found (Mutz & Helfrich, 1989). Two different approaches are conceivable in order to observe the curvature-induced adhesion transition for vesicles experimentally. (i) Changing the temperature will affect both the reduced volume and the scaled adhesion potential $w = WR_0^2/\kappa$ via the area expansion. A temperature decrease also decreases w and increases v. Therefore, a bound vesicle may become free upon cooling provided its initial state at the higher temperature is already sufficiently close to the adhesion transition. Likewise, osmotic deflation or inflation, which does not affect w, can induce a crossing of the adhesion transition in the phase diagram Fig. 6.2. (ii) A more indirect but quite elegant confirmation of the theory described above could make use of the characteristic size-dependence of the adhesion transition as expressed in Eq. (6.12). This relation implies that, for fixed W, in an ensemble of vesicles, only those with $R_0 > R_a \equiv (2\kappa/W_a)^{1/2}$ are bound to the substrate.

The "cleanest" experiments on bound vesicles so far, however, do not concern the aspect of unbinding but rather address the fluctuations of the bound part of vesicles (Rädler *et al.*, 1994). If it were feasible to induce unbinding by changing one parameter continuously which would weaken the effective potential, one could monitor the fluctuations of the bound part of the vesicle as the mean distance to the substrate changes. If these fluctuations are analysed using the correlation function (6.7), the change in the effective tension could be measured and correlated with the theoretical prediction of unbinding.

Chapter 7

Dynamics

Slow conformational changes of the bilayer as they are visible in the microscope, and as they can be recorded with a video camera comprise two aspects. First, there are the dynamical equilibrium fluctuations around the shape of lowest energy. Second, a discontinuous shape transformation involves essentially deterministic motion as an unstable shape decays towards the new minimum. In both cases, the presence of the surrounding liquid into which the membrane is embedded determines the dynamics in an important non-trivial way, since it generates an effective long-range dynamical interaction along the membrane.

Apart from dissipation in the viscous liquid, which has been recognized as an essential damping mechanism for some time (Kramer, 1971; Brochard & Lennon, 1975), a second source of dissipation has been appreciated just recently (Evans *et al.*, 1991; Seifert & Langer, 1993). This process arises from the dynamical counterpart of the area-difference elasticity introduced in Sect. 2.3: Local inhomogeneities of the lipid density in the neutral surface of each monolayer caused by sudden bending of the bilayer can relax laterally, if the two leaflets slide over each other. This process, however, is subject to friction in the tail region of the hydrocarbon-chains.

In this Chapter, basic aspects of the collective dynamics of conformation, lipid densities and the embedding liquid are discussed. In Sect. 7.1, the hydrodynamic equations for the coupled system comprising membrane and surrounding fluid are introduced. Eliminating the viscous liquid leads to a non-local equation of motion for the membrane. In Sect. 7.2, we use this equation to recall the dynamical fluctuations of an almost planar membrane in the classical model where dissipation arises form the viscous damping in the liquid alone (Brochard & Lennon, 1975).

The dynamical part of the bilayer aspect of the membrane is treated for an almost planar membrane in Sect. 7.3. It is shown that friction between the leaflets fundamentally alters the relaxation spectrum or the shape fluctuations below a meso-scopic length-scale (Seifert &

Langer, 1993). The dynamical fluctuations of the bound part of an adhering vesicle (Seifert, 1994a; Kraus & Seifert, 1994) are discussed in Sect. 7.4; in this geometry, quantitative measurements of collective dynamical processes have become feasible just recently (Rädler, 1993).[1]

7.1 Equations of motions

An equation of motion for the membrane can be derived by starting from the Navier-Stokes equations for the surrounding viscous liquid and introducing the membrane later. The Navier-Stokes equations for the velocity field $\mathbf{v}(\mathbf{r})$ of the solvent with density ρ_f and viscosity η are given by

$$\frac{d}{dt}(\rho_f \mathbf{v}) + \nabla p - \eta \nabla^2 \mathbf{v} = \mathbf{K}(\mathbf{r}), \tag{7.1}$$

where $p(\mathbf{r})$ denotes the pressure, and $\mathbf{K}(\mathbf{r})$ are the external forces acting on the liquid. These include both forces exerted from the membrane and forces due to confining boundaries, such as the presence of a substrate in the case of adhesion.

To a very good approximation, the inertial term in the Navier-Stokes equation can be neglected for the range of phenomena in which we are interested. As can be checked a posteriori, the corresponding Reynolds numbers are small compared with 1. In the so-called Stokes approximation, one then has to solve the force balance

$$\nabla p - \eta \nabla^2 \mathbf{v} = \mathbf{K}(\mathbf{r}). \tag{7.2}$$

Moreover, for these phenomena, the liquid can be considered as incompressible

$$\nabla \cdot \mathbf{v} = 0, \tag{7.3}$$

which can be used to eliminate the pressure in (7.2) in favor of the forces.

These equations are solved formally by introducing the Fourier transformation as

$$\mathbf{v}_\mathbf{k} = \int e^{-i\mathbf{k}\cdot\mathbf{r}} \mathbf{v}(\mathbf{r})\, d^3r \tag{7.4}$$

and

$$\mathbf{K}_\mathbf{k} = \int e^{-i\mathbf{k}\cdot\mathbf{r}} \mathbf{K}(\mathbf{r})\, d^3r\,. \tag{7.5}$$

The solution to Eqs. (7.2) and(7.3) then becomes a linear relationship

$$v_{\mathbf{k}i} = \frac{1}{\eta k^2}\left(\delta_{ij} - \frac{k_i k_j}{k^2}\right) K_{\mathbf{k}j} \tag{7.6}$$

[1] The dynamics of shape transformations of vesicles is a more elaborate issue which we will not touch here. A few theoretical steps in this direction can be found in (Bruinsma, 1991; Fischer, 1994; Seifert, 1994b).

between the velocity field and the external forces, where i, j denote Cartesian components. (v_{ki} is short for $(\mathbf{v_k})_i$ to keep the notation simple.) In real space, relation (7.6) reads

$$\mathbf{v}(\mathbf{r}) = \int d^3r' \mathcal{O}(\mathbf{r}, \mathbf{r}')\mathbf{K}(\mathbf{r}'), \tag{7.7}$$

where the Oseen tensor $\mathcal{O}(\mathbf{r}, \mathbf{r}')$ has matrix elements (Doi & Edwards, 1986)

$$O_{ij}(\mathbf{r}, \mathbf{r}') \equiv \frac{1}{8\pi\eta|\mathbf{r} - \mathbf{r}'|}\left[\delta_{ij} + \frac{(r_i - r_i')(r_j - r_j')}{|\mathbf{r} - \mathbf{r}'|^2}\right]. \tag{7.8}$$

Thus, the hydrodynamics generates a long-range interaction ($\sim 1/|\mathbf{r} - \mathbf{r}'|$) through the velocity field.

Since essentially no liquid penetrates the membrane, as discussed in Sect. 1.3, we can identify the normal velocity of the liquid, $\mathbf{v}(\mathbf{R}(s_1, s_2)) \cdot \mathbf{n}(s_1, s_2)$, at any point $\mathbf{R}(s_1, s_2)$ of the membrane with a conformational change of the membrane. Thus, we obtain a dynamical equation of motion for the membrane as

$$\partial_t \mathbf{R}(s_1, s_2, t) \cdot \mathbf{n}(s_1, s_2, t) = \mathbf{n}(s_1, s_2, t) \cdot \int d^3r' \mathcal{O}(\mathbf{r}, \mathbf{r}')\mathbf{K}(\mathbf{r}'). \tag{7.9}$$

At this stage, the tangential components of the liquid velocity are not yet relevant for a shape change.

To proceed, we need expressions for the forces exerted by the membrane upon the liquid. As a simple model, consider a membrane which is subject only to bending energy and which cannot sustain or exert any tangential forces. For such a membrane, the force density $\mathbf{K}(\mathbf{r})$ follows from the first variation of the bending energy F_M (2.53) as

$$\begin{aligned} \mathbf{K}(\mathbf{r}) &= -\int ds_1 ds_2 \mathbf{n}(s_1, s_2) \frac{\delta F_M}{\delta \epsilon(s_1, s_2)} \delta(\mathbf{r} - \mathbf{R}(s_1, s_2)) \\ &= 2\kappa \int ds_1 ds_2 \mathbf{n}(s_1, s_2)[2H(H^2 - K) - \Delta H]\delta(\mathbf{r} - \mathbf{R}(s_1, s_2)). \end{aligned} \tag{7.10}$$

For any given initial conformation $\mathbf{R}_0(s_1, s_2)$, this force density yields, after insertion into the equation of motion (7.9), a conformational change along the local normal.

The tangential velocity of the liquid, so far, has been irrelevant since it does not couple to the shape within the simplified model just described. For a physically more meaningful membrane model, one should include tangential forces. The next step in sophistication consists of a locally incompressible membrane with no-slip boundary conditions between the lipid flow within the membrane and the liquid velocity at the membrane. For such a model, one has to add a local surface tension to the bending energy. This tension, as well as the unknown tangential forces, have to be determined self-consistently by requiring

that the tangential velocity at the membrane is divergence-free, which corresponds to the condition of incompressibility. The implementation of such a model requires some care concerning both fundamental aspects, such as reparametrization invariance of the surface, and numerical aspects such as superficial divergences due to the $1/r$ singularity of the Oseen tensor (Langer & Seifert, 1994).

In this section, we focus specifically on two paradigmatic dynamical problems which are accessible to an analytical approach. We consider the dynamical equilibrium fluctuations of a free and a bound almost planar membrane. For these cases, many subtleties of the general case vanish since the displacements from the planar conformation are small.[2]

For such a geometry, it is convenient to apply a Fourier transformation parallel to the membrane plane according to

$$\mathbf{v}_\mathbf{q}(z) = \int e^{-i\mathbf{q}\cdot\mathbf{x}}\mathbf{v}(\mathbf{r})\,d\mathbf{x} \tag{7.11}$$

and

$$\mathbf{K}_\mathbf{q}(z) = \int e^{-i\mathbf{q}\cdot\mathbf{x}}\mathbf{K}(\mathbf{r})\,d\mathbf{x}\,, \tag{7.12}$$

where $\mathbf{r} = (\mathbf{x}, z) = (x, y, z)$. Moreover, one can decompose the velocity and the force fields into their z, longitudinal and transversal components as

$$\mathbf{v}_\mathbf{q}(z) \equiv v_{\mathbf{q}z}(z)\hat{\mathbf{z}} + v_{\mathbf{q}l}(z)\hat{\mathbf{q}} + v_{\mathbf{q}t}(z)\hat{\mathbf{t}}, \tag{7.13}$$

and

$$\mathbf{K}_\mathbf{q}(z) \equiv K_{\mathbf{q}z}(z)\hat{\mathbf{z}} + K_{\mathbf{q}l}(z)\hat{\mathbf{q}} + K_{\mathbf{q}t}(z)\hat{\mathbf{t}} \tag{7.14}$$

where $\hat{\mathbf{q}}$ is the unit-vector parallel to $\mathbf{q}$, and $\hat{\mathbf{t}}$ is the in-plane vector perpendicular to $\mathbf{q}$ and $\hat{\mathbf{z}}$.

Inserting these expressions for the Fourier transformed quantities into the relation (7.6) yields, with little algebra, the relationship between velocity and force components as

$$v_{\mathbf{q}z}(z) = \frac{1}{4\eta q}\int_{-\infty}^{\infty} dz'\, e^{-q|z-z'|}[(1+q|z-z'|)K_{\mathbf{q}z}(z') + iq(z'-z)K_{\mathbf{q}l}(z')], \tag{7.15}$$

$$v_{\mathbf{q}l}(z) = \frac{1}{4\eta q}\int_{-\infty}^{\infty} dz'\, e^{-q|z-z'|}[(1-q|z-z'|)K_{\mathbf{q}l}(z') + iq(z'-z)K_{\mathbf{q}z}(z')], \tag{7.16}$$

and

$$v_{\mathbf{q}t}(z) = \frac{1}{4\eta q}\int_{-\infty}^{\infty} dz'\, e^{-q|z-z'|}2K_{\mathbf{q}t}(z'). \tag{7.17}$$

Since the transverse components do not couple to the normal displacements in this geometry, they can be ignored in the following.

[2]Non-linear effects for a local relaxational dynamics without the hydrodynamic interaction are discussed in (Cai & Lubensky, 1994; Foltin, 1994).

7.2 Almost planar membrane: Classical model

As an instructive example, we first recall the relaxation of small displacements $h(x,y,t)$ of an almost planar membrane around its equilibrium position at $z = 0$ within the classical model, which will be derived here in a somewhat different approach than given in the original work (Brochard & Lennon, 1975). The restoring forces are small and proportional to h. Therefore, they can be assumed to act only in the plane $z = 0$, since the fact that they act at the local position $h(x,y,t)$ of the membrane is an effect of higher order. For such a force density,

$$K_{\mathbf{q}z}(z) \equiv \delta(z)[K_{\mathbf{q}z}\hat{\mathbf{z}} + K_{\mathbf{q}l}\hat{\mathbf{q}}], \tag{7.18}$$

the relations (7.15) and (7.16) immediately yield a decoupling of the z- and the longitudinal components according to

$$v_{\mathbf{q}r}(0) = \frac{1}{4\eta q} K_{\mathbf{q}r} \quad \text{with} \quad r = z \text{ or } l. \tag{7.19}$$

For the classical model, the normal force $K_{\mathbf{q}z}$ is given by the derivative of the bending energy F_0 (as introduced in Eq. (2.13)) as

$$K_{\mathbf{q}z} = -\frac{\partial F_0}{\partial h_{\mathbf{q}}^*} = -E_0(q)h_{\mathbf{q}} = -\kappa q^4 h_{\mathbf{q}}. \tag{7.20}$$

If the normal velocity at the membrane is identified with the time derivative of h, i.e.

$$\partial_t h_{\mathbf{q}} = v_{\mathbf{q}z}(0), \tag{7.21}$$

one obtains from relation (7.19) the equation of motion for the membrane in the form

$$\partial_t h_{\mathbf{q}} = -\Gamma_0(q)E_0(q)h_{\mathbf{q}}. \tag{7.22}$$

The "kinetic coefficient"

$$\Gamma_0(q) = 1/4\eta q \tag{7.23}$$

reflects the long range character of the hydrodynamic damping. In the solution to this equation of motion,

$$h_{\mathbf{q}}(t) = h_{\mathbf{q}}(0)e^{-\gamma_0(q)t}, \tag{7.24}$$

the damping rate $\gamma_0(q)$ is easily identified as

$$\gamma_0(q) = \Gamma_0(q)E_0(q) = \kappa q^3/4\eta. \tag{7.25}$$

The form (7.25) of the damping rate as a product (Marathe & Ramaswamy, 1989) of a kinetic coefficient which contains the dissipation, and an energy which contains the driving

force, will persist if we take the bilayer aspect of the membrane into account, as well as for a bound membrane.

The dynamical correlation function in this classical model can be obtained by multiplying the solution (7.24) with $h^*_{\mathbf{q}'}(0)$ and averaging with the Boltzmann weight $\exp(-F_0/T)$ which yields

$$< h_{\mathbf{q}}(t) h^*_{\mathbf{q}'}(0) >= \frac{T}{\kappa q^4} e^{-\omega(q)t} (2\pi)^2 \delta(\mathbf{q} - \mathbf{q}'). \tag{7.26}$$

7.3 Almost planar membrane: Bilayer dynamics

7.3.1 Force balance

If the membrane is described in the refined bilayer model introduced in Sect. 2.3, the normal force is given by

$$K_{\mathbf{q}z} = -\frac{\partial F}{\partial h^*_{\mathbf{q}}} = -[\tilde{\kappa} q^4 h_{\mathbf{q}} - 2kdq^2 \rho_{\mathbf{q}}], \tag{7.27}$$

where the bilayer energy F was defined in Eq. (2.28). If this force density is inserted into Eq. (7.19), one obtains with Eq. (7.21) the equation of motion for the height variable

$$\partial_t h_{\mathbf{q}} = -\Gamma_0(q)[\tilde{\kappa} q^4 h_{\mathbf{q}} - 2kdq^2 \rho_{\mathbf{q}}], \tag{7.28}$$

which involves the local density difference ρ. To obtain a closed system of equations, we need a dynamical equation for this density difference.

Such an equation of motion can be obtained from the in-plane force balance within each monolayer which reads (Seifert & Langer, 1993)

$$-\tilde{\nabla}\sigma^{\pm} \pm T^{\pm}_{zz} + \mu \tilde{\nabla}^2 \tilde{v}^{\pm} \mp b(\tilde{v}^{+} - \tilde{v}^{-}) = 0, \tag{7.29}$$

where the tilde refers to two dimensional quantities. The four force densities in (7.29) are

(*i*) the (in-plane) gradient of the surface pressure

$$-\tilde{\nabla}\sigma^{\pm} = -\tilde{\nabla}\frac{\delta F}{\delta \rho^{\pm *}}, \tag{7.30}$$

which arises form the elastic stretching or compression within each monolayer;

(*ii*) the tractions $T^{\pm}_{zz}$ of the surrounding fluid, which have the same magnitude but different sign as the (yet unknown) tangential forces $K^{\pm}_{\mathbf{q}l} = 4\eta q v^{\pm}_{\mathbf{q}l}(0)$ exerted from the membrane on the liquid;

(*iii*) a viscous shear damping within each monolayer[3] where μ is the monolayer shear viscosity and $\tilde{\mathbf{v}}^{\pm}$ is the velocity of the lipid flow within each monolayer;

(*iv*) the friction between the two monolayers with the phenomenological friction coefficient b (Evans *et al.*, 1991; Yeung, 1994). As pointed out in (Yeung, 1994), the justification for describing this friction as viscous arises from the fast motion of the dangling ends of the hydrocarbon-chains, which dynamically interdigitate slightly on a relatively fast time-scale, of order 10^{-9} sec, as shown by molecular dynamics simulations (de Loof *et al.*, 1991). This fast molecular motion of the dangling ends should give rise to an effectively viscous friction on the much slower time scale of typical shape changes.

The densities $\rho^{\pm}$ obey equations of continuity

$$\partial_t \rho^{\pm} \approx -\widetilde{\nabla} \cdot \tilde{\mathbf{v}}^{\pm} \tag{7.31}$$

to lowest order in the small quantities $\rho^{\pm}$ and $\tilde{\mathbf{v}}^{\pm}$.

Assuming conventional non-slip boundary conditions between liquid and membrane flow, i.e. $\tilde{\mathbf{v}}^{\pm} = v_{\mathbf{q}l}^{\pm}(0)\hat{\mathbf{q}}$, the equation of continuity (7.31) can be used to replace the velocities in the force balance (7.29). The difference of the two equations (7.29) then leads, after Fourier transformation, to the equation of motion for the density difference $\rho_{\mathbf{q}}$. This equation and the corresponding one for $h_{\mathbf{q}}$ can be written in the form (Seifert & Langer, 1994)

$$\frac{\partial}{\partial t}\begin{pmatrix} h_{\mathbf{q}} \\ \rho_{\mathbf{q}} \end{pmatrix} = -\mathbf{\Gamma}(q)\mathbf{E}(q)\begin{pmatrix} h_{\mathbf{q}} \\ \rho_{\mathbf{q}} \end{pmatrix}. \tag{7.32}$$

Here, $\mathbf{E}(q)$ is the upper left (2×2)submatrix of $\mathbf{E}(q)$ as defined in Eq. (2.29) for which we will not introduce a new notation. The matrix of kinetic coefficients

$$\mathbf{\Gamma}(q) \equiv \begin{pmatrix} 1/4\eta q & 0 \\ 0 & \dfrac{q^2}{2(2b + 2\eta q + \mu q^2)} \end{pmatrix} \tag{7.33}$$

shows that, for small q, the dissipation for the density difference mode is dominated by the inter-monolayer friction with coefficient b. It has a q^2-dependence because densities are conserved quantities.

The dynamical equation for the average density $\bar{\rho}_q$, which also follows from this procedure should not be taken seriously since for this quantity the inertial terms are crucial to the dynamics. As shown in (Seifert & Langer, 1993), including the inertial terms within the membrane leads to propagating sound-waves in $\bar{\rho}_q$.

[3]For simplicity, and since this damping mechanism will turn out to be irrelevant except on very small length-scales, we ignore any dilational viscosity. For the insoluble phospholipids, dilational viscosity can be expected to be of the same order than shear viscosity whereas for soluble monolayers the dilational viscosity can be two orders of magnitude larger (Langevin, 1992).

7.3.2 Dispersion relation and height-height correlation function

The formal solution to the relaxational dynamics (7.32) is

$$\begin{pmatrix} h_{\mathbf{q}}(t) \\ \rho_{\mathbf{q}}(t) \end{pmatrix} = \exp\left(-\mathbf{\Gamma}\cdot\mathbf{E}\, t\right) \begin{pmatrix} h_{\mathbf{q}}(0) \\ \rho_{\mathbf{q}}(0) \end{pmatrix}. \tag{7.34}$$

After diagonalization, the relaxation times of the various modes follow as the inverse values of the eigenvalues γ_i of $\mathbf{\Gamma}\cdot\mathbf{E}$ while the time-dependent correlation functions can be obtained from the corresponding eigenvectors.

The dispersion relation of the two eigenvalues $\gamma_{1,2}(q)$ is shown in Fig. 7.1. There are three regimes (Seifert & Langer, 1993) separated by the crossover wave-vectors $q_1 \equiv 2\eta k/b\tilde{\kappa}$ and $q_2 \equiv \sqrt{2b/\mu}$:

$$\gamma_1 \approx \begin{cases} \dfrac{\kappa}{4\eta}q^3, & q \ll q_1 \\ \dfrac{k}{2b}\dfrac{\kappa}{\tilde{\kappa}}q^2, & q_1 \ll q \ll q_2 \\ \dfrac{k}{\mu}\dfrac{\kappa}{\tilde{\kappa}}, & q_2 \ll q. \end{cases} \qquad \gamma_2 \approx \begin{cases} \dfrac{k}{2b}q^2, & q \ll q_1 \\ \dfrac{\tilde{\kappa}}{4\eta}q^3, & q_1 \ll q \end{cases} \tag{7.35}$$

For the dynamical height-height correlation function, one finds

$$< h_{\mathbf{q}}(t)h^*_{\mathbf{q}'}(0) >= \frac{T}{\kappa q^4}\left(A_1^h(q)e^{-\gamma_1(q)t} + A_2^h(q)e^{-\gamma_2(q)t}\right)(2\pi)^2\delta(\mathbf{q}-\mathbf{q}'). \tag{7.36}$$

Likewise, the density-density correlations become

$$< \rho_{\mathbf{q}}(t)\rho^*_{\mathbf{q}'}(0) >= \frac{T\tilde{\kappa}}{2k\kappa}\left(A_1^\rho(q)e^{-\gamma_1(q)t} + A_2^\rho(q)e^{-\gamma_2(q)t}\right)(2\pi)^2\delta(\mathbf{q}-\mathbf{q}'). \tag{7.37}$$

The fluctuation-dissipation theorem enforces $A_2^{h,\rho}(q) = 1 - A_1^{h,\rho}(q)$. These amplitudes are also shown in Fig. 7.1.

The asymptotic behavior of the damping rates and the correlation function can be understood as follows. For small q, γ_1 corresponds to the classical hydrodynamically damped bending mode γ_0 (7.25) and γ_2 is the damping rate of a new "slipping" mode, a density difference fluctuation damped by the inter-monolayer friction. In this regime, undulations relax only by the slow mode, so $A_1^h \approx 1$, and A_2^h is negligibly small, since the height variable is too slow to follow the fast density fluctuations. A similar consideration applies to A_1^ρ, A_2^ρ (Kraus & Seifert, 1994).

For $q \gg q_1, \gamma_2$ becomes the damping rate of a bending mode, with an effective bending rigidity $\tilde{\kappa}$ identified already in Sect. 2.3 as the bending rigidity for "frozen" lipid molecules

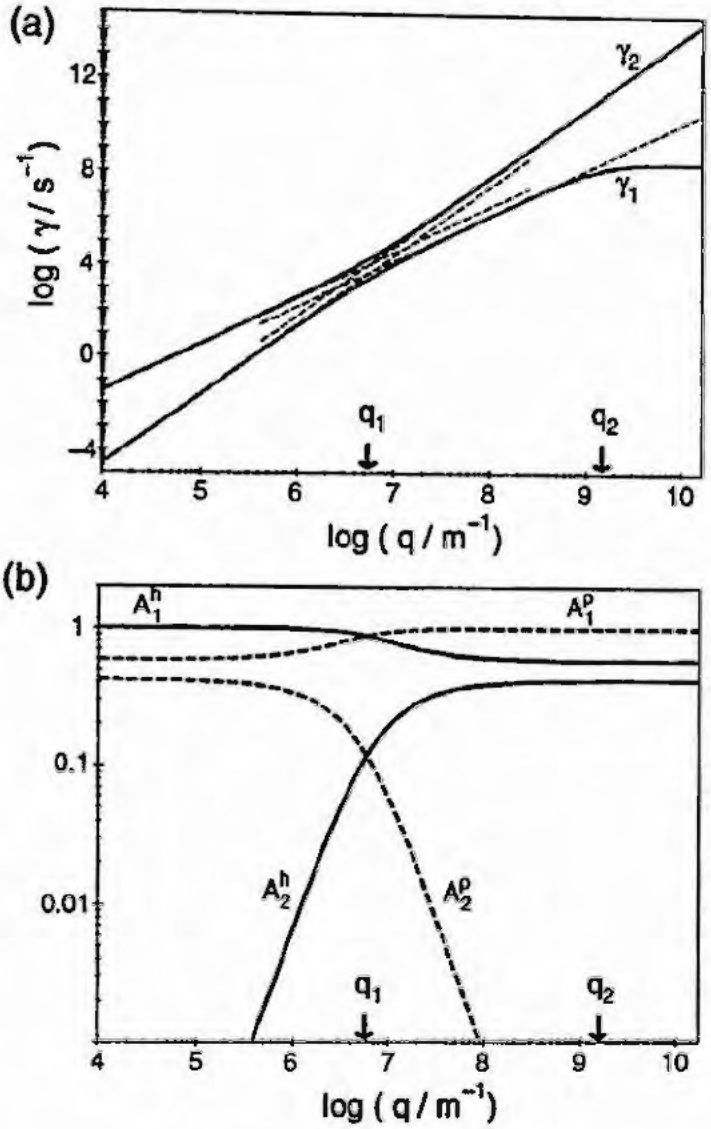

Figure 7.1: Dispersion relation (a) and amplitudes (b) for a free bilayer for $\kappa = 10^{-19}$ J, $k = 0.07$ J/m^2, $d = 1$ nm, $\eta = 10^{-3}$ J s/m^3, $\mu = 10^{-10}$ J s/m^2, and $b = 10^8$ J s/m^4; the thin dashed lines in (a) indicate the asymptotic behavior $\gamma_1 \approx \kappa q^3/4\eta$ and $\gamma_2 \approx kq^2/2b$, for small q; $\gamma_2 \approx \tilde{\kappa} q^3/4\eta$ and $\gamma_1 \approx kq^2\kappa/2b\tilde{\kappa}$, for large q, respectively. The ratio $\kappa/\tilde{\kappa} \simeq 0.417$ determines the asymptotic behavior of both the amplitudes A_2^p for small q and A_2^h for large q. (Kraus & Seifert, 1994).

(2.33). This effective high frequency rigidity differs from the low frequency rigidity κ because the densities cannot respond quickly to changes in shape. On time scales longer than $1/\gamma_2$, the height can relax so as to minimize the free energy for given density fluctuation. This

condition $\partial F/\partial h^*_{\mathbf{q}}\big|_{\rho_{\mathbf{q}}} = 0$ implies $h_{\mathbf{q}} = 2kd\rho_{\mathbf{q}}/\tilde{\kappa}q^2$, and therefore

$$\begin{aligned}\left\langle h_{\mathbf{q}}(t)h^*_{\mathbf{q}'}(0)\right\rangle \mathcal{N} &\approx \frac{4k^2d^2}{\tilde{\kappa}^2q^4}\left\langle \rho_{\mathbf{q}}(t)\rho^*_{\mathbf{q}'}(0)\right\rangle \mathcal{N} \approx \frac{4k^2d^2}{\tilde{\kappa}^2q^4}\frac{T\bar{\kappa}}{2k\kappa}\exp(-\gamma_1 t) \\ &= \left\langle h_{\mathbf{q}}h^*_{\mathbf{q}'}\right\rangle_0 \mathcal{N}\frac{2kd^2}{\tilde{\kappa}}\exp(-\gamma_1 t)\,, \end{aligned} \tag{7.38}$$

with $\mathcal{N} \equiv (2\pi)^2\delta(\mathbf{q}-\mathbf{q}')$. Thus, the coefficient $A_1^h(q)$ in the correlation function (7.36) is given by $A_1^h \approx 2kd^2/\tilde{\kappa}$, for $q \gg q_1$.

Finally, the slow mode γ_1 exhibits a second crossover at $q_2 \equiv \sqrt{2b/\mu}$, where the main dissipative mechanism changes from inter-monolayer friction to monolayer surface viscosity.

7.3.3 Experimental aspects

An important consequence of the results on the bilayer dynamics is that any experiment measuring $\langle h_{\mathbf{q}}(t)h_{\mathbf{q}}(0)\rangle$ should also pick up a contribution from the slow mode for $q > q_1$, provided it is sensitive to the time-scale $1/\gamma_1$. In particular, the slowest time-scale for shape fluctuations in this regime scales as q^{-2}, which differs form the q^{-3}-behavior of the classical model (7.25).

To estimate the crossover wavelengths q_1 below which the monolayer friction becomes relevant, we need a value for the friction coefficient b. This quantity, or more precisely the combination $4bd^2$ in our notation, has recently been measured by a nano-tether extrusion experiment for various lipids at different temperatures (Yeung, 1994). From the typical value $4bd^2 \simeq 2\times10^{-9}$J sec/m^2, one derives $b \simeq 5\times10^8$ J sec/m^4 with $d = 1$ nm. Using this value, one finds with $\kappa = 10^{-19}$ J, $\eta = 10^{-3}$ J sec/m^3, and $k = 10^2$ mJ/m^2, the crossover $q_1 \simeq 10^6$/m, corresponding to a wavelength of several microns, below which bilayer corrections to the dispersion relation for the bending mode should become important. For the second crossover, relevant only to the slower mode, we find $q_2 \simeq 1-3\times10^7$/cm, *i.e.*, a wavelength somewhat above the membrane thickness using $\mu \simeq 10^{-10}-10^{-9}$ J sec/m^2 derived from experiments using microfluorescence techniques (Merkel *et al.*, 1989).

Measurements of dynamical correlation functions in lipid bilayers have been performed in three different geometries (i) quasi-spherical vesicles (Engelhardt *et al.*, 1985; Bivas *et al.*, 1987) (ii) fluctuations of bound vesicles (Rädler, 1993) and (iii) scattering in multi-lamellar systems (Pfeiffer *et al.*, 1993). Even though the results derived above for the almost planar membrane do not carry over immediately to any of these geometries, the basic physical mechanism also applies to these situations.

For quasi-spherical vesicles, the calculations given above have to be repeated in spherical geometry. Within the classical model the result analogous to (7.25) has been derived in

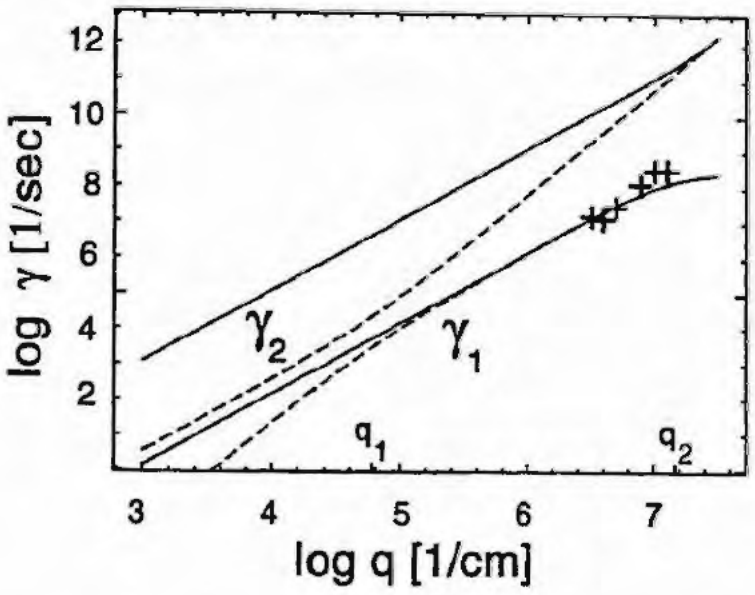

Figure 7.2: Dispersion relations for a single bilayer (dashed line) and a stack of bilayers (full line) for $\kappa = 10^{-12}$ erg, $k = 70$ mJ/m^2, $d = 1$ nm, $\eta = 0.001$ Jsec/m^3, $\mu = 10^{-10}$ J sec/cm^2, $b = 10^8$ J sec/m^4; and $l = 1$ nm for the stack. The marks are experimental data from (Pfeiffer *et al.*, 1993). (Seifert & Langer, 1993)

(Milner & Safran, 1987) while the bilayer dynamics in this geometry has been treated in (Yeung, 1994). However, the experimental resolution is presumably not yet sensitive enough to isolate the bilayer aspect for two reasons. First, only the first few modes have correlation times that are long enough to be recorded on video and second, the effective tension (4.59) enters as another unknown parameter in this geometry.

Dynamical light scattering on multi-layer systems (Nallet *et al.*, 1989) may become a more promising technique for verifying the effect of the bilayer structure in membrane dynamics. For a stack of swollen membranes and a wave-vector parallel to the sheets, the calculation of the dispersion relation for the collective undulation mode using the same force balance and boundary conditions at every membrane in a stack with repeat distance $2l$ leads to two modes, whose dispersion relation is shown in Fig. 7.2. For small q, both modes have a quadratic dispersion,

$$\gamma_1 \approx \frac{k}{2b}\frac{\kappa}{\tilde{\kappa}}q^2, \qquad \text{and} \qquad \gamma_2 \approx \frac{\tilde{\kappa}}{2\eta l}q^2. \tag{7.39}$$

Here, γ_2 corresponds to the undulation mode of a two component smectic (Brochard & de Gennes, 1975), which crosses over into the single layer result for $q \sim 1/l$. The damping rate of the second slow mode, γ_1, has the same dispersion as the single bilayer in the intermediate q regime.

The dispersion relation for γ_1 in the multi-layer system can be compared with a recent neutron reflection spin echo measurement of the undulations of swollen phospholipid multilayers (Pfeiffer *et al.*, 1993). In Fig. 7.2, we show these data obtained in the q range $0.3 - 1.2 \times 10^7$/cm. Even though the agreement with the theoretical results is good, more work will clearly be needed to prove that in this measurement the dissipation due to the bilayer aspect, as discussed here, has been observed. For a crucial experimental test, the damping rate as a function of the repeat distance $2l$ should be investigated. If the measured dispersion is indeed that of the frictional mode, the damping rate should be independent of the repeat distance, since the main dissipation for this mode occurs within the bilayer rather than in the liquid.

7.4 Dynamics of a bound fluid membrane

We now turn to the dynamics of a membrane interacting with a substrate through a potential $V(l)$ introduced in Sect. 6.1, to which we refer for definitions. For simplicity, we first describe the membrane within the classical model as an incompressible sheet. Modifications due to the bilayer structure will become important only beyond a cross-over vector q_1^a, to be determined later.

7.4.1 Hydrodynamics near a substrate

The hydrodynamics of the liquid surrounding the membrane is strongly affected by the presence of the wall. Since a membrane displacement with parallel wave vector q distorts the liquid flow field along a distance $1/q$ perpendicular to the membrane, the kinetic coefficient will deviate from its free value $\Gamma_0(q)$ whenever $q < 1/l_0$, where l_0 is the distance of the membrane from the wall. For optical measurements, the criterion $q < 1/l_0$ will typically be met.

The kinetic coefficient in this geometry can be obtained from the expression for the Oseen tensor (7.15) and (7.16). The total force density arising from the membrane and the wall is located at $z = l_0$ and $z = 0$, respectively. After a Fourier transformation parallel to the substrate, the total force density can thus be written as

$$\mathbf{K}_{\mathbf{q},z} \equiv \delta(z - l_0)[-\frac{\partial F_0^a}{\partial h_{\mathbf{q}}^*}\hat{\mathbf{z}} + K_{\mathbf{q}l}\hat{\mathbf{q}}] + \delta(z)[K_{\mathbf{q}z}^s\hat{\mathbf{z}} + K_{\mathbf{q}l}^s\hat{\mathbf{q}}]. \tag{7.40}$$

The first term is the normal force exerted by bending the membrane where F_0^a has been defined in (6.4). The latter three terms are the (yet unknown) force exerted by the membrane parallel to the plane, and the normal and the longitudinal force exerted by the substrate. If

this force density is inserted into Eqs. (7.15) and (7.16), the liquid flow field everywhere is obtained. The three unknown forces are determined through the following boundary conditions. First, both the normal and the longitudinal component of the velocity at the substrate have to vanish. Second, in the classical model, the membrane is incompressible, which implies that the in-plane divergence of the liquid flow at $z = l_0$ vanishes, i.e. $v_{\mathbf{q}l}(l_0) = 0$. The relationship between $v_{\mathbf{q}z}(l_0) = \partial_t h_{\mathbf{q}}$ and the normal force $-\partial F_0/\partial h_{\mathbf{q}}$ can then be written in the form

$$\partial_t h_{\mathbf{q}} = -\Gamma^a(q, l_0) E_0^a(q) h_{\mathbf{q}}, \tag{7.41}$$

where the energy $E_0^a(q)$ is given by Eq.(6.4).

The kinetic coefficient obeys the scaling form (Seifert, 1994a)

$$\Gamma^a(q, l_0) = \Gamma_0(q) \mathcal{G}(q l_0), \tag{7.42}$$

with the free kinetic coefficient $\Gamma_0(q)$ as defined in (7.23) and the scaling function

$$\mathcal{G}(x) \equiv 2 \frac{\sinh^2(q l_0) - (q l_0)^2}{\sinh^2(q l_0) - (q l_0)^2 + \sinh(q l_0)\cosh(q l_0) + (q l_0)} \to \begin{cases} x^3/3, & x \ll 1 \\ 1, & x \gg 1. \end{cases} \tag{7.43}$$

For $q \gg 1/l_0$, the asymptotic behavior of $\Gamma^a(q, l_0)$ deviates from its free value displaying the usual q^2-behavior for conserved quantities, the conserved quantity here being the volume of liquid between the membrane and the substrate.

7.4.2 Damping rate and correlation function

The $q-$dependence of the damping rate,

$$\gamma_0^a(q) \equiv \Gamma^a(q, l_0) E_0^a(q), \tag{7.44}$$

depends on several cross-over lengths scales arising from either the kinetic coefficient Γ^a or the energy E_0^a. In the low q-limit, one finds (Seifert, 1994a)

$$\gamma_0^a(q) \approx \Omega l_0^3 q^2/(12\eta), \quad q \ll \min[1/l_0, 1/\xi, 1/\xi_\Sigma], \tag{7.45}$$

independent of the tension and the rigidity of the membrane. With increasing q, the sequence of crossovers depends on the strength of the tension. We discuss explicitly only the case of weak tension, $\Sigma \ll 2\sqrt{\kappa\Omega}$, where the energy exhibits only one crossover length-scale at ξ defined in Eq.(6.5). Two cases must be distinguished (Seifert, 1994a):

(i) (monotonic damping) For $l_0 < \xi$, the intermediate behavior is given by

$$\gamma_0^a(q) \approx \kappa l_0^3 q^6/(12\eta), \quad 1/\xi \ll q \ll 1/l_0. \tag{7.46}$$

Such a q^6-behavior was first found in (Brochard & Lennon, 1975) as the low q limit of the bending fluctuations of two parallel membranes used as a crude model for fluctuations of red blood cells.[4]

(ii) (non-monotonic damping) For $\xi < l_0$, the q dependence becomes

$$\gamma_0^a(q) \approx \kappa/(4\eta\xi^4 q), \quad 1/l_0 \ll q \ll 1/\xi. \tag{7.47}$$

In this case, the damping rate *decreases* with increasing wave-vector (Seifert, 1994a). This unusual feature arises from the fact that the potential confines the mean square amplitudes $\langle h_{\mathbf{q}} h^*_{\mathbf{q}'} \rangle$ to the value $(T\xi^4/\kappa)(2\pi)^2\delta(\mathbf{q}-\mathbf{q}')$ independently of q, while the hydrodynamic damping becomes less effective with increasing q.

Finally, for large $q \gg \max[1/l_0, 1/\xi]$, the damping rate of the free membrane is recovered. In all regimes, the height-height correlation function is given by

$$< h_{\mathbf{q}}(t) h^*_{\mathbf{q}'}(0) >= \frac{T}{E_0^a(q)} e^{-\gamma_0^a(q)t}(2\pi)^2\delta(\mathbf{q}-\mathbf{q}'). \tag{7.48}$$

7.4.3 Dynamics of the unbinding transition: Illustrative Examples

In this section, we illustrate the results derived above with two examples. Each of them fits into one of the three regimes for the influence of *static* non-harmonic fluctuations which have to be distinguished for tensionless membranes as discussed in Sect. 6.1.3. In particular, we comment on the dynamic behavior at the unbinding transition where the separation l_0 becomes infinite (Lipowsky & Leibler, 1986; Mutz & Helfrich, 1989).

The mean field regime: Consider a charged membrane pushed by an osmotic pressure p towards a substrate. In weak electrolytes, where the screening length is large compared to l_0, fluctuations beyond the harmonic level can be safely ignored. The potential is then (Leibler & Lipowsky, 1987)

$$V(l) = A/l + pl, \tag{7.49}$$

where $A \equiv (\pi T/2l_B)$ (Israelachvili, 1991). Here, $l_B \simeq 0.7$ nm is the Bjerrum length in water and T the temperature (with Boltzmann's constant set to unity). One immediately gets $l_0 = (A/p)^{1/2}$ and $\xi = (\kappa/2A)^{1/4} l_0^{3/4}$. In the small q range, this implies that the damping rate $\gamma_0^a(q) \approx (A/6\eta)q^2$ does not depend on the mean separation l_0 for this potential. For an estimate of the typical time scales involved, we find $\gamma_0^a(q) \approx (10^{-5}\mathrm{cm}^2/\mathrm{sec})q^2$, using the typical values $\kappa \simeq 10^{-19}\mathrm{J} \simeq 25T$ for phospholipids and $\eta = 10^{-3}\mathrm{J\ sec/m}^3$ for water. For a wavelength $\lambda = 1\mu\mathrm{m} = 2\pi/q$, this becomes $\gamma_0^a(q) \simeq 6 \times 10^4/\mathrm{sec}$ which is too fast to be visible

[4] Brochard and Lennon's work has been extended in (Frey & Nelson, 1991), where the dynamics of two *polymerized* membranes is studied.

by video microscopy but will be accessible to dynamical light scattering. The criterion $l_0 > \xi$, implying non-monotonic damping, is met whenever $l_0 > \kappa l_B/\pi T \simeq 6$nm. Thus, the damping rate decreases with q in the range $1/l_0 < q < 1/\xi$ for unscreened electrostatic interactions (and, quite generally, for adhesion potentials which belong to the mean field regime). For $p \to 0$, which corresponds to the unbinding transition, l_0 becomes much larger than ξ. Thus, the two crossover wave-vectors, $1/l_0$ and $1/\xi$, in (7.47) scale differently at the unbinding transition, and the intermediate anomalous behavior of $\gamma_0^a(q)$ should be detectable.

The weak fluctuation regime: In stronger electrolytes, the electrostatic repulsion is screened and becomes exponential in l. Non-harmonic fluctuations can then no longer be neglected. The total potential becomes

$$V(l) = cT^2/\kappa l^2 + pl. \tag{7.50}$$

The equilibrium separation is given by $l_0 = (2c/p)^{1/3}T^{2/3}/\kappa^{1/3}$ and the relation between the correlation length $\xi = (\kappa/T)^{1/2}l_0/(6c)^{1/4} \simeq 3l_0$ and l_0 becomes independent of the amplitude p of the linear attractive potential. Since $\xi > l_0$, the weak fluctuation regime will always be governed by monotonic damping. Even for $p \to 0$ the intermediate behavior, $\gamma_0^a(q) \sim q^6$, will be confined to the rather narrow interval $1/3l_0 \lesssim q \lesssim 1/l_0$. For an estimate of the typical damping rates, assuming small q and taking $c = 1$, we get $\gamma_0^a(q) \approx (cT^2/2\eta\kappa)q^2/l_0 \simeq (10^{-13}\text{cm}^3/\text{sec})q^2/l_0$. For $l_0 = 50$nm and $\lambda = 2\mu$m, one obtains $\gamma_0^a(q) \simeq 10/\text{sec}$, which is below video frequency. Thus, these fluctuations will be accessible to micro-optical techniques.

The strong fluctuation regime: If both the attractive and the repulsive potential become short ranged, the non-harmonic fluctuations are so dominant that even the superposition of direct and steric interaction potentials fails to describe the interaction (Lipowsky & Leibler, 1986). However, the scaling behavior of the damping rate derived from (7.44) should still hold, provided one uses the fully renormalized l_0 and ξ.

7.4.4 Effect of bilayer architecture

So far, the membrane has been described within the classical model. We now discuss the modifications which arise if the bound membrane is treated as a bilayer consisting of compressible monolayers (Kraus & Seifert, 1994).

We start from the harmonic approximation where the energy for the bound bilayer is given, in analogy to the free membrane, by

$$F^a \equiv \frac{1}{2}\int \frac{d^2q}{(2\pi)^2}\,(h_{\mathbf{q}}, \rho_{\mathbf{q}}, \bar{\rho}_{\mathbf{q}}) \begin{pmatrix} \tilde{\kappa}q^4 + \Sigma q^2 + \Omega & -2kdq^2 & 0 \\ -2kdq^2 & 2k & 0 \\ 0 & 0 & 2k \end{pmatrix} \begin{pmatrix} h_{\mathbf{q}} \\ \rho_{\mathbf{q}} \\ \bar{\rho}_{\mathbf{q}} \end{pmatrix} . \tag{7.51}$$

No coupling between the lateral densities and the distance from the substrate is assumed here. If such a coupling arises from a more careful treatment of van der Waals interaction, it could be incorporated easily on the harmonic level.

The force density that enters the expressions (7.15) and (7.16) for the velocity field is now given by

$$\mathbf{K}_{\mathbf{q},z} \equiv \delta(z-l_0)[-\frac{\partial F^a}{\partial h^a_{\mathbf{q}}}\hat{\mathbf{z}} + (K^+_{\mathbf{q}l} + K^-_{\mathbf{q}l})\hat{\mathbf{q}}] + \delta(z)[K^s_{\mathbf{q}r}\hat{\mathbf{z}} + K^s_{\mathbf{q}l}\hat{\mathbf{q}}], \tag{7.52}$$

where the tangential force at the membrane is split into two parts. While the boundary condition for the velocity field at the substrate remains the same as above, the tangential velocities at the membrane have to match with the force balance within each monolayer, which is still given by (7.29). Solving these equations leads to the relaxational dynamics in the form

$$\frac{d}{dt}\begin{pmatrix} h_{\mathbf{q}} \\ \rho_{\mathbf{q}} \\ \bar{\rho}_{\mathbf{q}} \end{pmatrix} = -\mathbf{\Gamma}^a(q,l_0)\mathbf{E}^a(q)\begin{pmatrix} h_{\mathbf{q}} \\ \rho_{\mathbf{q}} \\ \bar{\rho}_{\mathbf{q}} \end{pmatrix}. \tag{7.53}$$

The quite lengthy explicit expression for the matrix of kinetic coefficients $\mathbf{\Gamma}^a(q,l_0)$ is given in (Kraus & Seifert, 1994). In this geometry, the average density $\bar{\rho}$ couples to both the shape and density difference variable due to the broken symmetry between upper and lower layer. In practice, however, the corresponding off-diagonal elements in $\mathbf{\Gamma}^a(q,l_0)$ are negligible and the physics can still be understood by considering only the variables h and ρ.

The detailed discussion of the dispersion relation and correlation functions given in (Kraus & Seifert, 1994) can be summarized as follows. The dispersion relation is made up by two modes with relaxation rates γ^a_1 and γ^a_2. Their values are given by $\gamma^a_1(q) \simeq \gamma^a_0(q)$ (as defined in (7.44)) and $\gamma^a_2(q) \simeq (k/2b)q^2$, except for $q > q^a_1$. The crossover vector q^a_1 is defined through the conditions that for all $q > q^a_1$ both of the following two conditions are met:

$$(i) \quad \gamma^a_0(q) > \frac{kq^2}{2b}. \tag{7.54}$$

If this inequality holds, the height fluctuations are faster than the lateral density relaxation. Therefore, the bending rigidity κ in $\gamma^a_0(q)$ gets renormalized to $\tilde{\kappa}$. This effect is relevant only if the height fluctuations are indeed governed by bending energy (rather than by the potential or the tension), i.e. only if

$$(ii) \quad q > \max[1/\xi, 1/\xi_\kappa]. \tag{7.55}$$

If this inequality holds, the height can adjust to density fluctuations which renormalizes the effective compressibility k for density difference fluctuations from k to $k(\kappa/\tilde{\kappa})$.

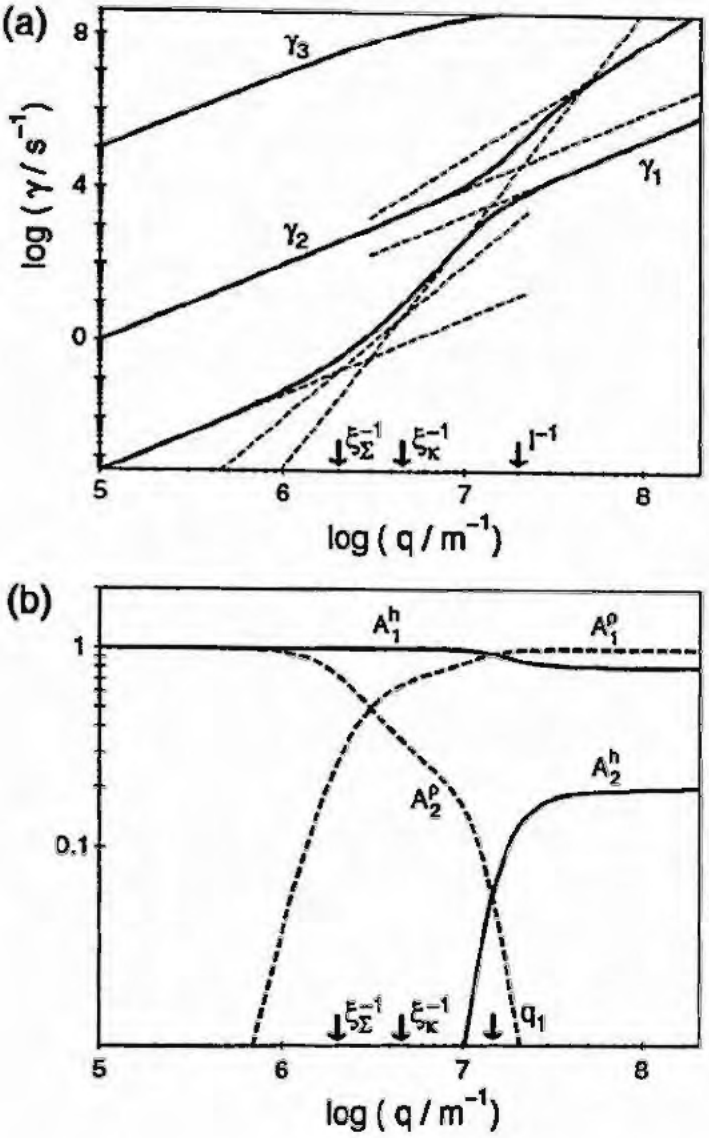

Figure 7.3: Dispersion relations (a) and amplitudes of the dynamic correlation functions (b) for a bound bilayer; case of weak adhesion and low tension. $\kappa = 0.5 \cdot 10^{-19}$ J, $k = 0.1$ J/m^2, $d = 1$ nm, $\eta = 10^{-3}$ J s/m^3, $\mu = 10^{-10}$ J s/m^2, $b = 5 \cdot 10^8$ J s/m^4, $\Omega = 4 \cdot 10^6$ J/m^4, $\Sigma = 10^{-6}$ J/m^2, and $l_0 = 50$ nm; The dashed lines indicate the asymptotic behavior in the various regimes, i.e. $kq^2/2b$ and $\tilde{\kappa}q^3/4\eta$ for γ_2; $\Omega l^3 q^2/12\eta$, $\Sigma l^3 q^4/12\eta$, $\kappa l^3 q^6/12\eta$, and $kq^2\kappa/2b\tilde{\kappa}$ for γ_1. The relaxation mode γ_3 of the average monolayer density $\bar{\rho}$ decays much faster. Parameters used here give $\kappa/\tilde{\kappa} \simeq 0.2$ for the large-q behavior of A_2^h. (Kraus & Seifert, 1994).

In particular, these results imply that the height-height correlation function for long times

behaves like

$$< h_{\mathbf{q}}(t) h^*_{\mathbf{q}'}(0) > \approx (2\pi)^2 \delta(\mathbf{q}-\mathbf{q}') \begin{cases} \dfrac{T}{E^a_0(q)} \exp\left(-\gamma^a_0(q)t\right) & q \ll \max[1/\xi, 1/\xi_\kappa] \\ \dfrac{2Tkd^2}{\tilde{\kappa}\kappa q^4} \exp\left(-\dfrac{k\kappa q^2}{2b\tilde{\kappa}}t\right) & q \gg \max[1/\xi, 1/\xi_\kappa], \end{cases} \quad (7.56)$$

where the prefactor of the large q regime follows from a calculation analogous to the one displayed in Eq.(7.38) for the free case.

For practical applications, the various cross-overs of the full dispersion relation may be close together and asymptotic expressions based on a single q behavior may be of little value for describing the data. This is shown explicitly in Fig. 7.3 in an example motivated by an experimental situation (Rädler, 1993). We consider a giant vesicle in weak adhesion with the fluctuating part facing the wall in an intermediate distance $l_0 \simeq 50$ nm. Tension in such a case is small. The curvature of the potential can be estimated via $\Omega = \kappa \xi_{ex}^{-4}$ (or $\Omega = \Sigma \xi_{ex}^{-2}$) from the measured real-space correlation length ξ_{ex} of height fluctuations, which was found to be of the order 0.5 μm. The remaining material parameters can be found in the figure caption.

Full dispersion relations like the one shown in Fig. 7.3 should provide the basis for analysis of experimental measurements of the fluctuations of bound membranes. Even though at present the experimental data are not yet comprehensive enough for a detailed comparison, the potential of such measurements for a quantitative analysis of membrane interaction and dynamics is evident.

Chapter 8

Lipid mixtures

Single-component membranes have been the topic in the previous chapters. The lipid bilayer of biomembranes, however, is composed of different types of molecules which may differ in their head groups, in the length of their hydrocarbon chains or in the number of unsaturated bonds within these chains. In such a multi–component system, the composition can become laterally inhomogeneous within each monolayer and can be different across the two monolayers. As a result, an inhomogeneous spontaneous curvature is created which leads to a coupling between the composition and the shape (Gruler, 1975; Gebhardt *et al.*, 1977; Leibler, 1986; Leibler & Andelman, 1987). Moreover, there are energies associated with composition variables such as the entropy of mixing and the cost of an inhomogeneous composition profile.

As a first step towards the modelling of multi-component membranes, we consider in this Chapter a two-component membrane. Quite generally, one can distinguish two cases for the phase behavior of such a membrane: (i) a homogeneous one–phase region at high temperature and (ii) a two–phase coexistence region at lower temperatures for a certain range of compositions.

In the two-phase region, domains of one phase in the surrounding matrix of the other phase are formed. The edges of these domains are characterized by an edge or line tension. Since the length of the domain boundary decreases if the domain buds, the competition between this edge tension and the curvature energy leads to *domain-induced budding* as soon as the domain reaches a critical size (Lipowsky, 1992; Lipowsky, 1993; Jülicher & Lipowsky, 1993). A related phenomena is the occurrence of striped or modulated phases investigated mainly for two-dimensional vesicles in (Markin, 1981; Andelman *et al.*, 1992; Kawakatsu *et al.*, 1993).

In the one–phase region, the ground state in the absence of a spontaneous curvature is a flat and laterally homogeneous membrane. However, any inhomogeneity in the compo-

sition, either laterally within a monolayer or between the two monolayers, induces a local spontaneous curvature if the two lipid species have a different molecular geometry. For an almost planar membrane, this leads to a coupling between bending fluctuations and composition fluctuations which decreases the bending rigidity (Leibler, 1986; Leibler & Andelman, 1987). For a non-spherical vesicle, this coupling between shape and composition causes *curvature-induced lateral phase segregation* (Seifert, 1993), as discussed in Sect. 8.1.

Experimental investigations of the phase diagram have shown that a two-component membrane in the fluid state often exhibits a homogeneous phase. By decreasing the temperature, before reaching a critical point the gel state intervenes which then coexists with a homogeneous fluid phase. Genuine fluid-fluid coexistence, however, has been found for a few examples. An especially important one is provided by mixtures of phospholipids and cholesterol, as has been established quite recently (Needham *et al.*, 1988; Vist & Davis, 1990; Bloom *et al.*, 1991). Fluid-fluid coexistence also occurs in the binary mixture of DEPC and DPPE (Wu & McConnell, 1975) and in mixtures with partially unsaturated alkyl chains (Bloom, 1992).

8.1 Curvature-induced lateral phase segregation

Even if a flat membrane is in a laterally homogeneous state, the shape transformation of the closed vesicle can induce phase segregation within the membrane (Seifert, 1993). For an initially spherical vesicle, a temperature increase leads to deviations from the spherical shape and, thus, to a position–dependent curvature, which induces a position–dependent composition.

8.1.1 Coupling between composition and shape

For a quantitative description, the composition (area fractions) of lipid A in the individual monolayers $x_A^i (= 1 - x_B^i)$ $(i = in, out)$ and deviations $\delta x_A^i(s_1, s_2) \equiv x_A^i(s_1, s_2) - \bar{x}_A$, from the mean value $\bar{x}_A$ are introduced. If the local deviation is different in the two monolayers, a local spontaneous curvature is induced according to

$$C_0(s_1, s_2) = \lambda(\delta x_A^{out}(s_1, s_2) - \delta x_A^{in}(s_1, s_2)) + \bar{C}_0 \equiv \lambda\phi(s_1, s_2) + \bar{C}_0, \qquad (8.1)$$

where the phenomenological coupling constant λ has the dimensions of an inverse length (Leibler, 1986). A systematic spontaneous curvature $\bar{C}_0$ arises if the mean compositions $\bar{x}_A^i$ are different in the two monolayers, as it applies to spontaneous formation of small vesicles in mixtures of oppositely charged surfactants where phase separation occurs across the membrane (Kaler *et al.*, 1989; Safran *et al.*, 1990; Safran *et al.*, 1991; Kaler *et al.*, 1992).

8.1.2 Energy of a two-component vesicle

The bending energy, F_1, of the two-component vesicle is then chosen as a generalization of the bending energy of a single-component vesicle, as given by (2.50). This leads to (Seifert, 1993)

$$F_1 = \kappa \left(\oint dA \, \frac{1}{2} (2H(s_1, s_2) - C_0(\phi(s_1, s_2))^2 + \frac{\alpha\pi}{8Ad^2}(\Delta A - \Delta A_0)^2 \right). \tag{8.2}$$

For simplicity, it is assumed that neither the bending rigidities κ and $\alpha\kappa$ nor the area of the vesicle, A, and area-difference ΔA_0 depend on the composition.

Since the membrane does not show genuine phase separation, there is a free energy associated with the deviation of the composition from its mean value. For small deviations, this energy can be written in the form

$$F_2 = \frac{\kappa}{2}\epsilon \oint dA \left(\phi^2 + (\xi_c \nabla \phi)^2 \right). \tag{8.3}$$

Here, ξ_c is the correlation length for composition fluctuations, ∇ is the covariant gradient operator and ϵ is a molecular energy, estimated in Sect. 8.1.3 below, divided by the bending rigidity.

Since the typical length-scale for shape variations of large vesicles is in the micrometer-range, while the typical correlation length ξ_c will be of the order of nanometers, the gradient term in F_2 will be, in general, much smaller than the ϕ^2-term and, thus, can be ignored. If the exchange of molecules between the two layers is forbidden, the total energy,

$$F \equiv F_1 + F_2, \tag{8.4}$$

has to be minimized under the constraint $\oint dA\phi = 0$. The composition profile $\phi(s_1, s_2)$, then becomes

$$\phi(s_1, s_2) = \frac{2\lambda}{\lambda^2 + \epsilon} \left(H(s_1, s_2) - \frac{\Delta A}{4dA} \right), \tag{8.5}$$

which shows that the local composition follows the deviation of the mean curvature $H(s_1, s_2)$ from its average value $\Delta A/(4dA)$. After inserting (8.5) into F, the total energy can be written as (Seifert, 1993)

$$F = \kappa_{\text{eff}} \left(G + \frac{\alpha_{\text{eff}}\pi}{8Ad^2}(\Delta A - \Delta A_{0,\text{eff}})^2 + \text{const} \right). \tag{8.6}$$

This expression is the standard form of the bending energy of a single-component vesicle in the ADE model (2.50) in which the three model parameters have been renormalized. First, the effective bending rigidity is

$$\kappa_{\text{eff}} \equiv \frac{\kappa\epsilon}{\epsilon + \lambda^2} < \kappa. \tag{8.7}$$

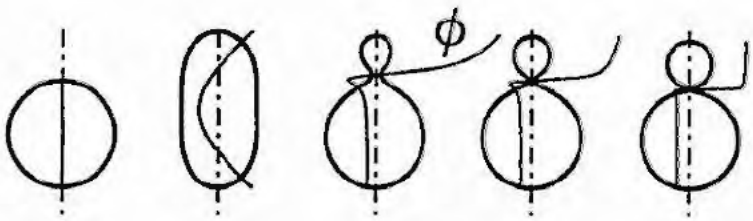

Figure 8.1: Evolution of a spherical vesicle as the reduced volume v changes due to an increase in temperature for $\bar{C}_0 = 0, \alpha = 1, \alpha_{\rm eff} = 2$, and $\Delta A_0(v = 1)/(16\pi dR) = 1.7$. The thin curves show the composition ϕ. The dashed-dotted lines correspond to $\phi = 0$. The reduced volumes are $v = 1.0, 0.89, 0.89, 0.86$, and 0.82 from left to right. At $v = 0.89$, the symmetric and the asymmetric shape have the same energy, indicating a discontinuous budding transition. The vesiculation line is reached with the last shape. (Seifert, 1993).

Thus, the bending rigidity decreases for a two-component system, as has been derived for almost planar membranes before (Leibler, 1986). Secondly, the non-local term becomes more relevant for stronger couplings since the non–local bending rigidity is renormalized according to

$$\alpha_{\rm eff} \equiv \alpha + (\lambda^2/\epsilon)(1 + 1/\pi) > \alpha. \tag{8.8}$$

Finally, the renormalized equilibrium area difference is

$$\Delta A_{0,\rm eff} \equiv \frac{\epsilon + \lambda^2}{\epsilon \alpha_{\rm eff}} \left(\frac{2\bar{C}_0 dA}{\pi} + \alpha \Delta A_0 \right) \tag{8.9}$$

Once this mapping has been obtained, both the knowledge of the phase diagram of the area-difference elasticity model and shape calculations within this models can be used to obtain results for the two-component system. As an illustrative example, consider the thermal evolution of an initially spherical vesicle (with a homogeneous composition profile $\phi(s) = 0$) with increasing temperature as shown in Fig. 8.1. It is assumed that the thermal trajectory is still given by Eq. (3.12) with $r = 1$. With increasing temperature, the reduced volume decreases and the shape becomes more prolate. The inhomogeneous curvature then induces a non-trivial composition profile along the contour. In the outer monolayer, the A molecules are enriched at the poles (if their enhancement in the outer layer leads to a positive spontaneous curvature, i.e., if $\lambda > 0$) while the B lipids are enriched along the equatorial region of the vesicle. For smaller v, the up/down asymmetric shapes have lower

energy leading to a discontinuous budding transition. These shapes finally end up at the vesiculation point. In the vesiculated state, the composition within each sphere becomes homogeneous again with all the variation of the composition occurring in the neck. Thus, the shape change, i.e., in this case budding and vesiculation, leads to phase segregation. Moreover, the formation of smaller buds is more favorable in the two-component system than in the pure system under the same conditions (Seifert, 1993).

8.1.3 Estimates and experiments

A crude estimate for the magnitude of the curvature-induced phase segregation can be obtained as follows (Seifert, 1993). Assume the lipid A has a cone-like shape with a radius of curvature R_A while lipid B has a cylindrical shape. The coupling constant λ is then of the order of $1/R_A$. Since R_A is determined by typical molecular dimensions, we will use $\lambda = 1/10\text{nm}$ for a conservative estimate. For the free energy density coefficient ϵ, one estimates $\epsilon \simeq \tau T/\kappa a^2$ where $a \simeq 1$ nm is a molecular length. The reduced temperature $\tau \equiv (T - T_C)/T_C$ is the distance to the A-B critical point that separates the one-phase region from the two-phase coexistence region of the lipid mixture. For a mixture of DEPC and DPPE, this critical point is at $T_c \simeq 340K$ according to (Wu & McConnell, 1975). For a vesicle at a temperature of 10 centigrades above T_c, $\tau \simeq 0.03$ which leads with $T/\kappa \simeq 1/25$ to $\phi \simeq 20(H - \Delta A/(4dA))$nm. With $(H - \Delta A/(4dA)) \simeq 1/R_0$, where R_0 is the radius of the vesicle, the typical variation in the composition becomes of the order of 1% for vesicles with a radius $R_0 \simeq 1$ μm but 10% for $R_0 \simeq$ 100 nm. The smaller the vesicles are the larger becomes the phase segregation.

Very close to the critical point, the argument given above that the correlation length is small compared with the size of the vesicle is no longer valid. In fact, using $\xi \simeq a/\tau^\nu$, where $a \simeq 1$ nm and $\nu = 1$ is the critical exponent of the two-dimensional Ising model, one obtains $\tau_* \simeq a/R_0$ as a crossover temperature. For $\tau \lesssim \tau_*$, the gradient term in F_2 can no longer be neglected. Within mean-field theory, the shape of two-component vesicles has been investigated in (Taniguchi *et al.*, 1994) in the vicinity of a demixing transition.

Even though there are a few experiments on shape transformations of multi-component vesicles (Farge & Devaux, 1992), the interaction between local composition and the shape transformation has not yet been systematically studied. For such a comparison between theory and experiment, one should, e.g., analyse the composition of the bud and compare it with the composition of the mother vesicle. The experimental observation that budding can be followed by fission in a multicomponent membrane (Döbereiner *et al.*, 1993) may help to achieve this challenging task.

Chapter 9

Concluding perspective

The theory of conformations of fluid membranes and vesicles presented in this treatise started from a continuum description based on two relevant degrees of freedom: the local shape, and the local density difference in the two monolayers. Energy minimization, taking into account the geometrical constraints, yields a variety of shapes of various topologies. These shapes are arranged into phase diagrams which separate phases of different symmetry. For vesicles of higher genus, this approach culminates in the prediction of conformal diffusion which amounts to a one-fold continuous degeneracy of the ground state. For bound vesicles and vesicles consisting of two components, an additional energy enters the minimization, which leads to the prediction of a curvature-driven adhesion transition and curvature-induced lateral phase segregation, respectively.

The non-trivial aspect of the simple minimization of energies arises from the closed topology of the vesicles. On a smaller length-scale, the membrane can be considered as almost planar. The topological closure can then be subsumed into an effective tension, the role of which became clear in the theory of Gaussian fluctuations around the mean shapes. For an almost planar membrane, the theory was developed further to include dynamical fluctuations of free and bound membranes.

Experimentally, several of the phenomena described here have already been observed. The variety of shapes of spherical topology has, in fact, been a main motivation for this work. Conformal diffusion of vesicles of higher genus has been verified experimentally. On a quantitative level, detailed experiments on the shape of vesicles are feasible although quite challenging, since the observables have to be obtained from image analysis of contours which are affected by Brownian rotation. Still, the quantitative theoretical predictions contained in the phase diagrams should be accessible to experimental verification. On the other hand, a close comparison of observed shapes with theoretically calculated shapes could yield an independent determination of material parameters such as the rigidity ratio α. Significant

progress in quantitative experiments is involving bound membranes that are part of large adhering vesicles. In this geometry, dynamical fluctuations are experimentally accessible the analysis of which should lead to insight into dissipative mechanisms within the membrane in the near future.

Alluding again to the three fields mentioned in the introduction that merge in motivating work on membranes, the following subjective perspective presents areas of research related to the approach discussed in this paper. With regards to the chemical physics aspect, a better understanding of how the molecular architecture and interactions determine the basic material parameters such as the bending rigidities, which enter the continuum theory, is necessary.[1] For mixed vesicles, the phenomenological parameters that occur in energy terms like (8.2) and (8.3) should also be derived from the molecular constituents. Likewise, a sensible theory of membrane rupture presumably has to be built on some non-trivial properties of cohesion of the membrane on a molecular scale and the presence of water molecules will have to be taken into account.

As to statistical mechanics, most of the work presented here can be characterized as a study of the low temperature equilibrium properties of a fluid membrane without internal degrees of freedom. The theory of Gaussian fluctuations presents a first step towards the regime where entropy becomes a determining factor. Nonlinear fluctuations will also become important close to any shape transition, as well as at higher temperatures where Monte Carlo simulations of vesicles various phases such as the branched-polymer and an inflated phase with unusual scaling properties[2]. At higher temperatures, it will also be particularly interesting to allow for topology changing conformations (Boal & Rao, 1992).

Several extensions of the present approach arise from either coupling the membrane to "external fields", or decorating the membrane with "internal degrees of freedom". An example for the former is given by membranes and vesicles in electric fields[3] or the deformation of vesicles in stationary flow (Gompper & Kroll, 1993). A paradigmatic case for an internal degree of freedom has been discussed in the chapter on lipid mixtures for which the composition can be considered as a scalar field living on the membrane. Along a similar line, one can investigate a vector order parameter on the membrane, which behaves differently depending on the genus of the surface (MacKintosh & Lubensky, 1991; Lubensky & Prost, 1992). If

[1] One approach to relate microscopic with mesoscopic properties is reviewed in (Ben-Shaul, 1994).

[2] (Ho & Baumgärtner, 1990; Kroll & Gompper, 1992; Gompper & Kroll, 1992; Gompper & Kroll, 1994)

[3] Membranes in electric fields have been intensively studied, even though not very well understood; however, work on the geometrical aspects of vesicles in moderate fields is scarce. Small fields lead to deformations of vesicles as studied in (Bryant & Wolfe, 1987; Kummrow & Helfrich, 1991; Hyuga *et al.*, 1991a; Hyuga *et al.*, 1991b; Peterson, 1992). Strong fields lead to electroporation of the membrane (Crowley, 1973; Dimitrov, 1984; Winterhalter & Helfrich, 1987; Needham & Hochmuth, 1989), and electrofusion of vesicles and cells, as reviewed in (Zimmermann, 1982; Neumann *et al.*, 1989; Chang *et al.*, 1992).

the membrane is decorated with large impurities, thermal fluctuations of the membrane can lead to long-range interaction among them (Goulian *et al.*, 1993; Palmer *et al.*, 1994).

For polymerized, solid or "tethered" membranes with fixed connectivity, which can sustain shear, the in-plane displacements, i.e. the "phonons", are internal degrees of freedom which are coupled to the bending modes (Landau & Lifshitz, 1989). This coupling leads to a scale-dependent effective bending rigidity (Nelson & Peliti, 1987; Nelson, 1988). Solid or polymerized membranes are stiffer than fluid ones as can be seen in the microscope: if vesicles are cooled below the chain-melting transition, their flickering is substantially reduced.

With the red blood cell, biology again provides a main motivation for the study of polymerized membranes. Apart from the fluid lipid bilayer, the plasma membrane of a red blood cell contains a network of spectrin tetramers linked together at junctional complexes which forms a quasi-hexagonal structure attached to the bilayer by integral membrane proteins (Alberts *et al.*, 1989). The spectrin network can be isolated by dissolving the lipid with detergents. It then no longer exhibits the typical biconcave shape of the red blood cell but rather becomes nearly spherical. Its morphological and elastic properties can be studied if the skeletons are suspended with optical tweezers in a flow chamber (Svoboda *et al.*, 1992). Likewise, X-ray diffraction as well as light scattering (Schmidt *et al.*, 1993) probe the structural properties of this network.

For the compound red blood cell membrane, the presence of the network poses a conceptual problem for the calculation of shapes since it is not yet clear to which extent the network contributes to the stability of the shape. In fact, we have seen that even for lipid vesicles a discocyte shape minimizes the curvature energy in an appropriate range of the reduced volume. Thus, in the absence of external forces, the shape of the red blood cell could be controlled primarily by the bending elasticity of the bilayer together with the osmotic conditions, while the cytoskeleton is used to recover this shape after deformations of the cell shape. On the other hand, it is known that dissolving the network from the bilayer results in spontaneous budding of small vesicles. Thus, it seems that the network is relevant in stabilizing the red blood cell lipid membrane with its specific composition (Steck, 1989).

Evidence for a presumably subtle interplay between network and bilayer also arises from measurements of the elastic properties of the red blood cell membrane and, in particular, from its shear modulus which seems to be strongly scale-dependent. On large scales, deformation in the micro-pipet (Waugh & Evans, 1979) as well as deformation induced by an electric field (Engelhardt & Sackmann, 1988) yield a shear modulus which is one order of magnitude larger than the one obtained from the analysis of the thickness fluctuations by flicker spectroscopy, which probes smaller scales (Strey, 1993). The origin of this discrepancy is not yet understood. In general, the flickering of a compound membrane such as

the plasma membrane of red blood cells should exhibit a crossover scale below which shape fluctuations are fluid-like whereas the finite shear modulus of the network only affects the large fluctuations (Lipowsky & Girardet, 1990; Komura & Lipowsky, 1992).

A comprehensive theoretical model for the red blood cell membrane has not yet emerged. Steps in such a direction are provided by a continuum theory in which the network is modeled as an ionic gel (Stokke *et al.*, 1986a; Stokke *et al.*, 1986b), as well as by recent computer simulations (Boal *et al.*, 1992; Boal, 1994). The analysis of these models shows a sensitive dependence of the shear modulus on the properties of the spectrin tethers. For an understanding of the red blood cell membrane, concepts from polymer physics and membrane physics thus have to merge.

These few remarks on the red blood cell, the quest for whose understanding marks one of the starting points of the research on vesicles, suffice to show the continuing inspiration biology brings to physics. Based on the experience acquired in comprehending vesicle conformations as described in this treatise, the study of these more complicated systems is anticipated to reveal more fascinating surprises in the near future.

Acknowledgments

I am indebted to Reinhard Lipowsky for introducing me to this field, for an enjoyable collaboration and innumerable discussions on various aspects of the physics of membranes, and for generous support both in his group at the University in Munich where the work reported here has been started and at the IFF in Jülich where it has been finished.

I am most grateful to Michael Wortis both for giving me the chance to work in his group during two very enjoyable years at the Simon Fraser University in Vancouver and for many thoughtful conversations and a pleasant collaboration.

Erich Sackmann organized the "Sonderforschungsbereich" in Munich without which this work would never have been nucleated. I am indebted to him not only for creating this most stimulating forum but also for many inspiring discussion and a fruitful collaboration.

Karin Berndl, Frank Jülicher, Martin Kraus, Ling Miao, and Marija Nikolic contributed with their thesis works substantially to various parts reported here. I am grateful to all of them as well as to Steve Langer for an enjoyable collaboration.

Discussions and collaboration with the experimentalists Hans-Günther Döbereiner, Willi Fenzl, Josef Käs, Xavier Michalet, and Joachim Rädler have been most stimulating.

Evan Evans and Wolfgang Helfrich have always been generous in sharing with me the wealth of their life-long experience with these systems.

I benefitted from correspondence, discussions and collaboration with many more colleagues. In particular, I would like to mention D. Andelman, D. Bensimon, B. Duplantier, M. Bloom, D. Boal, R. Bruinsma, M. Cates, G. Cevc, B. Fourcade, T. Fischer, G. Forgacs, C. Goh, G. Gompper, J. Goos, W. Häckl, S. Hyde, H. Kleinert, B. Klösgen, S. König, D. Kroll, J. Krug, R. Kusner, D. Langevin, M. Lässig, T. Lubensky, F. MacKintosh, K. Mecke, D. Morse, P. Nelson, G. Oster, A. Parsegian, M. Peterson, P. Pincus, R. Podgornik, J. Prost, S. Ramaswamy, M. Rao, D. Richter, W. Schnitzler, J. Shillcock, T. Steck, S. Svetina, H. Strey, A. Yeung, B. Zeks, A. Zilker, U. Zimmermann, and M. Zuckermann.

I am most grateful to Cynthia Goh and Steve Langer for critically reading through this paper and trying to improve the english. The remaining imperfections are entirely mine.

Last, but not least, I want to express my sincere thanks to Herbert Wagner, both for showing me how fascinating a topic statistical physics is when I was a student and for guidance and support on various stages of my career since then.

References

Alberts, B., Bray, D., Lewis, J., Raff, M., Roberts, K., & Watson, J.D. 1989. *Molecular biology of the cell.* second edn. New York: Garland.

Andelman, D., Kawakatsu, T., & Kawasaki, K. 1992. Equilibrium Shape of Two-Component Unilamellar Membranes and Vesicles. *Europhys. Lett.*, **19**, 57–62.

Backer, J.M., & Dawidowicz, E.A. 1981. Transmembrane Movement of Cholesterol in Small Unilamellar Vesicles Detected by Cholesterol Oxidase. *J. Biol. Chem.*, **256**, 586–588.

Bailey, S.M., Chiruvolu, S., Israelachvili, J.N., & Zasadzinski, J.A.N. 1990. Measurements of Forces involved in vesicle adhesion using freeze–fracture electron microscopy. *Langmuir*, **6**, 1326–1329.

Ben-Shaul, A. 1994. Molecular Theory of Chain Packing, Elasticity and Lipid–Protein Interaction in Lipid Bilayers. *In:* Lipowsky, R., & Sackmann, E. (eds), *Structure and Dynamics of Membranes.* Amsterdam: Elsevier Science.

Berndl, K. 1990. *Formen von Vesikeln.* Diplomarbeit, Ludwig-Maximilians-Universität München (1990).

Berndl, K., Käs, J., Lipowsky, R., Sackmann, E., & Seifert, U. 1990. Shape Transformations of Giant Vesicles: Extreme Sensitivity to Bilayer Asymmetry. *Europhys. Lett.*, **13**, 659–664.

Beysens, D., Boccara, N., & Forgacs, G. (eds). 1991. *Dynamical Phenomena at Interfaces, Surfaces and Membranes.* New York: Nova Science.

Bivas, I., Hanusse, P., Bothorel, P., Lalanne, J., & Aguerre-Chariol, O. 1987. An Application of the Optical Microscopy to the Determination of the Curvature Elastic Modulus of Biological and Model Membranes. *J. Phys.*, **48**, 855–867.

Bivas, I., Bivolarski, L., Mitov, M.D., & Derzhanski, A. 1992. Correlations Between the Form Fluctuations Modes of Flaccid Quasispherical Lipid Vesicles and their Role in

the Calculation of the Curvature Elastic Modulus of the Vesicle Membrane. Numerical Results. *J. Phys. II*, **12**, 1423–1438.

Bloom, M. 1992. The physics of soft, natural materials. *Physics in Canada*, **48**, No.1,7–16.

Bloom, M., Evans, E., & Mouritsen, O.G. 1991. Physical Properties of the Fluid Lipid-Bilayer Component of Cell Membranes: A Perspective. *Quart. Rev. Biophys.*, **24**, 293–397.

Boal, D.H. 1994. *Computer Simulation of a Model Network for the Erythrocyte Cytoskeleton.* preprint.

Boal, D.H., & Rao, M. 1992. Topology changes in fluid membranes. *Phys. Rev. A*, **46**, 3037–3045.

Boal, D.H., Seifert, U., & Zilker, A. 1992. Dual Network Model for Red Blood Cell Membranes. *Phys. Rev. Lett.*, **69**, 3405–3408.

Boroske, E., Elwenspoek, M., & Helfrich, W. 1981. Osmotic Shrinkage of Giant Egg-Lecithin Vesicles. *Biophys. J.*, **34**, 95–109.

Bozic, B., Svetina, S., Zeks, B., & Waugh, R.E. 1992. Role of lamellar membrane structure in tether formation from bilayer vesicles. *Biophys. J.*, **61**, 963–973.

Brakke, K.A. 1992. The Surface Evolver. *Experimental Mathematics*, **1**, 141–165.

Brochard, F., & de Gennes, P.G. 1975. Hydrodynamic Properties of Fluid Lamellar Phases of Lipid/Water. *Pramana*, **1**, 1–21.

Brochard, F., & Lennon, J.F. 1975. Frequency Spectrum of the Flicker Phenomenon in Erythrocytes. *J. Physique*, **36**, 1035–1047.

Bruinsma, R. 1991. Growth Instabilities of Vesicles. *J. Phys. II France*, **1**, 995–1012.

Bryant, G., & Wolfe, J. 1987. Electromechanical Stresses Produced in the Plasma Membranes of Suspended Cells by Applied Electric Fields. *J. Membrane Biol.*, **96**, 129–139.

Bryant, R. 1984. A duality theorem for Willmore surfaces. *J. Differential Geom.*, **20**, 23–53.

Cai, W., & Lubensky, T.C. 1994. Covariant Hydrodynamics of Fluid Membranes. *Phys. Rev. Lett.*, **73**, 1186–1189.

Cai, W., Lubensky, T.C., Nelson, P., & Powers, T. 1994. Measure factors, tension, and correlations of fluid membranes. *J. Phys. II France*, **4**, 931–949.

Canham, P.B. 1970. The Minimum Energy of Bending as a Possible Explanation of the Biconcave Shape of the Human Red Blood Cell. *J. Theoret. Biol.*, **26**, 61–81.

Cevc, G. 1994. Material Transport Across permeability barriers by means of lipid vesicles. *In:* Lipowsky, R., & Sackmann, E. (eds), *Structure and Dynamics of Membranes.* Amsterdam: Elsevier Science.

Cevc, G., & Marsh, D. 1987. *Phospholipid Bilayers: Physical Principles and Models.* New York: Wiley.

Cevc, G., Fenzl, W., & Sigl, L. 1990. Surface–Induced X–Ray Reflection Visualization of Membrane Orientation and Fusion into Multibilayers. *Science*, **249**, 1161–1163.

Chang, D.C., Chassy, B.M., Saunders, J.A., & Sowers, A.E. 1992. *Guide to Electroporation and Electrofusion.* San Diego: Academemic Press, Inc.

Crowley, J.M. 1973. Electrical breakdown of bimolecular lipid membranes as an electromechanical instability. *Biophys. J.*, **13**, 711–724.

David, F., & Leibler, S. 1991. Vanishing tension of fluctuating membranes. *J. Phys. II France*, **1**, 959–976.

de Gennes, P.-G., & Taupin, C. 1982. Microemulsions and the flexibility of oil/water interfaces. *J. Phys. Chem.*, **86**, 2294–2304.

de Loof, H., Harvey, S.C., Segrest, J.P., & Pastor, R.W. 1991. Mean field stochastic boundary molecular dynamics simulation of a phospholipid in a membrane. *Biochemistry*, **30**, 2099–2113.

Deuling, H.J., & Helfrich, W. 1976. The Curvature Elasticity of Fluid Membranes: A Catalogue of Vesicle Shapes. *J. Physique*, **37**, 1335–1345.

Dimitrov, D.S. 1984. Electric Field–Induced Breakdown of Lipid Bilayers and Cell Membranes: A thin Viscoelastic film model. *J. Membrane Biol.*, **78**, 53–60.

do Carmo, M.P. 1976. *Differential Geometry of Curves and Surfaces.* New Jersey: Prentice–Hall.

Döbereiner, H.-G. private communication.

Döbereiner, H.-G., Käs, J., Noppl, D., Sprenger, I., & Sackmann, E. 1993. Budding and Fission of Vesicles. *Biophys. J.*, **65**, 1396–1403.

Doi, M., & Edwards, S.F. 1986. *The Theory of polymer dynamics.* Oxford: Clarendon Press.

Duplantier, B. 1990. Exact Curvature Energies of Charged Membranes of Arbitrary Shapes. *Physica A*, **168**, 179–197.

Duplantier, B., Goldstein, R.E., Romero-Rochin, V., & Pesci, A.I. 1990. Geometrical and Topological Aspects of Electric Double Layers near Curved Surfaces. *Phys. Rev. Lett.*, **65**, 508–511.

Duwe, H.P., Käs, J., & Sackmann, E. 1990. Bending Elastic Moduli of Lipid Bilayers: Modulation by Solutes. *J. Phys. France*, **51**, 945–962.

Engelhardt, H., & Sackmann, E. 1988. On the Measurement of Shear Elastic Moduli and Viscosities of Erythrocyte Plasma Membranes by Transient Deformation in High Frequency Electric Fields. *Biophys. J.*, **54**, 495–508.

Engelhardt, H., Duwe, H.P., & Sackmann, E. 1985. Bilayer Bending Elasticity Measured by Fourier Analysis of Thermally Excited Surface Undulations of Flaccid Vesicles. *J. Physique Lett.*, **46**, L 395–L 400.

Evans, E. 1990. Adhesion of Surfactant–Membrane Covered Droplets: Special Features and Curvature Elasticity Effects. *Colloids and Surfaces*, **43**, 327–347.

Evans, E., & Needham, D. 1987. Physical Properties of Surfactant Bilayer Membranes: Thermal Transitions, Elasticity, Rigidity, Cohesion, and Colloidal Interactions. *J. Phys. Chem.*, **91**, 4219–4228.

Evans, E., & Rawicz, W. 1990. Entropy–Driven Tension and Bending Elasticity in Condensed–Fluid Membranes. *Phys. Rev. Lett.*, **64**, 2094–2097.

Evans, E., Yeung, A., Waugh, R., & Song, J. 1991. Dynamic Coupling and Nonlocal Curvature Elasticity in Bilayer Membranes. *Pages 148–159 of:* Lipowsky, R., Richter, D., & Kremer, K. (eds), *The Structure and Conformation of Amphiphilic Membranes.* Springer Proceedings in Physics, vol. 66. Berlin: Springer.

Evans, E.A. 1974. Bending Resistance and Chemically Induced Moments in Membrane Bilayers. *Biophys. J.*, **14**, 923–931.

Evans, E.A. 1980a. Analysis of Adhesion of Large Vesicles to Surfaces. *Biophys. J.*, **31**, 425–432.

Evans, E.A. 1980b. Minimum Energy Analysis of Membrane Deformation Applied to Pipet Aspiration and Surface Adhesion of Red Blood Cells. *Biophys. J.*, **30**, 265–284.

Evans, E.A. 1985. Detailed Mechanics of Membrane–Membrane Adhesion and Separation. I. Continuum of Molecular Cross–Bridges. *Biophys. J*, **48**, 175–183.

Farge, E., & Devaux, P.F. 1992. Shape Changes of Giant Liposomes Induced by an Asymmetric Transmembrane Distribution of Phospholipids. *Biophys. J.*, **61**, 347–357.

Faucon, J.F., Mitov, M.D., Meleard, P., Bivas, I., & Bothorel, P. 1989. Bending Elasticity and Thermal Fluctuations of Lipid Membranes. Theoretical and Experimental Requirements. *J. Phys. France*, **50**, 2389–2414.

Fischer, T.M. 1993. Bending Stiffness of Lipid Bilayers. V. Comparison of Two Formulations. *J. Phys. II France*, **3**, 1795–1805.

Fischer, T.M. 1994. Which membranes determine the time scales in vesicle budding? *Phys. Rev. E*, **??**, in press.

Foltin, G. 1994. Dynamics of incompressible fluid membranes. *Phys. Rev. E*, **49**, 5243–5248.

Förster, D. 1986. On the scale dependence, due to thermal fluctuations, of the elastic properties of membranes. *Phys. Lett.*, **114A**, 115–120.

Fourcade, B. 1992. Theoretical Results of Toroidal Vesicles. *J. Phys. II France*, **2**, 1705–1724.

Fourcade, B., Mutz, M., & Bensimon, D. 1992. Experimental and Theoretical Study of Toroidal Vesicles. *Phys. Rev. Lett.*, **68**, 2551–2554.

Fourcade, B., Miao, L., Rao, M., Wortis, M., & Zia, R.K.P. 1994. Scaling Analysis of Narrow Necks in Curvature Models of Fluid Lipid-Bilayer Vesicles. *Phys. Rev. E*, **49**, 5276–5286.

Frey, E., & Nelson, D.R. 1991. Dynamics of Flat Membranes and Flickering in Red Blood Cells. *J. Phys. I France*, **1**, 1715–1757.

Gebhardt, C., Gruler, H., & Sackmann, E. 1977. On Domain Structure and Local Curvature in Lipid Bilayers and Biological Membranes. *Z. Naturforsch.*, **32c**, 581–596.

Gompper, G., & Kroll, D.M. 1992. Inflated Vesicles: a New Phase of Fluid Membranes. *Europhys. Lett.*, **19**, 581–586.

Gompper, G., & Kroll, D.M. 1993. Floppy fluid vesicles in elongational flow. *Phys. Rev. Lett.*, **71**, 1111–1114.

Gompper, G., & Kroll, D.M. 1994. *Phase diagram and scaling behavior of fluid vesicles.* preprint.

Gompper, G., & Schick, M. 1994. Self-assembling amphiphilic systems. *In:* Domb, C., & Lebowitz, J. (eds), *Phase Transition and Critical Phenomena.* London: Academic.

Goos, J., & Gompper, G. 1993. Topological defects in lamellar phases: passages, and their fluctuations. *J. Phys. I France*, **3**, 1551–1567.

Goulian, M., Bruinsma, R., & Pincus, P. 1993. Long-Range Forces in Heterogeneous Fluid Membranes. *Europhys. Lett.*, **22**, 145–150.

Gruler, H. 1975. Chemoelastic Effects of Membranes. *Z. Naturforsch.*, **30c**, 608–614.

Heinrich, V., Brumen, M., Heinrich, R., Svetina, S., & Zeks, B. 1992. Nearly Spherical Vesicle Shapes Calculated by Use of Spherical Harmonics: Axisymmetric and Nonaxisymmetric Shapes and their Stability. *J. Phys. II France*, **2**, 1081–1108.

Heinrich, V., Svetina, S., & Zeks, B. 1993. Nonaxisymmetric Vesicle Shapes in a Generalized Bilayer–Couple Model and the Transition Between Oblate and Prolate Axisymmetric Shapes. *Phys. Rev. E*, **48**, 3112–3123.

Helfrich, W. 1973. Elastic Properties of Lipid Bilayers: Theory and Possible Experiments. *Z. Naturforsch.*, **28c**, 693–703.

Helfrich, W. 1974. Blocked Lipid Exchanges in Bilayers and its Possible Influence on the Shape of Vesicles. *Z. Naturforsch.*, **29c**, 510–515.

Helfrich, W. 1978. Steric Interaction of Fluid Membranes in Multilayer Systems. *Z. Naturforsch.*, **33a**, 305–315.

Helfrich, W. 1985. Effect of thermal undulations on the rigidity of fluid membranes and interfaces. *J. Physique*, **46**, 1263–1268.

Helfrich, W. 1986. Size distributions of vesicles: The role of the effective rigidity of membranes. *J. Physique*, **47**, 321–329.

Helfrich, W. 1987. Measures of integration in calculating the effective rigidity of fluid surfaces. *J. Physique*, **48**, 285–289.

Helfrich, W. 1994. Lyotropic lamellar phases. *J. Phys.: Condens. Matter*, **6**, A79–A92.

Helfrich, W., & Servuss, R.-M. 1984. Undulations, Steric Interaction and Cohesion of Fluid Membranes. *Il Nuovo Cimento*, **3D**, 137–151.

Ho, J.-S., & Baumgärtner, A. 1990. Simulation of Fluid Self–Avoiding Membranes. *Europhys. Lett.*, **12**, 295–300.

Hoffmann, H., Thunig, C., Munkert, U., Meyer, H.W., & Richter, W. 1992. From vesicles to the L_3 (Sponge) Phase in alkyldimenthylamine Oxide/Heptanol Systems. *Langmuir*, **8**, 2629–2638.

Homan, R., & Pownall, H.J. 1988. Transbilayer diffusion of phospholipids: Dependence on headgroup structure and acyl chain length. *Biochim. et Biophys. Acta*, **938**, 155–166.

Hsu, L., Kusner, R., & Sullivan, J. 1992. Minimizing the Squared Mean Curvature Integral for Surfaces in Space Forms. *Experimental Mathematics*, **1**, 191–207.

Hu, Jian-Guo, & Ou-Yang, Zhong-Can. 1993. Shape equations of the axisymmetric vesicles. *Phys. Rev. E*, **47**, 461–467.

Hyuga, H., Kinosita, K., Jr., & Wakabayashi, N. 1991a. Deformation of Vesicles under the Influence of Strong Electric Fields. *Japanese J. of Appl. Physics*, **30**, 1141–1148.

Hyuga, H., Kinosita, K., Jr., & Wakabayashi, N. 1991b. Deformation of Vesicles under the Influence of Strong Electric Fields II. *Japanese J. of Appl. Physics*, **30**, 1333–1335.

Israelachvili, J.N. 1991. *Intermolecular and Surface Forces*. second edn. London: Academic Press.

Israelachvili, J.N., & Wennerström, H. 1990. Hydration or steric forces between amphiphilic surfaces? *Langmuir*, **6**, 873–876.

Janiak, M.J., Small, D.M., & Shipley, G.G. 1979. Temperature and Compositional Dependence of the Structure of Hydrated Dimyristoyl Lecithin. *J. of Biol. Chem.*, **254**, 6068–6078.

Jenkins, J.T. 1977. Static Equilibrium Configurations of a Model Red Blood Cell. *J. Math. Biology*, **4**, 149–169.

Jülicher, F. 1993. *Die Morphologie von Vesikeln.* Ph.D. thesis, Universität zu Köln.

Jülicher, F., & Lipowsky, R. 1993. Domain–Induced Budding of Vesicles. *Phys. Rev. Lett.*, **70**, 2964–2967.

Jülicher, F., & Seifert, U. 1994. Shape equations for axisymmetric vesicles: A clarification. *Phys. Rev. E*, **49**, 4728–4731.

Jülicher, F., Seifert, U., & Lipowsky, R. 1993a. Conformal Degeneracy and Conformal Diffusion of Vesicles. *Phys. Rev. Lett.*, **71**, 452–455.

Jülicher, F., Seifert, U., & Lipowsky, R. 1993b. Phase Diagrams and Shape Transformations of Toroidal Vesicles. *J. Phys. II France*, **3**, 1681–1705.

Kaler, E.W., Muthy, A.K., Rodriguez, B.E., & Zasadzinski, J.A.N. 1989. Spontaneous Vesicle Formation in Aqueous Mixtures of Single–Tailed Surfactants. *Science*, **245**, 1371–1374.

Kaler, E.W., Herrington, K.L., Murthy, A.K., & Zasadzinski, J.A.N. 1992. Phase Behavior and Structures of Mixtures of Anionic and Cationic Surfactants. *J. Phys. Chem.*, **96**, 6698–6707.

Karcher, H., Pinkall, U., & Sterling, I. 1988. New Minimal Surfaces in S^3. *J. Differential Geometry*, **28**, 169–185.

Käs, J., & Sackmann, E. 1991. Shape Transitions and Shape Stability of Giant Phospholipid Vesicles in Pure Water induced by Area–to–Volume Changes. *Biophys. J.*, **60**, 825–844.

Käs, J., Sackmann, E., Podgornik, R., Svetina, S., & Zeks, B. 1993. Thermally Induced Budding of Phospholipid Vesicles – A Discontinuous Process. *J. Phys. II France*, **3**, 631–645.

Kawakatsu, T., Andelman, D., Kawasaki, K., & Taniguchi, K. 1993. Phase Transitions and Shape of Two Component Membranes and Vesicles I: Strong Segregation Limit. *J. Phys. II France*, **3**, 971–997.

Kleinert, H. 1986. Thermal softening of curvature elasticity in membranes. *Phys. Lett.*, **114A**, 263–268.

Komura, S., & Lipowsky, R. 1992. Fluctuations and stability of polymerized vesicles. *J. Phys. II France*, **2**, 1563–1575.

Kramer, L. 1971. Theory of Light Scattering from Fluctuations of Membranes and Monolayers. *J. of Chem. Phys.*, **55**, 2097–2105.

Kraus, M., & Seifert, U. 1994. Relaxation modes of an adhering bilayer membrane. *J. Phys. II France*, **4**, 1117–1134.

Kroll, D.M., & Gompper, G. 1992. The conformation of fluid membranes: Monte Carlo simulations. *Science*, **255**, 968–971.

Kummrow, M., & Helfrich, W. 1991. Deformation of Giant Lipid Vesicles by Electric Fields. *Phys. Rev. A*, **44**, 8356–8360.

Kusner, R. 1989. Comparison Surfaces for the Willmore Problem. *Pacific J. Math.*, **138**, 317–345.

Kusner, R. 1994. private comm.

Landau, L.D., & Lifshitz, E.M. 1989. *Elastizitätstheorie.* Berlin: Akademie–Verlag.

Langer, J., & Singer, D. 1984. Curves in the hyperbolic plane and mean curvature of tori and R^3 and S^3. *Bull. London Math. Soc.*, **16**, 531–534.

Langer, S.A., & Seifert, U. 1994. in preparation.

Langevin, D. 1992. *Light scattering by liquid surfaces and complimentary techniques.* New York: Marcel Dekker.

Lasic, D.D. 1994. Applications of Liposomes. *In:* Lipowsky, R., & Sackmann, E. (eds), *Structure and Dynamics of Membranes.* Amsterdam: Elsevier Science.

Lawson, H.B. 1970. Complete Minimal Surfaces in S^3. *Ann. Math.*, **92**, 335–374.

Leibler, S. 1986. Curvature Instability in Membranes. *J. Physique*, **47**, 507–516.

Leibler, S., & Andelman, D. 1987. Ordered and Curved Meso-Structures in Membranes and Amphiphilic Films. *J. Phys.*, **48**, 2013–2018.

Leibler, S., & Lipowsky, R. 1987. Complete unbinding and quasi-long-range order in lamellar phases. *Phys. Rev. B*, **35**, 7004–7009.

Leibler, S., Singh, R.R.P., & Fisher, M.E. 1987. Thermodynamic behavior of two-dimensional vesicles. *Phys. Rev. Lett.*, **59**, 1989–1992.

Lipowsky, R. 1990. Shape Fluctuations and Critical Phenomena. *Pages 139–170 of:* van Beijeren, H. (ed), *Fundamental Problems in Statistical Mechanics VII.* Elsevier Science.

Lipowsky, R. 1991. The conformation of membranes. *Nature*, **349**, 475–481.

Lipowsky, R. 1992. Budding of membranes induced by intramembrane domains. *J. Phys. II France*, **2**, 1825–1840.

Lipowsky, R. 1993. Domain-induced budding of fluid membranes. *Biophys. J.*, **64**, 1133–1138.

Lipowsky, R., & Girardet, M. 1990. Shape Fluctuations of Polymerized or Solidlike Membranes. *Phys. Rev. Lett.*, **65**, 2893–2896.

Lipowsky, R., & Grotehans, S. 1993. Hydration vs. Protrusion Forces Between Lipid Bilayers. *Europhys. Lett.*, **23**, 599–604.

Lipowsky, R., & Leibler, S. 1986. Unbinding transitions of interacting membranes. *Phys. Rev. Lett.*, **56**, 2541–2544.

Lipowsky, R., & Sackmann, E. 1994. *Structure and Dynamics of Membranes*. Amsterdam: Elsevier Science.

Lipowsky, R., & Seifert, U. 1991a. Adhesion of Membranes: A Theoretical Perspective. *Langmuir*, **7**, 1867–1873.

Lipowsky, R., & Seifert, U. 1991b. Adhesion of Vesicles and Membranes. *Mol. Cryst. Liq. Cryst.*, **202**, 17–25.

Lipowsky, R., & Zielinska, B. 1989. Binding and unbinding of lipid membranes: A Monte Carlo study. *Phys. Rev. Lett.*, **62**, 1572–1575.

Lipowsky, R., Richter, D., & Kremer, K. (eds). 1991. *The Structure and Conformation of Amphiphilic Membranes*. Springer Proceedings in Physics, vol. 66. Berlin: Springer.

Lubensky, T.C., & Prost, J. 1992. Orientational Order and Vesicle Shape. *J. Phys. II France*, **2**, 371–382.

Luke, J.C. 1982. A Method for the Calculation of Vesicle Shapes. *SIAM J. Appl. Math.*, **42**, 333–345.

Luke, J.C., & Kaplan, J.I. 1979. On theoretical shapes of bilayer lipid vesicles under conditions of increasing membrane area. *Biophys. J.*, **25**, 107–111.

MacKintosh, F.C., & Lubensky, T.C. 1991. Orientational Order, Topology, and Vesicle Shapes. *Phys. Rev. Lett.*, **67**, 1169–1172.

Maggs, A.C., & Leibler, S. 1990. Adsorption and fluctuations of two–dimensional vesicles. *Europhys. Lett.*, **12**, 19–24.

Marathe, Y., & Ramaswamy, S. 1989. Frequency–Dependent Viscosity of Membrane Solution. *Europhys. Lett.*, **8**, 581–585.

Markin, V.S. 1981. Lateral Organization of Membranes and Cell Shapes. *Biophys. J.*, **36**, 1–19.

Marra, J., & Israelachvili, J.N. 1985. Direct Measurements of Forces between Phosphatidylcholine and Phosphatidylethanolamine Bilayers in Aqueous Electrolyte Solutions. *Biochem.*, **24**, 4608–4618.

Marsh, D. 1990. *Handbook of lipid bilayers.* Florida: CRC Press.

Mecke, K. 1994. *Integralgeometrie in der Statistischen Physik: Perkolation, komplexe Flüssigkeiten und die Struktur des Universums.* Frankfurt am Main: Deutsch.

Meleard, P., Faucon, J.F., Mitov, M.D., & Bothorel, P. 1992. Pulsed–Light Microscopy Applied to the Measurement of the Bending Elasticity of Giant Liposomes. *Europhys. Lett.*, **19**, 267–271.

Merkel, R., Sackmann, E., & Evans, E. 1989. Molecular Friction and Epitactic Coupling between Monolayers in Supported Bilayers. *J. Phys. France*, **50**, 1535–1555.

Mermin, N.D., & Wagner, H. 1966. Absence of Ferromagnetism or Antiferromagnetism in one– or two–dimensional isotropic Heisenberg models. *Phys. Rev. Lett.*, **17**, 1133–1136.

Meunier, J., Langevin, D., & Boccara, N. 1987. *Physics of amphiphilic layers.* Springer–Verlag.

Miao, L. 1992. *Equilibrium shapes and shape transitions of fluid lipid-bilayer vesicles.* Ph.D. thesis, Simon Fraser University.

Miao, L., Fourcade, B., Rao, M., Wortis, M., & Zia, R.K.P. 1991. Equilibrium Budding and Vesiculation in the Curvature Model of Fluid Lipid Vesicles. *Phys. Rev. A*, **43**, 6843–6856.

Miao, L., Seifert, U., Wortis, M., & Döbereiner, H.-G. 1994. Budding Transitions of Fluid–Bilayer Vesicles: The Effect of Area–Difference Elasticity. *Phys. Rev. E*, **49**, 5389–5407.

Michalet, X. 1994. *Etude expérimentale de vésicule phospholipidiques de genre topologique non sphérique.* Ph.D. thesis, l'Université de Paris VII.

Michalet, X., Bensimon, D., & Fourcade, B. 1994. Fluctuating Vesicles of Nonspherical Topology. *Phys. Rev. Lett.*, **72**, 168–171.

Milner, S.T., & Safran, S.A. 1987. Dynamical Fluctuations of Droplet Microemulsions and Vesicles. *Phys. Rev. A*, **36**, 4371–4379.

Morse, D.C., & Milner, S.T. 1994a. Fluctuation and Phase Behavior of Fluid Membrane Vesicles. *Europhys. Lett.*, **26**, 565–570.

Morse, D.C., & Milner, S.T. 1994b. *Statistical Mechanics of Finite Fluid Membranes.* preprint.

Mui, B. L.-S., Döbereiner, H.-G., Madden, T.D., & Cullis, P.R. 1994. *Influence of differential monolayer area on the morphology of large unilamellar vesicles.* preprint.

Mutz, M., & Bensimon, D. 1991. Observation of Toroidal Vesicles. *Phys. Rev. A*, **43**, 4525–4527.

Mutz, M., & Helfrich, W. 1989. Unbinding transition of a biological model membrane. *Phys. Rev. Lett.*, **62**, 2881–2884.

Mutz, M., & Helfrich, W. 1990. Bending rigidities of some biological model membranes as obtained from the Fourier analysis of contour sections. *J. Phys. France*, **51**, 991–1002.

Naito, H., & Okuda, M. 1993. Counterexemple to some shape equations for axisymmetric vesicles. *Phys. Rev. E*, **48**, 2304–2307.

Nallet, F., Roux, D., & Prost, J. 1989. Hydrodynamics of Lyotropic Smectics: A Dynamic Light Scattering Study of Dilute Lamellar Phases. *J. Phys. France*, **50**, 3147–3165.

Needham, D., & Hochmuth, R.M. 1989. Electro–mechanical permeabilization of lipid vesicles. *Biophys. J.*, **55**, 1001–1009.

Needham, D., McIntosh, T.J., & Evans, E. 1988. Thermomechanical and Transition Properties of Dimyristoylphosphatidycholine/Cholesterol Bilayers. *Biochem.*, **27**, 4668–4673.

Nelson, D. 1988. The Statistical Mechanics of Crumpled Membranes. *Pages 193–215 of:* Stanley, H.E., & Ostrowsky, N. (eds), *Random Fluctuations and Pattern Growth.*

Nelson, D., Piran, T., & Weinberg, S. (eds). 1989. *Statistical Mechanics of Membranes and Surfaces.* Singapore: World Scientific.

Nelson, D.R., & Peliti, L. 1987. Fluctuations in membranes with crystalline and hexatic order. *J. Phys. France*, **48**, 1085–1092.

Nelson, P., & Powers, T. 1993. Renormalization of chiral couplings in tilted bilayer membranes. *J. Phys. II France*, **3**, 1535–1569.

Neumann, E., Sowers, A.E., & Jordan, C.A. (eds). 1989. *Electroporation and Electrofusion in Cell Biology.* New York: Plenum Press.

Nezil, F.A, & Bloom, M. 1992. Combined influence of cholesterol and synthetic amphiphillic peptided upon bilayer thickness in model membranes. *Biophys. J.*, **61**, 1176–1183.

Nikolic, M., Seifert, U., & Wortis, M. 1994. in preparation.

Ou-Yang, Z.-C. 1990. Anchor Ring–Vesicle Membranes. *Phys. Rev. A*, **41**, 4517–4520.

Ou-Yang, Z.-C., & Helfrich, W. 1987. Instability and Deformation of a Spherical Vesicle by Pressure. *Phys. Rev. Lett.*, **59**, 2486–2488.

Ou-Yang, Z.-C., & Helfrich, W. 1989. Bending Energy of Vesicle Membranes: General Expressions for the first, second and third Variation of the Shape Energy and Applications to Spheres and Cylinders. *Phys. Rev. A*, **39**, 5280–5288.

Palmer, K.M., Goulian, M., & Pincus, P. 1994. Fluctuation-induced forces in stacked fluid membranes. *J. Phys. II France*, **4**, 805–817.

Parsegian, V.A., Fuller, N., & Rand, R.P. 1979. Measured work of deformation and repulsion of lecithin bilayers. *Natl. Acad. Sci. USA*, **76**, 2750–2754.

Peliti, L. 1991. *Biologically inspired physics.* New York and London: Plenum Press.

Peliti, L., & Leibler, S. 1985. Effects of thermal fluctuations on systems with small surface tension. *Phys. Rev. Lett.*, **54**, 1690–1693.

Peterson, M.A. 1985a. Geometrical Methods for the Elasticity Theory of Membranes. *J. Math. Phys.*, **26**, 711–717.

Peterson, M.A. 1985b. An Instability of the Red Blood Cell Shape. *J. Appl. Phys.*, **57**, 1739–1742.

Peterson, M.A. 1985c. Shape Fluctuations of Red Blood Cells. *Mol. Cryst. Liq. Cryst.*, **127**, 159–186.

Peterson, M.A. 1988. Comment on "Instability and Deformation of a Spherical Vesicle by Pressure". *Phys. Rev. Lett.*, **61**, 1325.

Peterson, M.A. 1989. Deformation energy of vesicles at fixed volume and surface area in the spherical limit. *Phys. Rev. A*, **39**, 2643–2645.

Peterson, M.A. 1992. Linear Response of the Human Erythrocyte to Mechanical Stress. *Phys. Rev. A*, **45**, 4116–?

Peterson, M.A., Strey, H., & Sackmann, E. 1992. Theoretical and Phase Contrast Microscopic Eigenmode Analysis of Erythrocyte Flicker: Amplitudes. *J. Phys. II France*, **2**, 1273–1285.

Pfeiffer, W., König, S., Legrand, J.F., Bayerl, T., Richter, D., & Sackmann, E. 1993. Neutron Spin Echo Study of Membrane Undulations in Lipid Multibilayers. *Europhys. Lett.*, **23**, 457–462.

Pinkall, U. 1985. Hopf tori in S^3. *Invent. math.*, **81**, 379–386.

Pinkall, U., & Sterling, I. 1987. Willmore Surfaces. *The Mathematical Intelligencer*, **9**, 38–43.

Polyakov, A.M. 1987. *Gauge fields and strings.* Harward Academic Publishers.

Porte, G. 1992. Lamellar phases and disordered phases of fluid bilayer membranes. *J. Phys.: Condens. Matter*, **4**, 8649–8670.

Rädler, J. 1993. *Über die Wechselwirkung fluider Phospholipid-Membranen mit Festkörperoberflächen.* Ph.D. thesis, TU–München.

Rädler, J., & Sackmann, E. 1992a. On the Measurement of Weak Repulsive and Frictional Colloidal Forces by Reflection Interference Contrast Microscopy. *Langmuir*, **8**, 848–852.

Rädler, J., & Sackmann, E. 1992b. Vesicle-substrate interaction studied by reflection interference contrast microscopy. *In:* Lipowsky, R., Richter, D., & Kremer, K. (eds), *The structure and conformation of amphiphilic membranes.* Berlin: Springer.

Rädler, J.O., Feder, T.J., Strey, H.H., & Sackmann, E. 1994. *Fluctuation analysis of tension–controlled undulation forces between giant vesicles and solid substrates.* preprint.

Rand, R.P., & Parsegian, V.A. 1989. Hydration forces between phospholipid bilayers. *Biochim. Biophys. Acta*, **988**, 351–376.

Robertis, E.D.P. De, & E.M.F. De Robertis, Jr. 1980. *Cell and Molecular Biology.* seventh edn. Philadelphia: Saunders College.

Roux, D., Coulon, C., & Cates, M.E. 1992. Sponge Phases in Surfactant Solutions. *J. Phys. Chem.*, **96**, 4174–4187.

Sackmann, E. 1990. Molecular and Global Structure and Dynamics of Membranes and Lipid Bilayers. *Can. J. Phys.*, **68**, 999–1012.

Safran, S.A., Pincus, P., & Andelman, D. 1990. Theory of Spontaneous Vesicle Formation in Surfactant Mixtures. *Science*, **248**, 354–356.

Safran, S.A., Pincus, P.A., Andelman, D., & MacKintosh, F.C. 1991. Stability and Phase Behavior of Mixed Surfactant Vesicles. *Phys. Rev. A*, **43**, 1071–1078.

Schmidt, C.F., Svoboda, K., Lei, N., Petsche, I.B., Berman, L.E., Safinya, C.R., & Grest, G.S. 1993. Existence of a Flat Phase in Red Cell Membrane Skeletons. *Science*, **259**, 952–955.

Schneider, M.B., Jenkins, J.T., & Webb, W.W. 1984a. Thermal Fluctuations of Large Cylindrical Phospholipid Vesicles. *Biophys. J.*, **45**, 891–899.

Schneider, M.B., Jenkins, J.T., & Webb, W.W. 1984b. Thermal Fluctuations of Large Quasi-Spherical Bimolecular Phospholipid Vesicles. *J. Phys.*, **45**, 1457–1472.

Schnitzler, W. 1993. *Simulation und Analyse dreidimensionaler Vesikel- und Erythrozytenformen.* Diplomarbeit RWTH Aachen.

Seifert, U. 1990. Shape Transformations of Free, Toroidal and Bound Vesicles. *Journal de Physique, Colloque*, **51,C7**, 339–344.

Seifert, U. 1991a. Adhesion of Vesicles in Two Dimensions. *Phys. Rev. A*, **43**, 6803–6814.

Seifert, U. 1991b. Conformal Transformations of Vesicle Shapes. *J. Phys. A: Math. Gen.*, **24**, L573–L578.

Seifert, U. 1991c. Vesicles of Toroidal Topology. *Phys. Rev. Lett.*, **66**, 2404–2407.

Seifert, U. 1993. Curvature–Induced Lateral Phase Segregation in Two–Component Vesicles. *Phys. Rev. Lett.*, **70**, 1335–1338.

Seifert, U. 1994a. Dynamics of a bound membrane. *Phys. Rev. E*, **49**, 3124–3127.

Seifert, U. 1994b. Morphology and dynamics of budding of vesicles. *Pages ?? – ?? of:* Felix, D. Beysens M.-A., Forgasz, G., & Gaill, F. (eds), *Interplay of genetic and physical processes in the development of biological form.* Springer.

Seifert, U., & Langer, S.A. 1993. Viscous Modes of Fluid Bilayer Membranes. *Europhys. Lett.*, **23**, 71–76.

Seifert, U., & Langer, S.A. 1994. Hydrodynamics of membranes: the bilayer aspect and adhesion. *Biophys. Chem.*, **49**, 13–22.

Seifert, U., & Lipowsky, R. 1990. Adhesion of Vesicles. *Phys. Rev. A*, **42**, 4768–4771.

Seifert, U., & Lipowsky, R. 1993. Adhesion and Unbinding of Vesicles. *Pages 295–304 of:* Beysens, D., Boccara, N., & Forgacz, G. (eds), *Dynamical phenomena at interfaces, surfaces and membranes.* New York: Nova Science.

Seifert, U., Miao, L., Döbereiner, H.-G., & Wortis, M. 1991a. Budding Transition for Bilayer Fluid Vesicles with Area–Difference Elasticity. *Pages 93–96 of:* Lipowsky, R., Richter, D., & Kremer, K. (eds), *The Structure and Conformation of Amphiphilic Membranes.* Springer Proceedings in Physics, vol. 66. Berlin: Springer.

Seifert, U., Berndl, K., & Lipowsky, R. 1991b. Shape transformations of vesicles: Phase diagrams for spontaneous–curvature and bilayer–coupling models. *Phys. Rev. A*, **44**, 1182–1202.

Servuss, R.-M., & Helfrich, W. 1989. Mutual adhesion of lecithin membranes at ultralow tensions. *J. Phys. France*, **50**, 809–827.

Sheetz, M.P., & Singer, S.J. 1974. Biological Membranes as Bilayer Couples. A Molecular Mechanism of Drug–Erythrocyte Interactions. *Proc. Natl. Acad. Sci. (USA)*, **71**, 4457–4461.

Steck, T.L. 1989. Red Cell Shape. *Pages 205–246 of:* Stein, W., & Bronner, F. (eds), *Cell Shape Determinants, Regulation, and Regulatory Role.* Academic Press, NY.

Stokke, B.T., Mikkelsen, A., & Elgsaeter, A. 1986a. The Human Erythrocyte Membrane Skeleton May be an Ionic Gel. I. Membrane Mechanochemical Properties. *Eur. Biophys. J.*, **13**, 203–218.

Stokke, B.T., Mikkelsen, A., & Elgsaeter, A. 1986b. The Human Erythrocyte Membrane Skeleton May be an Ionic Gel. II. Numerical Analyses of Cell Shapes and Shape Transformations. *Eur. Biophys. J.*, **13**, 219–233.

Strey, H. 1993. *Bestimmung elastischer Eigenschaften von Zellmembranen und Zytoskelett mittels Flickerspektroskopie.* Ph.D. thesis, TU-München.

Svetina, S., & Zeks, B. 1983. Bilayer couple hypothesis of red cell shape transformations and osmotic hemolysis. *Biochemica et Biophysica Acta*, **42**, 86–90.

Svetina, S., & Zeks, B. 1989. Membrane bending energy and shape determination of phospholipid vesicles and red blood cells. *Eur. Biophys. J.*, **17**, 101–111.

Svetina, S., & Zeks, B. 1992. The Elastic Deformability of Closed Multilayered Membranes is the same as that of a Bilayer Membrane. *Eur. Biophys. J.*, **21**, 251–255.

Svetina, S., Ottova-Leitmanova, A., & Glaser, R. 1982. Membrane Bending Energy in Relation to Bilayer Couples Concept of Red Blood Cell Shape Transformations. *J. theor. Biol.*, **94**, 13–23.

Svoboda, K., Schmidt, C.F., Branton, D., & Block, S.M. 1992. Conformation and Elasticity of the Isolated Red Blood Cell Membrane Skeleton. *Biophys. J.*, **63**, 784–793.

Taniguchi, T., Kawasaki, K., Andelman, D., & Kawakatsu, T. 1994. Equilibrium Shape Deformations of Two-Component Vesicles. *J. Phys. II France*, **4**, 1333–1362.

Thomsen, G. 1924. Grundlagen der konformen Flächentheorie. *Abh. Math. Sem. Univ. Hamburg*, **3**, 31–56.

Vist, M.R., & Davis, J.H. 1990. Phase Equilibria of Cholesterol/Dipalmitoylphosphatidylcholine Mixtures: ^{2}H Nuclear Magnetic Resonance and Differential Scanning Calorimetry. *Biochemistry*, **29**, 451–464.

Waugh, R., & Evans, E.A. 1979. Thermoelasticity of Red Blood Cell Membrane. *Biophys. J.*, **26**, 115–132.

Waugh, R.E., Song, J., Svetina, S., & Zeks, B. 1992. Local and nonlocal curvature elasticity in bilayer membranes by tether formation from lecithin vesicles. *Biophys. J.*, **61**, 974–982.

Wheater, J.F. 1994. Random surfaces: From polymer membranes to strings. *J. Phys. A: Math. Gen.*, **27**, 3323–3353.

Wiese, W., Harbich, W., & Helfrich, W. 1992. Budding of lipid bilayer vesicles and flat membranes. *J. Phys.: Cond. Matter*, **4**, 1647–1657.

Willmore, T.J. 1965. Note on embedded surfaces. *Anal. Scient. ale Univ. Iasi (Sect. Ia)*, **11**, 493–496.

Willmore, T.J. 1982. *Total curvature in Riemannian geometry.* Chicester: Ellis Horwood.

Winterhalter, M., & Helfrich, W. 1987. Effect of voltage on pores in membranes. *Phys. Rev. A*, **36**, 5874–5876.

Wortis, M., Seifert, U., Berndl, K., Fourcade, B., Miao, L., Rao, M., & Zia, R.K.P. 1993. Curvature–Controlled Shapes of Lipid–Bilayer Vesicles: Budding, Vesiculation and Other Phase Transitions. *Pages 221–236 of:* Beysens, D., Boccara, N., & Forgacs, G. (eds), *Dynamical phenomena at interfaces, surfaces and membranes.* New York: Nova Science.

Wu, S.H.-W., & McConnell, H.M. 1975. Phase Separations in Phospholipid Membranes. *Biochemistry*, **14**, 847–854.

Yeung, A.K.C. 1994. *Mechanics of Inter–Monolayer Coupling in Fluid Surfactant Bilayers.* Ph.D. thesis, University of British Columbia.

Zheng, W.-M., & Liu, J. 1993. Helfrich shape equation for axisymmetric vesicles as a first integral. *Phys. Rev. E*, **48**, 2856–2860.

Zilker, A., Engelhardt, H., & Sackmann, E. 1987. Dynamic Reflection Interference Contrast (RIC-) Microscopy: A New Method to Study Surface Excitations of Cells and to Measure Membrane Bending Elastic Moduli. *J. Physique*, **48**, 2139–2151.

Zilker, A., Ziegler, M., & Sackmann, E. 1992. Spectral Analysis of Erythrocyte Flickering in the 0.3–4-μm^{-1} Regime by Microinterferometry Combined with Fast Image Processing. *Phys. Rev. A*, **46**, 7998–8001.

Zimmermann, U. 1982. Electric field–mediated fusion and related electrical phenomena. *Biochemica et Biophysica Acta*, **694**, 227–277.

FORSCHUNGSZENTRUM JÜLICH GmbH

KFA

Jül-2997
December 1994
ISSN 0944-2952